



DYNAMICS OF GALAXY CLUSTERS AND THEIR OUTSKIRTS: beyond the virialization regime

MARTINA FALCO

Dissertation
Submitted for the Degree

PHILOSOPHIÆ DOCTOR

Dark Cosmology Centre
The PhD School of Science
Faculty of Science
University of Copenhagen

Submission: 19/11/2013
Defence: 10/01/2014

Supervisor: *Prof. Steen Hansen*
Opponents: *Prof. Wyn Evans*
Prof. Claudia De Rham

ACKNOWLEDGMENT

I would like to thank my supervisor Steen, an irreplaceable support, from the scientific and maybe even more the personal point of view. I thank my friend and colleague Radek, for all the inspiring discussions and for helping me from the first day of my PhD to the last.

When I got this position I could not imagine how important that moment would have been for my life, Copenhagen and DARK got a big place in my heart forever, and I thank all the people I have met here.

I don't know how I would survive without the "italian crew" : Matteo C., Claudio, Nico, Stefania, Matteo B., Anna, Stefano... thank you for being my family here. I thank my wonderful friends Ia, Karen, Ece, Johan, Allison, Johannes, Thomas, Anja, for sharing the good and the bad times, and listening to me whenever I need. I thank my flatmates Ilaria and Ludo, because home still means Napoli! Thanks to all the people I met during these three years, who make me enjoy my life in Copenhagen.

Thanks to my family and my friends in Napoli, for being so close to me, despite the distance.

Martina

ABSTRACT

Galaxy clusters have demonstrated to be powerful probes of cosmology, since their mass and abundance depend on the cosmological model that describes the Universe and on the gravitational formation process of cosmological structures. The main challenge in using clusters to constrain cosmology is that their masses cannot be measured directly, but need to be inferred indirectly through their observable properties. The most common methods extract the cluster mass from their strong X-ray emission or from the measured redshifts of the galaxy members. The gravitational lensing effect caused by clusters on the background galaxies is also an important trace of their total mass distribution.

In the work presented within this thesis, we exploit the connection between the gravitational potential of galaxy clusters and the kinematical properties of their surroundings, in order to determine the total cluster mass. To this end we investigate in detail the dynamics of the non equilibrated region outside virialized clusters. Massive clusters attract galactic groups and larger structures against the expansion of the Universe. We determine the theoretical equations that allow us to model the motion of galaxies at any distance from the center of a cluster. Moreover, we analyze spectroscopic observations of galaxies far away from the central part of the cluster.

The main result of this study is the development of two new methods to measure the mass of galaxy clusters. One constrains the virial mass and the other extends the mass determination far outside the radius of virialization. Our tests performed on cosmological simulations and observational data validate the proposed methods. We also formalize a justification for the *Jeans swindle*, i.e. the inconsistency that characterizes the dynamical mass measurement of any cosmological structure, by explaining it within the framework of an expanding Universe.

CONTENTS

Acknowledgment	iii
Abstract	iv
Contents	v
1 Introduction	1
1.1 Cosmological background	2
1.1.1 The expanding Universe	2
1.1.2 Friedmann-Robertson-Walker cosmology	3
1.1.3 Various components of the Universe	4
1.1.4 Dark matter evidence	6
1.1.5 Λ CDM model	8
1.2 Large scale structures	8
1.3 Galaxy clusters	10
1.4 Dark matter haloes around galaxy clusters	12
1.5 Dynamics of galaxy clusters	13
1.5.1 The Jeans equation for spherical systems	15
1.5.2 The non equilibrium region of galaxy clusters	17
1.6 Galaxy clusters as cosmological probes	18
2 Mass estimation of galaxy clusters	21
2.1 The Virial Theorem method	21
2.2 Analysis of the ICM properties	22
2.3 The Jeans dynamical approach	24
2.4 The caustic method	27
2.5 The gravitational lensing	30
2.6 This thesis: new approaches to the cluster mass estimation	32
3 Mass estimation in the inner region of galaxy clusters from the outskirts	35
3.1 Summary	36
3.2 Introduction	37
3.2.1 Mass estimate from the radial velocity profile	38
3.2.2 Radial infall velocity profile	39
3.3 Filaments and sheets around galaxy clusters	40
3.3.1 Line of sight velocity profile	41
3.3.2 Linear structures in the velocity field	42
3.4 Testing the method on Cosmological Simulation	43

3.4.1	Identification of filaments and sheets from the velocity field	43
3.4.2	Analysis and result	45
3.5	Result on Coma cluster	47
3.6	Summary and Conclusion	53
4	Mass estimation in the outer region of galaxy clusters	57
4.1	Summary	58
4.2	Introduction	59
4.3	Non-equilibrium dynamics of galaxy clusters: the generalized Jeans equation . .	60
4.4	Comparison with cosmological simulations	62
4.4.1	The simulation	62
4.4.2	Analytical approximations to density, anisotropy and mean radial velocity profiles	63
4.4.3	Comparison with a stacked halo	70
4.4.4	Comparison with isolated halos	72
4.5	Conclusions and Discussion	74
5	The Jeans swindle	81
5.1	Summary	82
5.2	Introduction	84
5.3	Jeans Swindle in the Jeans equation	84
5.4	Why the Jeans Swindle works	87
5.5	Comoving coordinates	89
5.6	Conclusions	89
6	Conclusion	91
6.1	Summary	91
6.2	Future work	92
	Bibliography	93

1

INTRODUCTION

The description of the cosmos has become a very important discipline in astronomy. In the last decade, several observations have revolutionized cosmology, by providing strong evidence for the existence of new forms of matter (dark matter) and energy (dark energy). Understanding how the Universe is composed, how it formed and how it will evolve are the main aspects of modern cosmology. Progresses have been achieved by the improvement of observational techniques and the development of new physical theories. One of the main cosmological probes is the study of how the matter is distributed into the structures that we observe today.

This thesis fits into the general context of investigating the properties of the Universe by looking at its large scale structure. In particular, our efforts are devoted to improve the knowledge of the dynamical properties of clusters of galaxies and their mass distribution. An important part of our work is also dedicated to give a contribution to the characterization of other more complex cosmological objects.

Galaxy clusters are the easiest large scale structures to study, since they seem to manifest themselves as the most massive bound and quasi-relaxed objects in the Universe. The main feature that makes galaxy clusters a great cosmological laboratory, is that their matter density is dominated by invisible dark matter. It accounts for more than 80% of the total matter in the Universe, and therefore it plays a central role in cosmological studies. Despite that, dark matter has never been observed directly, and a concrete understanding of its nature remains elusive. The study of galaxy clusters provides a direct way to estimate the total mass content in the Universe. In fact, the estimation of the mass of clusters has become a prominent research field in the last decades. Moreover, the formation and evolution of clusters is connected to the expansion history and the growth of large scale structures in the Universe. For example, clusters are well suited to explore the dark energy problem. These studies require a good understanding of the relation between the mass of a cluster and the observables.

Galaxy clusters emerge from a hierarchical structure formation process: small overdensities in the Universe follow a merging process that leads to the formation of larger structures. The matter falls into these large halos, increasing their mass, and the last stadium of the assembly process is the dynamical equilibrium of the matter inside the formed objects.

The dynamics of galaxy clusters is fully understood in the region where the galaxies have reached the state of equilibrium, and several methods for the mass estimation in that region provide quite accurate measurements. Nevertheless, in order to better understand the formation and evolution of structures, a consistent description of the cluster dynamics and the mass distribution needs to be extended also to the outermost regions of clusters, where the matter has generally not reached dynamical equilibrium.

In the hierarchical scenario of structure formation, galaxy clusters are interconnected via less equilibrated structures, such as two-dimensional sheets and one-dimensional filaments, which represent the channel for the matter to flow into the clusters. These objects are much more difficult to observe than clusters, because their overdensity is only just above the average density of the Universe. A deep and detailed understanding of their properties has not been achieved so far. However, a clear definition and the consequent detection of such filaments and sheets, as well as studying their connection to the dynamics of galaxy clusters, would represent a very useful tool for probing cosmology.

In this chapter, we introduce the theoretical and observational framework which represents the starting point of this thesis. In particular, we place galaxy clusters into the cosmological picture, highlighting the currently accepted large scale structure scenario and describing how the mass of clusters is used as cosmological probe. We also focus our attention on the current understanding of the galaxy clusters dynamics.

1.1 COSMOLOGICAL BACKGROUND

In this section I present an overview of all the aspects of cosmology that provides the basis of this thesis and that will be relevant for the subsequent discussions.

All the work developed in this thesis is mainly based on the dynamics of cosmological large scale structures, namely the study of their internal and relative motion.

1.1.1 THE EXPANDING UNIVERSE

A crucial discovery in the history of cosmology is that the Universe is expanding. This implies that galaxies are receding from us and from each other. At the scale of galaxy clusters and larger, the recession motion of galaxies plays a key role in the study of the kinematics and therefore it will represent an important aspect of analysis done in this thesis.

The first observational evidence of the expansion of the Universe was made by Hubble (1929). He describes this phenomena by a very simple equation called *Hubble's law*. If galaxies are moving away from us, the light coming from a galaxy arrives with a wavelength larger than the one originally emitted. We define the *redshift* z of a galaxy as

$$z = \frac{\lambda_{obs}}{\lambda_{em}} - 1, \quad (1.1)$$

where λ_{obs} is the observed wavelength and λ_{em} is the wavelength at the time of emission. The redshift corresponds to a recession velocity v , which, for nearby objects, is given by a simple Doppler formula $v = cz$. Hubble (Hubble, 1929) discovered a linear relation between the distance of a galaxy r and its receding velocity v , which is referred to as Hubble's law

$$v = cz = H_0 r. \quad (1.2)$$

The proportionality constant H_0 is defined as the *Hubble constant*, and quantifies the expansion rate of the Universe at the current time. It is common to write H_0 in the normalized and dimensionless form

$$H_0 = 100 \text{ h km s}^{-1} \text{ Mpc}^{-1}. \quad (1.3)$$

A measurement of the expansion of the Universe, i.e. the Hubble constant, requires the knowledge of both the distance of an object and its velocity. The velocity of an object is obtained from its redshift. Accurate distance measurements are more difficult to obtain. One of the

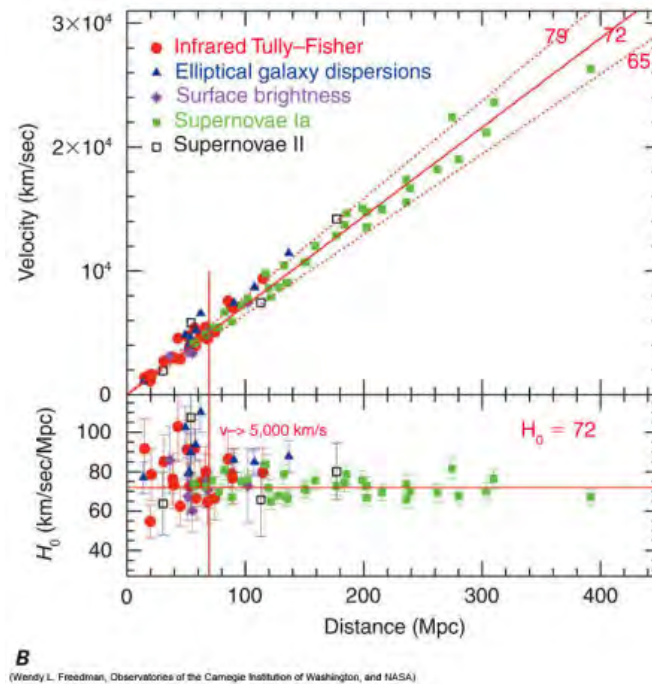


Figure 1.1 . Hubble diagram obtained by the HST key project. The different colored dots represent different ways of measuring distance. The different lines plotted alongside experimental data correspond to different values of H_0 . The best fit for these data is $H_0 = 72 \text{ km s}^{-1} \text{ Mpc}^{-1}$. The bottom panel shows the differences between the points and the solid line. Figure from (Freedman et al. (2001)).

common methods is to use standard candles, i.e. sources with the same known luminosity, as for example the Type Ia Supernovae (SNeIa). In Figure 1.1 the Hubble diagram is shown. The data are obtained from different methods, and the theoretical lines correspond to different values of the Hubble constant.

Current measurements of the Hubble constant give values in the range $h = 0.6 - 0.8$. The HST Telescope (Freedman et al., 2001) gives $h = 0.72 \pm 0.08$, and WMAP (Spergel et al., 2007) measures $h = 0.7 \pm 0.022$. The Riess's supernovae result is 0.73 ± 0.03 (Riess et al., 1998), while the recent Planck mission finds a significantly lower value $h = 0.67 \pm 0.014$ (Planck Collaboration et al., 2013). The errorbars of these estimations are all within 1σ .

Going to higher redshifts, the luminosity distance departs from the linear Hubble law and shows that the Universe expansion is accelerating. This evidence means that the ordinary matter and radiation, whose motion is driven by the attractive gravitational force, are not the only components of the Universe.

1.1.2 FRIEDMANN-ROBERTSON-WALKER COSMOLOGY

The equations that govern the accelerating expansion of the Universe are derived by introducing a metric, which describes the space-time, and by using the formalism of General Relativity.

The *Cosmological Principle* states that, on sufficiently large scales, the Universe is homogeneous and isotropic. This assertion was originally assumed, and subsequently confirmed by

observations for the very large scale of the Universe. Assuming homogeneity and isotropy, the unique form of the line element obeys the Friedmann-Robertson-Walker (FRW) metric and can be written as :

$$ds^2 = -dt^2 + a(t)^2 \left[\frac{dr^2}{1 - kr^2} + r^2(d\theta^2 + \sin^2\theta d\phi^2) \right], \quad (1.4)$$

where t is the cosmic time, and r, θ, ϕ are the spherical polar coordinates. The parameter k determines the curvature of the spatial hyper-surface and can take the values $k = 0$, corresponding to a flat space, $k = 1$, corresponding to a closed space, with finite volume and no boundary, and $k = -1$, corresponding to an open, infinite space. The *scale factor* $a(t)$ encodes the size of the Universe at large scales, and it is related to the redshift z by

$$1 + z = \frac{a(t_{obs})}{a(t_{em})}, \quad (1.5)$$

where t_{obs} is the time at which the light emitted at time t_{em} by a source is observed.

The General Relativity applied to the FRW metric yields two fundamental equations (Carroll, 2004):

- The *Friedmann equation*

$$H^2 = \left(\frac{\dot{a}}{a} \right)^2 = \frac{8\pi G}{3} \rho - \frac{k}{a^2} \quad (1.6)$$

- The *Fluid equation*

$$\dot{H} + H^2 = \frac{\ddot{a}}{a} = -\frac{4\pi G}{3} (\rho + 3P), \quad (1.7)$$

where we use the relation between the Hubble parameter and the scale factor

$$H(t) = \frac{\dot{a}(t)}{a(t)}. \quad (1.8)$$

The quantities ρ and P are the total energy density and pressure of the Universe.

Observations of our Universe justify the development of cosmological models that assume the existence of different components in the Universe. They all contribute to the total density and pressure. From the point of view of cosmology, the relevant feature of each component is how its energy density evolves as the Universe expands, and what the abundance of each specie is at the present time. In the following section, we show how the Universe is described in terms of *cosmological density parameters* related to the different components.

1.1.3 VARIOUS COMPONENTS OF THE UNIVERSE

The density in the Universe is due to matter (baryonic or not baryonic) and radiation. In order to explain the acceleration of the expansion of the Universe, a fluid for which gravity is repulsive has been introduced as one of the species in the present Universe. This new component is referred to as dark energy and it is associated to a non-null cosmological constant Λ . The vacuum density is written as

$$\rho_\Lambda = \frac{\Lambda}{8\pi G}. \quad (1.9)$$

Hence, ρ can be written as the sum of the density of matter ρ_M , the density of radiation ρ_r and the vacuum energy density ρ_Λ :

$$\rho = \rho_M + \rho_r + \rho_\Lambda. \quad (1.10)$$

Conventionally, the abundance of each density component i is expressed by the dimensionless parameter

$$\Omega = \frac{\rho_i}{\rho_{crit}}, \quad (1.11)$$

where the *critical density* ρ_{crit} is the present energy density of a flat Universe and is given by

$$\rho_{crit} = \frac{3H^2}{8\pi G}. \quad (1.12)$$

The three component parameters are

$$\Omega_M = \frac{8\pi G\rho_M}{3H^2}, \quad \Omega_r = \frac{8\pi G\rho_r}{3H^2}, \quad \Omega_\Lambda = \frac{\Lambda}{3H^2}. \quad (1.13)$$

When including the cosmological constant, equation (1.6) can be arranged in terms of the parameters in equation (1.13) as

$$\Omega = \Omega_r + \Omega_M + \Omega_\Lambda = 1 + \frac{k}{a^2H^2}. \quad (1.14)$$

The sum Ω is the total *density parameter*, and it describes the curvature of the Universe. If $\Omega > 1$ the curvature parameter k is greater than zero, signifying a Universe with positive curvature. If $\Omega < 1$, then $k < 0$, corresponding to a negative curvature. A critical value is obtained when $\Omega = 1$, which is the case of flat Universe, $k = 0$.

One can define

$$\Omega_k = -\frac{k}{a^2H^2}, \quad (1.15)$$

in analogy with the other terms. With this notation, the Friedmann equation (1.14) can be seen as a constraint on the cosmological parameters:

$$\sum_i \Omega_i = 1. \quad (1.16)$$

The main goal of cosmological studies is to determine the fractional contribution of the different components.

The energy densities of the each component evolve with the pressure P according to the equation of state $\rho = wP$. The dimensionless parameter w depends on the corresponding component. In the general case, this parameter varies with time. For constant w , plugging the equation of state into the fluid equation, one obtains the energy density as function of the scale factor

$$\rho = \rho_0 a^{-3(1+w)}. \quad (1.17)$$

For non-relativistic particles, both dark matter and baryons, $w = 0$. For relativistic matter, i.e. radiation, $w = +1/3$. An accelerating Universe requires a component with negative pressure, therefore $w < -1/3$. When the acceleration of the Universe is explained with the presence of vacuum energy, $w = -1$.

Using equations (1.6) and (1.7), the evolution of the scale factor is

$$a(t) \propto t^{2/3(1+w)}, \quad (1.18)$$

for constant w .

Figure 1.2 shows the evolution of the radiation matter, and dark energy densities with redshift. In the early hot Universe ($z > 3000$), the radiation dominates, and the Universe expands

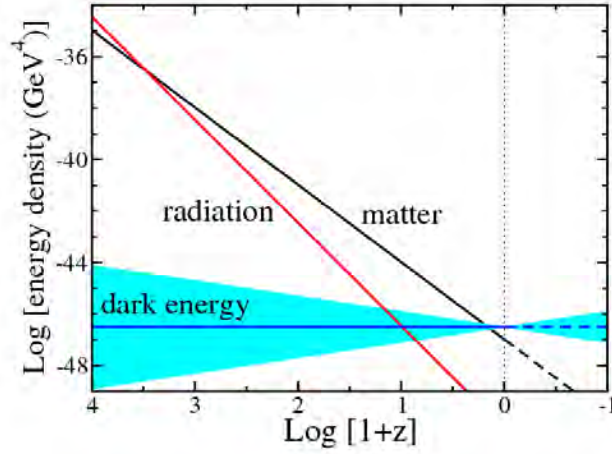


Figure 1.2 Evolution of the density of radiation, matter, and dark energy densities with redshift. For dark energy, the band represents $w = -1 \pm 0.2$.

as $a(t) \propto t^{1/2}$. At redshifts $3000 > z > 0.5$ the Universe is matter-dominated and expands as $a(t) \propto t^{2/3}$. At $z < 0.5$ the dark energy-dominated era begins and the Universe expands exponentially $a(t) \propto \exp(Ht)$.

In order to better understand the effect of the components on the acceleration of the Universe, the deceleration parameter $q(z)$ has been introduced and defined as

$$q(z) = -\frac{\ddot{a}}{aH^2} = \frac{1}{2} \sum_i \Omega_i(z) [1 + 3w_i(z)] \quad (1.19)$$

During the matter- and radiation-dominated eras, gravity slows the expansion, and thus $q > 0$ and $\ddot{a} < 0$. During the vacuum energy-dominated era, the Universe starts to accelerate ($q < 0$ and $\ddot{a} > 0$).

1.1.4 DARK MATTER EVIDENCE

In this thesis we will deal with the dynamics of the constituents of the matter in the Universe. Therefore, we are interested in the properties of the total matter density. We will here review the most clear observational indications for the existence of a dominant non visible form of matter.

The energy density of visible matter (stars, gas, dust, etc.) is in fact not enough to account for all the matter density in the Universe. Several evidences give rise to the existence of dark matter (DM), i.e. matter that does not emit light and can be observed only through its gravitational effects.

The most important type of analysis for establishing the presence of dark matter is the kinematical study of stars in galaxies and galaxies in galaxy clusters. The first indication of dark matter was found in the Coma cluster by Zwicky (Zwicky, 1933), who observed the radial velocities of galaxies around the cluster. He found an unexpectedly large velocity dispersion (1000 km s^{-1}) and concluded, by the application of the virial theorem, that for such a velocity dispersion, the mean density of the Coma cluster would need to be much greater than the one derived from luminous matter only.

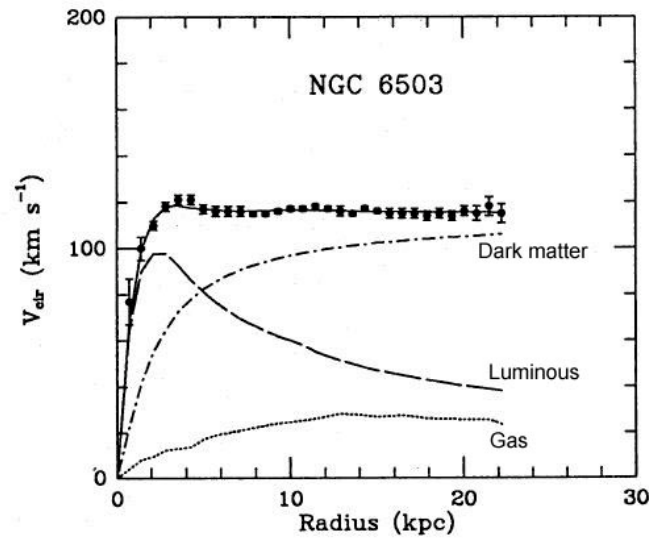


Figure 1.3 Rotation curve for the spiral galaxy NGC6503: circular velocity v_c as function of the distance from the galaxy center. The dashed and dotted curves are the contributions to v_c due to the disc and the gas, respectively, while the dot-dash curve represents the contribution from the dark halo. Figure from (Begeman et al., 1991).

Although dark matter was found for the first time in clusters of galaxies, the clearest evidence of its existence was shown at the scale of galaxies. Assuming a balance between the gravitational and centrifugal forces within Newtonian mechanics, the circular velocity of a star in a galaxy is expected to fall with the distance as $v_c^2 = GM(r)/r$, where $M(r)$ is the total mass within the radius r . The observed rotation curves of spiral galaxies show that v_c instead becomes roughly constant with radius (Figure 1.3 shows an example of the rotation curve of a spiral galaxy, from Begeman et al. (1991)). This implies that $M(r) \propto r$. A linearly increasing mass cannot be justified by the presence of the disk, the bulge or the stellar halo. It can be explained only by assuming that dark matter is present in an approximately spherical halo surrounding the disk, with density distribution $\rho(r) \propto 1/r^2$.

Another probe of the matter in galaxy clusters is gravitational lensing (Mandelbaum et al., 2010). A galaxy cluster can act as a gravitational lens which distorts the light of background galaxies or quasars. Therefore, observations of background galaxies can be used to determine the mass distribution of the cluster projected on the sky. The measured total mass turns out to be much greater than that provided by the luminous component. Therefore, in our current understanding, dark matter surrounds galaxies and galaxy clusters, forming a halo that envelopes the visible matter.

The determination of the distribution and the amount of dark matter in the Universe has received significant attention in the recent years, representing one of the most fundamental aspects of cosmology. This thesis has the final goal of contributing to the estimation of the amount of Dark Matter in the Universe.

1.1.5 Λ CDM MODEL

In what follows, cosmological simulations of the Universe will represent a necessary tool for carrying out our work. Every simulation of the formation of the structures we observe today must be based on a cosmological model.

Among the several proposed models, the concordance one is the flat Λ CDM, where Cold Dark Matter particles (“cold” refers to particles travelling with non-relativistic velocities), dominate the mean matter density. This model contemplates a flat Universe in accelerated expansion, and the cosmological constant Λ is the dominant component. The ordinary matter accounts for only $\approx 4\%$ of the total matter of the Universe, while the rest is in form of CDM. This scenario is strongly supported by several observations that can constrain the cosmological parameters.

The cosmic microwave background (CMB) is the leftover radiation emitted by the hot plasma in the early Universe. The measurements of the CMB anisotropies give constraints on the curvature of the Universe. Different experiments as WMAP (Spergel et al., 2007), COBE (Bennett et al., 1996) e BOOMERANG (MacTavish et al., 2006) find the condition

$$\Omega_M + \Omega_\Lambda = 1.00 \pm 0.02, \quad (1.20)$$

which, together with equation (1.16), implies $\Omega_k = 0$, i.e. that the Universe is flat.

The angular power spectrum of the CMB temperature fluctuations contains also information on the baryonic matter content in the Universe gives a baryons density (Spergel et al., 2007)

$$\Omega_b h^2 = 0.020 \pm 0.001. \quad (1.21)$$

This value is in agreement with the prediction from the study of the primordial abundances of light elements, which constrains the baryons density in the range (Serpico et al., 2004)

$$0.018 < \Omega_b < 0.023. \quad (1.22)$$

The SNe Ia observations can constrain a combination of Ω_Λ and Ω_M , and the matter content of the largest clusters of galaxies is expected to provide a good estimation of Ω_M . By combining these results with the CMB data, the best-fit values are around $\Omega_\Lambda \approx 0.7$ and $\Omega_M \approx 0.3$ (Perlmutter et al., 1999). Figure 1.4 summarizes the constraints on the contributions of matter and cosmological constant in the Universe.

1.2 LARGE SCALE STRUCTURES

Astronomical observations over the last century have revealed the existence of inhomogeneities and structures on all scales studied so far. The distribution of luminous matter is in fact highly non-uniform and it is concentrated on the scale of galaxies (kiloparsecs), clusters of galaxies (megaparsecs), and a network filaments (tens of megaparsec) interconnecting galaxies, groups and clusters. As it will be clear in the next sections, an important part of this thesis is dedicated to study large scale structures and their motion, with the main goal of measuring the mass of the most massive ones, the clusters of galaxies.

In general, a large scale structure is defined as the structure or inhomogeneity of the Universe on scales larger than that of a galaxy. The scenario of large scale structure formation is believed to begin from initial fluctuations in the density of any component of matter (dark matter, baryons, radiation) that arise in the very early universe. Those fluctuations have grown through gravitational instability into the structures we observe today (Peebles, 1980; Bahcall, 1997). The formation process is hierarchical: the first perturbations to collapse are the smallest-scale ones,

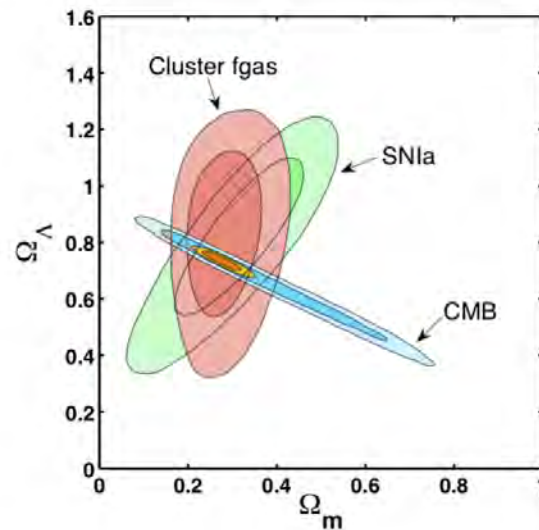


Figure 1.4 Cosmological constraints reported by showing the 1 and 2σ confidence constraints in the $(\Omega_M, \Omega_\Lambda)$ plane from the Chandra f_{gas} (red contours), CMB data (blue contours) and SNIa data (green contours). The inner, orange contours show the constraint obtained from all three data sets combined. Figure from (Allen et al., 2008).

and then the small-scale objects merge and form larger structures through a continuous assembly mechanism. The observations of the CMB give a snapshot of what the universe looked like at the time of the initial fluctuations (corresponding to $z \approx 1000$).

Extensive galaxy redshift surveys progressed over the last two decades, as the 2-degree Field Galaxy Redshift Survey (2dFGRS) (Colless et al., 2001) and the Sloan Digital Sky Survey (SDSS) (Abazajian et al., 2009), provide the current maps of the large scale structure distribution, and reveal a complex network: galaxy clusters are at the nodes of galactic filaments and sheets, which act as the transport channels along which matter flows into the equilibrated halos. These overdense structures surround nearly empty regions, called voids. For example, Figure 1.5 shows a slice of the universe as reconstructed from the 2dFGRS.

Cosmological numerical simulations of the growth of cosmic structure have been developed, in order to reproduce in detail the process that leads from the young Universe to the rich cosmic web we observe today (Efstathiou et al., 1985). Such simulations start at a sufficiently early epoch, when density fluctuations are still small, and follow the evolution of the collisionless dark matter component only, or together with the normal baryonic matter. Initial conditions have to be set as input, and the equations governing the astrophysical formation processes are solved numerically. The initial conditions depend on the adopted cosmological model of structure formation. The main elements involved are the background cosmology (a choice of Ω_M , H_0 , Ω_Λ), an initial fluctuation spectrum, a statistical distribution of fluctuation (often assumed to be gaussian), the proportion of particle species (hot or cold dark matter, baryonic).

Simulations show that in a Λ CDM Universe, the dark matter component drives the gravi-

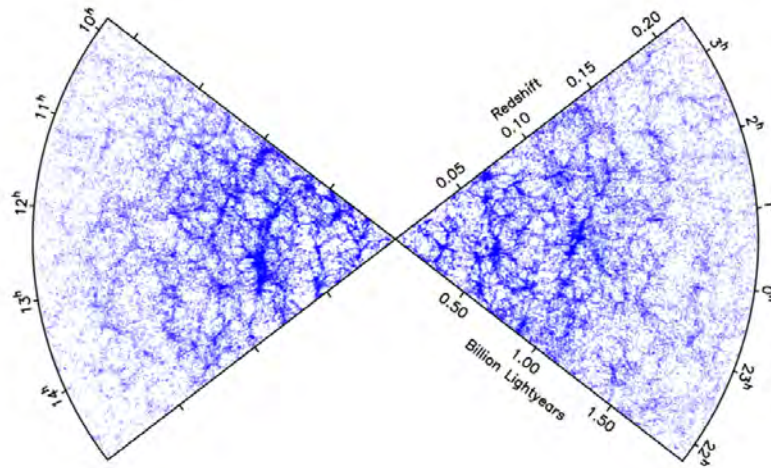


Figure 1.5 A slice of the universe as reconstructed from the 2dFGRS. The survey maps the distribution of matter within a section of the sky, by combining redshift and angular position data. The figure shows the large scale structure of the universe, made up of clusters, filaments and voids (Colless et al., 2001).

tational collapse and the hierarchical accretion of smaller systems. The first stage of the dark matter collapse is a sheet-like configuration, and subsequently the collapse continues toward elongated filaments, which eventually produce compact and virialized dark matter halos. The luminous matter follows the dark matter, and subsequently, galaxies and galaxy clusters form at the centres of the dark haloes by cooling and condensation of baryons. This picture give rise to the present observations of the cosmic web.

In Figure 1.6 the time evolution of the largest halo in Millenium-II simulation is shown, for different co-moving scales (Boylan-Kolchin et al., 2009). The simulation is made in the Λ CDM cosmology.

1.3 GALAXY CLUSTERS

The work presented in this thesis is aimed at measuring the mass of galaxy clusters. In this section I therefore review the main properties of these objects.

Galaxy clusters occupy a special position in this hierarchical scenario, as the most extended and most recently formed systems in the Universe, which are held together by their own gravity. Their masses cover a range from roughly $10^{13} M_{\odot}$ to over $10^{15} M_{\odot}$, and their spatial size spreads over 1 – 3Mpc. Dark matter represents $\approx 80\%$ of the total matter content in clusters. Stars and galaxies, which emit at visible wavelengths, make up only for a few percent of the whole mass content of clusters (3 – 5%). The most massive visible component is in diffuse, hot gas (15 – 25%), (Kellogg et al., 1971a; Gonzalez et al., 2007).

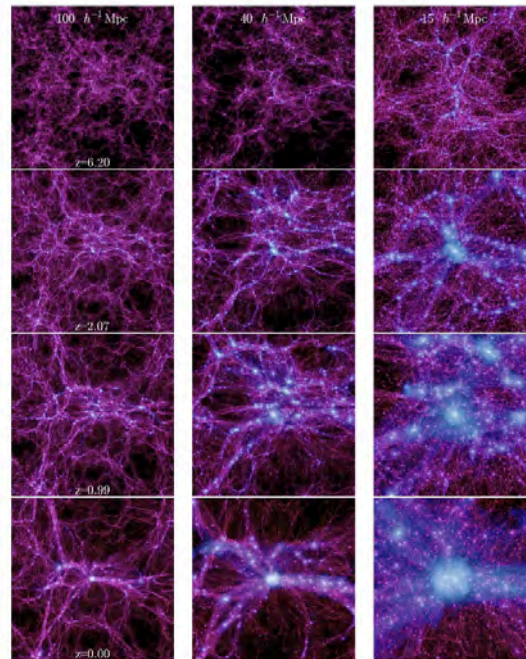


Figure 1.6 Time evolution of the largest FOF halo at $z = 0$ in the Millennium-II Simulation (Boylan-Kolchin et al., 2009). The halo is shown at three co-moving scales (from left to right: $100, 40,$ and $15h^{-1}$ Mpc, with thickness $15, 10,$ and $6h^{-1}$ Mpc) and at four different cosmological epochs (from top to bottom: $z = 6.2, 2.07, 0.99$ and $0.$)

When observed with optical telescopes, clusters of galaxies appear as overdensities of galaxies in an approximately spherical region (Abell, 1958; Zwicky et al., 1961). The X-ray astronomy revealed that galaxy clusters are strong emitters of photons with energies of the order of KeV, due to hot intra-cluster medium (ICM) (Gursky et al., 1971; Kellogg et al., 1971b). The X-ray emission is a very powerful technique to identify clusters up to large cosmological distances. The hot ICM electrons emitting in X-rays also change the intensity of the cosmic microwave background (CMB) radiation via inverse Compton scattering. This distortion in the CMB spectrum is called thermal Sunyaev-Zel'dovich effect (Sunyaev & Zeldovich, 1980). Therefore, measurements of the intensity or temperature fluctuation of the CMB allows to detect clusters at very large distances. The total gravitational potential of clusters (due to both visible and dark matter) causes the deflection of light rays coming from distant galaxies, leading to distortions in the shapes of these sources. The gravitational lensing effect makes the background galaxies appear as arcs curved around the cluster center. The gravitational lensing is therefore an important tool for identifying the presence of clusters and measuring their total mass (Mandelbaum et al., 2010).

Figure 1.7 is a example of the observation of the galaxy cluster Abell 1689 with different methods.

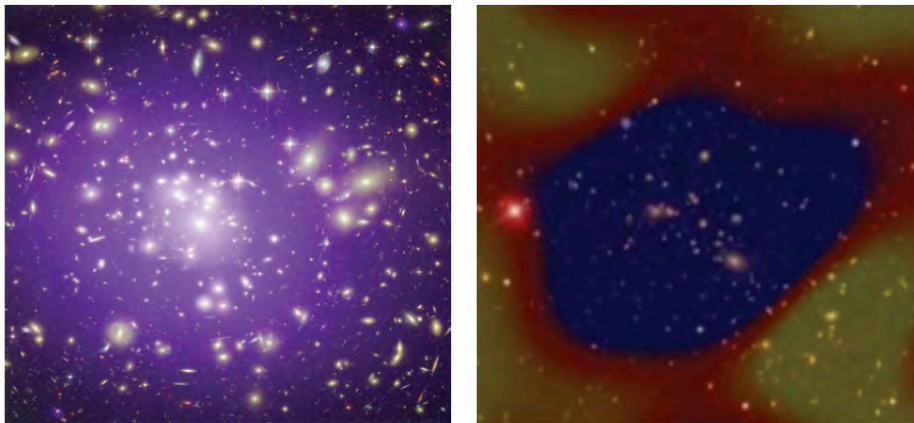


Figure 1.7 Left panel: optical, X-ray and gravitational lensing image of the galaxy cluster Abell 1689. Right panel: Sky Survey with the superimposed map of the temperatures of the Cosmic Microwave Background observed by the Sunyaev-Zeldovich array (SZA). Figure from (Borgani & Kravtsov, 2011)

1.4 DARK MATTER HALOES AROUND GALAXY CLUSTERS

As described before, galaxy clusters are surrounded by large halos made of dark matter, which, as a first approximation, are commonly described as spherical and isolated from their surroundings. The properties of dark matter halos can be studied by performing high-resolution cosmological simulations. An important feature that emerges is that these systems seem to achieve a final state of equilibrium, displaying nearly universal density profiles.

Navarro, Frenk and White found that the density profiles of halos in CDM simulations, can be fitted by the same formula, independently of their mass. The NFW profile reads as (Navarro et al., 1996)

$$\rho(r) = \frac{\rho_s}{\left(\frac{r}{r_s}\right) \left(1 + \frac{r}{r_s}\right)^2}, \quad (1.23)$$

parametrized by a characteristic length r_s , the scale radius, at which the logarithmic slope of the profile is $d \ln \rho / d \ln r = -2$, and the scale density $\rho_s = \rho(r_s)$. Within the scale radius, the DM density goes as $\rho \propto r^{-1}$, while beyond r_s the radial behavior is $\rho \propto r^{-3}$.

Figure 1.8 shows the density profiles of simulated dark matter halos, together with the fits of the form given in equation (1.23).

After the NFW work, several other functional forms have been proposed (for example Moore et al. (1999)), that can fit better the halos of higher resolution numerical simulation, both in the very inner and in the outer regions.

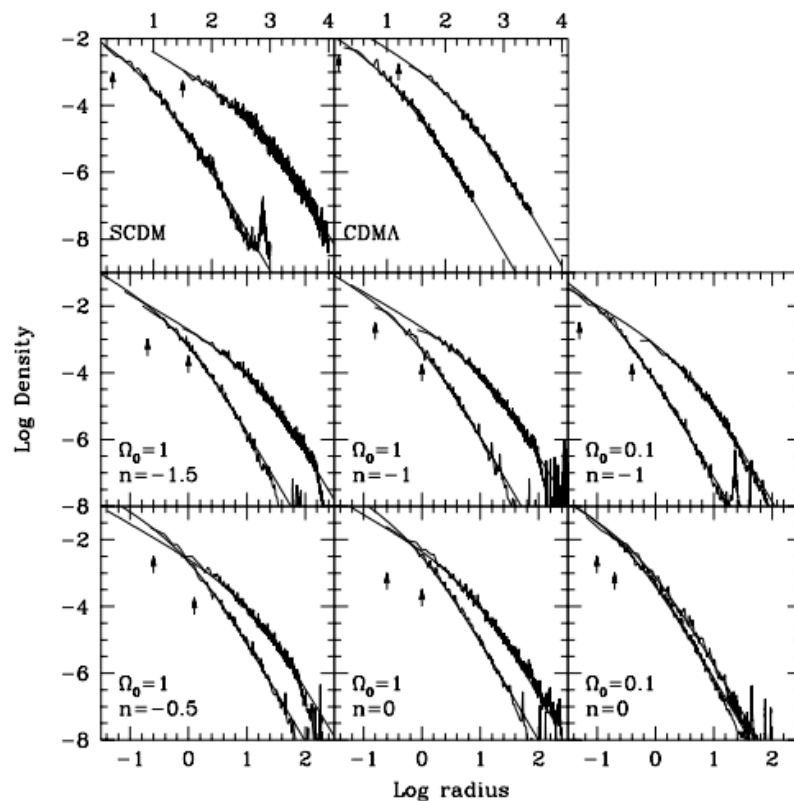


Figure 1.8 Density profiles of simulated dark matter halos. The different panels correspond to simulations for different cosmologies. Each panel shows the least and the most massive halos in each simulation (least massive to the left). Solid lines are the fits of the profiles to the NFW universal form. Figure from Navarro et al. (1996).

The majority of these different results can be reassumed in a compact universal form, the generalized NFW profile (Coe, 2010)

$$\rho(r) = \frac{\rho_s}{\left(\frac{r}{r_s}\right)^\alpha \left(1 + \frac{r}{r_s}\right)^{\beta-\alpha}}, \quad (1.24)$$

where the inner and the outer slopes, α and β , are not universal, but represent free parameters that can vary from halo to halo.

1.5 DYNAMICS OF GALAXY CLUSTERS

We are going to study galaxy clusters from the dynamical point of view, and we will propose a new formalism to describe the non fully equilibrated external regions. This section is a summary of the present status of our understanding of the clusters dynamical state, from both the theoretical and observational point of views, and the results obtained from cosmological simulations.

Virialization is the end stage of any collapsing structure. When a cosmological structure is virialized, the merging process of matter has finished, and the object is gravitationally bound

and stable. Galaxy clusters are the most recent objects that had the time to reach this state, where all the matter components form a virialized system: the gas reaches hydrostatic equilibrium, meaning that its pressure balances the gravitational force, while galaxies and dark matter are in dynamical equilibrium, meaning that their kinetic energy is balanced by the gravity of the cluster. Nevertheless, in the majority of galaxy clusters we observe today, the formation process is still ongoing: only the inner core of clusters is actually relaxed, while the outskirts still contain matter inflowing into the inner region. The presence of substructures surrounding virialized clusters emerges from several observations (Brown & Rudnick, 2011; Ettori & Molendi, 2011). Figure 1.9 for example represents an image of the Coma cluster in X-ray, clearly showing subgroups outside the inner virialized core.

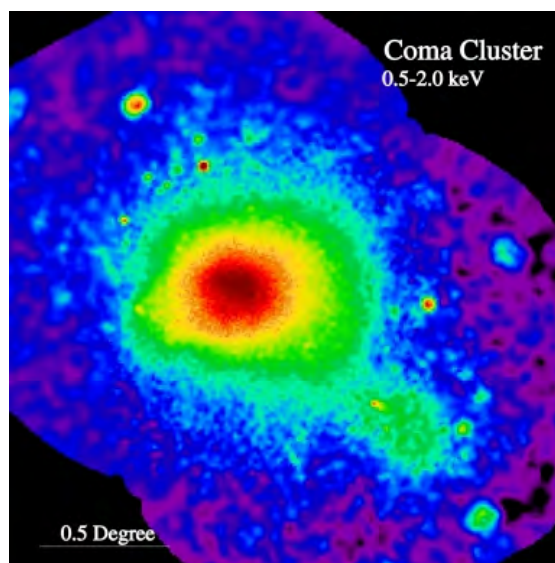


Figure 1.9 The Coma cluster in X-ray. The image shows the merging of the larger, brighter central cluster and the fainter group of galaxies to the lower right. The field is 2.7 degrees wide by 2.5 degrees high. Image credit: Rosat.

The dynamics of a cluster is thus characterized by a smooth transition from the region where the condition of equilibrium holds to the region where matter is infalling and the description of the dynamical state is more complicated. For this reason, defining the border of the sphere within which the cluster is in equilibrium is important, both in observations and in simulations, although it is not an easy task. The radius that confines the equilibrated cluster and separates it from the outskirts is called *virial radius*. The most common way to define the relaxed halo is on the basis of the spherical collapse model (Gott (1975); Gunn (1977)). Within the spherical model framework, the virial radius of every halo at redshift z is the one that encloses a fixed overdensity of Δ_{vir} times the critical density of the Universe

$$\rho(r_{\text{vir}}) = \frac{3M(r_{\text{vir}})}{4\pi r_{\text{vir}}^3} = \Delta_{\text{vir}} \rho_c. \quad (1.25)$$

The quantity Δ_{vir} is a function of the cosmology and the redshift. It is quite common to use $\Delta_{\text{vir}} \approx 200$, and therefore, $r_{\text{vir}} = r_{200}$. The total mass of a halo is defined as the *virial mass* $M_{\text{vir}} = M(r_{\text{vir}})$ in equation (1.25).

In the virialized sphere, the dynamics of galaxy clusters is well described by the *Jeans equations*, which rely on the assumption of a steady-state and spherical system. Since the spherical Jeans equation is the starting point of our work described in the next sections, here I show the formalism behind its derivation.

1.5.1 THE JEANS EQUATION FOR SPHERICAL SYSTEMS

In this section I derive the Jeans equation for a cluster of galaxies, approximated as a spherical system.

A galaxy cluster can be assumed to form a collisionless dynamical system, in which the motion of all the constituents is determined by the overall potential of the system. Dark matter particles are expected to have weak interactions at most, and thus the dark matter fluid is effectively collisionless. Gravitationally interacting stars in a galaxy and galaxies in a galaxy cluster are also collisionless.

The Jeans equations are thus derived by considering a system of identical, collisionless particles in six-dimensional phase-space $d^3x d^3v$. For such a system, the probability that at a given time, a randomly chosen particle has phase-space coordinates in a given range, is described by the distribution function $f(\mathbf{x}, \mathbf{v}, t)$. The collisionless Boltzmann equation states that (Binney & Tremaine, 2008)

$$\frac{\partial f}{\partial t} + \sum_{i=1}^3 \left(v_i \frac{\partial f}{\partial x_i} + \frac{\partial \Phi}{\partial x_i} \frac{\partial f}{\partial v_i} \right) = 0, \quad (1.26)$$

where $\Phi(x)$ is the Newtonian gravitational potential. The first-order Jeans equation, is obtain by integrating the Boltzmann equation over velocities.

In the standard derivation, the Jeans equation is developed under the assumption of dynamical equilibrium. Within this approach, the overall infall motion of matter towards the cluster center is not taken into account. The hypothesis of equilibrium can be expressed with the conditions

$$\bar{v}_i = 0, \quad (1.27)$$

where \bar{v}_i is the mean velocity in the i th direction, and

$$\frac{\partial}{\partial t} = 0, \quad (1.28)$$

which states that any partial time derivative of any function is identically zero. This approach has been widely adopted so far in literature, as it is simpler to develop and the results are easier to handle.

Moreover, clusters are approximate by spherical objects. This quite strong assumption allows to describe the three dimensional cluster mass, density and temperature distributions as radial profiles. From now on, our spatial coordinate system is thus the spherical one (r, θ, ϕ) .

These conditions yields the following stationary Jeans equation (Binney & Tremaine, 2008) :

$$-\rho \frac{d\Phi}{dr} = \frac{d\rho \bar{v}_r^2}{dr} + \frac{\rho}{r} \left(2\bar{v}_r^2 - \bar{v}_\theta^2 - \bar{v}_\phi^2 \right). \quad (1.29)$$

Here ρ is number density of the tracer, \bar{v}_i^2 is the second moment of i th velocity component and $\Phi(r)$ is the total gravitational potential.

We can introduce the velocity anisotropy parameter β as

$$\beta = 1 - \frac{\overline{v_\theta^2}(r) + \overline{v_\phi^2}(r)}{2\overline{v_r^2}(r)}. \quad (1.30)$$

The general expression for the second-order velocity moments is

$$\overline{v_i^2} = \sigma_i^2 + \overline{v_i^2}, \quad (1.31)$$

where σ_i^2 are the velocity dispersions.

Given equation (1.27), in the case of steady-state equilibrium, the second-order velocity moments are all equal to the velocity dispersions in the corresponding direction

$$\overline{v_i^2} = \sigma_i^2. \quad (1.32)$$

The velocity anisotropy can be thus written in terms of the velocity dispersions as

$$\beta = 1 - \frac{\sigma_\theta^2(r) + \sigma_\phi^2(r)}{2\sigma_r^2(r)}. \quad (1.33)$$

For purely circular orbits, $\sigma_r = 0$ and $\beta = -\infty$, whereas for purely radial orbits, $\sigma_\theta = \sigma_\phi = 0$ and $\beta = 1$. For isotropic motion $\sigma_r = \sigma_\theta = \sigma_\phi$, one must have $\beta = 0$.

In terms of the anisotropy parameter, the equation (1.29) reads

$$-\rho(r) \frac{d\Phi}{dr} = -\rho(r) \frac{GM(r)}{r^2} = \frac{d(\rho\sigma_r^2)}{dr} + 2 \frac{\beta}{r} \rho\sigma_r^2, \quad (1.34)$$

where $M(r)$ is the total mass distribution of the system. Thus, the Jeans equation relates the total mass of the cluster to the velocity dispersion of the galaxy members.

From kinematical observations of a cluster one can measure its velocity dispersion as function of the distance from the center, and model it by using equation (1.34). This corresponds to the standard procedure for determining the mass distribution from the dynamics (see section 2.3). In the most general case, the solution of equation (1.34) for σ_r is

$$\sigma_r^2(r) = \frac{1}{\rho(r)} \exp \left[-2 \int_0^r \frac{\beta(s)}{s} ds \right] \times \int_r^\infty \exp \left[2 \int_0^s \frac{\beta(\tilde{s})}{\tilde{s}} d\tilde{s} \right] \times \rho(s) \left[\frac{GM(s)}{s^2} \right] ds. \quad (1.35)$$

Observations provide only the component of the velocities along the line of sight and the projected distances from the cluster center. The line of sight velocity dispersion as function of the projected radius R is obtained by weighting by the density of the tracer and integrating along the line of sight

$$\sigma_{\text{los}}^2(R) = \frac{1}{I(R)} \int_R^\infty \left(1 - \beta \frac{R^2}{r^2} \right) \frac{\rho\sigma_r^2 r}{\sqrt{r^2 - R^2}} dr, \quad (1.36)$$

where the normalization is given by the surface density

$$I(R) = \int_R^\infty \rho \frac{r}{\sqrt{r^2 - R^2}} dr. \quad (1.37)$$

When observers model the velocity dispersion of clusters though equation (1.36), the tracer is represented by the visible matter, i.e. the galaxy members, and therefore the quantity ρ corresponds to the galactic density. Cosmological simulations are made of dark matter particles only, which, in that case, represent the tracer, and ρ corresponds to the total density of the system. We will apply equation (1.35) to all the particles in the simulated dark matter halos.

1.5.2 THE NON EQUILIBRIUM REGION OF GALAXY CLUSTERS

While the formalism in section 1.5.1 provides a coherent description of the dynamics in the virialized sphere of a galaxy cluster, the outer region is much more tricky to model. However, future deep measurements of clusters, including redshifts at large distances from the cluster center, will need to be supported by a detailed understanding of the cluster mass distribution at that scale. A description of the non-equilibrium region of galaxy clusters has been developed in this work, and chapter 4 is entirely dedicated to that.

The outskirts form a direct link between the cluster and the rest of the Universe. They are the regions where the structure formation process is still affecting the distribution of all the cluster components. On the other hand, outskirts of galaxy clusters are less subject to complicated astrophysical mechanisms, as radiative gas cooling, star formation and energy injection from active galactic nuclei. The dominant physical processes are instead related to the dynamics of collisionless dark matter and mainly driven by the gravitational potential of the system.

Observations of clusters in the outskirts are quite challenging. The X-ray surface brightness drops down at large distances from the cluster center like the square of the density, thus the information inferred from X-ray observations are quite limited. The SZ measurements are also less sensitive in clusters outskirts, as the pressure becomes low. At large distances from the cluster center, the gravitational lensing is much more affected by projection effect. See Reiprich et al. (2013) for a review on the outskirts of galaxy clusters.

Large and deep redshift surveys provide the line of sight velocity of clusters as function of the distance from the center on the sky, up to tens of virial radii. These observations allow to extend the dynamical analysis of galaxy clusters to the outer regions. Figure 1.10 represents the galaxy distribution in the redshift diagram for the Coma cluster. The inner relaxed cluster members ($r < (1 - 2) r_{\text{vir}}$) are easy to recognize. These data show a velocity dispersion different from zero also for $r > r_{\text{vir}}$, meaning the presence of an overall peculiar infall motion of galaxies around clusters, in the region $r_{\text{vir}} < r < 4 r_{\text{vir}}$. However, the observed velocity dispersion cannot be modelled by equation (1.35), since the equilibrium hypothesis does not hold at that scale. For larger distances, the velocity does not show a clear feature on the sky, due to the presence of background groups and small clusters and the projection effect.

High-resolution numerical simulations allow to predict the radial velocity pattern of particles belonging to a halo. In Figure 1.11 the result of the cosmological simulation performed by Cuesta et al. (2008) is shown. The three panels show the mean radial velocity profiles averaged in radial shells for low-mass, galaxy-size, cluster-size halos. The three lines in every panel correspond to the same velocity profile at different redshifts. From these figures, a quite clear picture of the radial velocity profile of DM halos in simulations emerges. In the inner parts, the average radial velocities are zero for all the three mass ranges. At very large distances, for all the halos, the expansion of the Universe takes over the peculiar velocity and the Hubble flow becomes the most remarkable feature. The transition from the inner region to the Hubble flow shows almost increasing radial velocity in the low-mass and the galactic-sized halos, i.e. these halos display a small signatures of infall in their surroundings. For cluster size halos, there is instead a significant region in the velocity distribution where galaxies have large negative velocities. This infall velocity pattern is particularly prominent in the region $r_{\text{vir}} < r < 4 r_{\text{vir}}$. In all cases, the infall depends on the redshift, being more pronounced for higher redshifts.

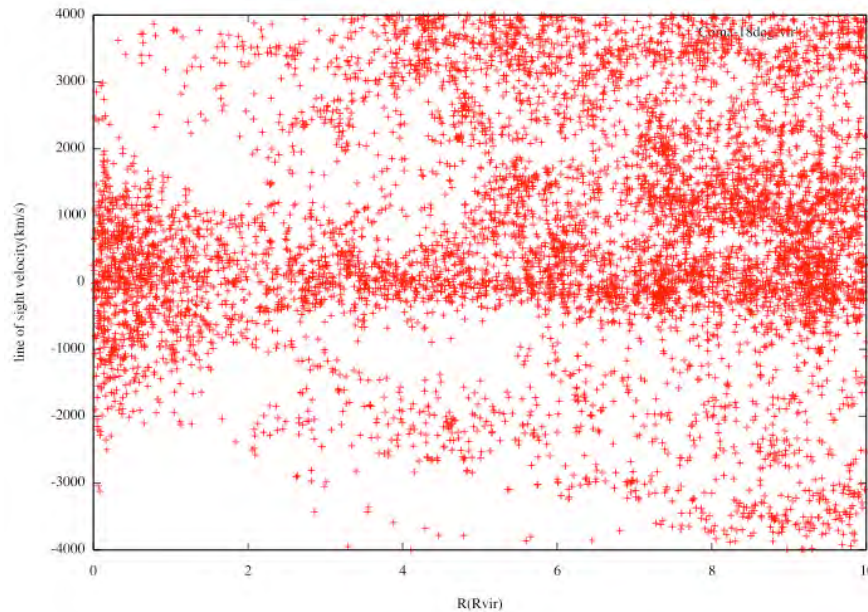


Figure 1.10 Spectroscopic observation of the Coma cluster up to ten virial radii: line of sight velocity as function of the projected distance from the cluster center. The data is taken from the SDSS survey.

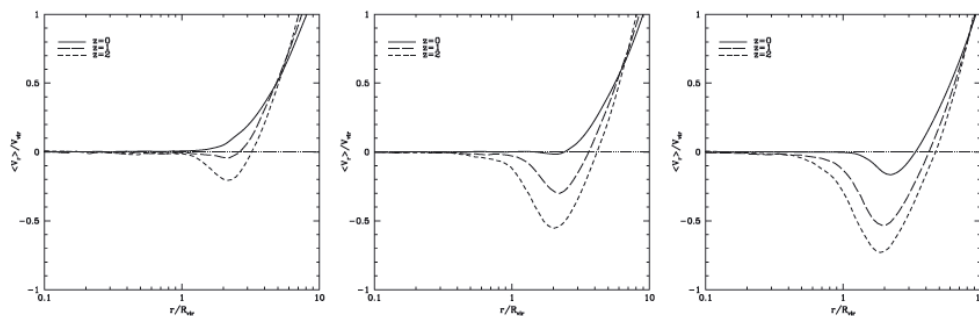


Figure 1.11 Result of cosmological simulations of dark matter only halos. The three panels show the mean radial velocity profiles averaged in radial shells for low-mass, galaxy-size, cluster-size halos. The three lines in every panel correspond to the same velocity profile at different redshifts. Figure from Cuesta et al. (2008)

1.6 GALAXY CLUSTERS AS COSMOLOGICAL PROBES

Galaxy clusters are important in cosmology, as they represent a confirmation of the abundance of dark matter and cosmological constant in the Universe. Many methods have been developed that use clusters as cosmological probes (Allen et al., 2011).

Under the assumption that clusters are large enough to be representative of the matter content of the Universe, the measurement of their mass distribution provides a robust tool for the determination of cosmological parameters. A classical method based on such assumption, for estimating the mass density of the universe Ω_M , consists in measuring the mass-to-light ratio

M/L , i.e. the ratio of the total cluster mass over the luminous mass (Popesso et al., 2007). Determining this ratio and multiplying it by the mean luminosity density of the Universe, gives an estimation of Ω_M . The M/L ratio has been measured for clusters of different masses. As displayed in Figure 1.12, the ratio increases as function of the mass, reaching a plateau at very high masses ($M \approx 10^{15} M_\odot$). This constant value of M/L corresponds to a matter density parameter of $\Omega_M \approx 0.3$ (Carlberg et al., 1996), as predicted by the Λ CDM model.

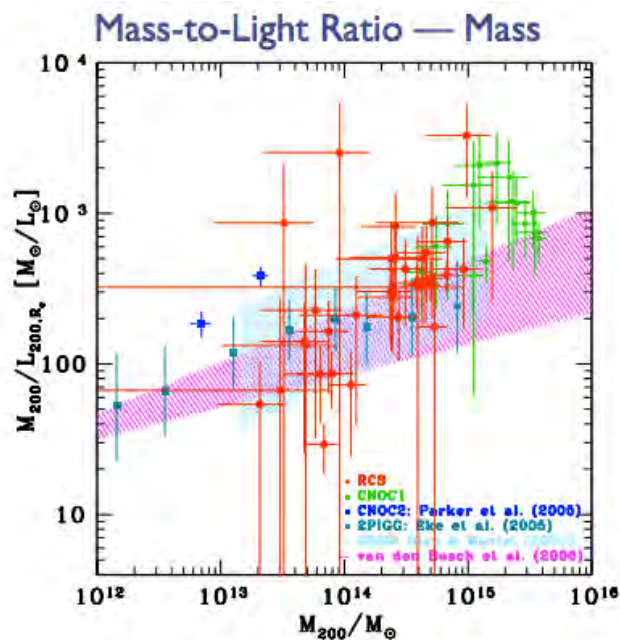


Figure 1.12 Mass to light ratio measured for different clusters, as function of the cluster mass.

The basic element of a cosmological model is the number density of halos as function of the mass and the redshift $n(M, z)$, called *cluster mass function* (Reiprich et al., 2001; Wen et al., 2010; Burenin & Vikhlinin, 2012). This can be obtained by collecting a large number of cluster mass estimations. The observed cluster mass function can then be compared with the predictions of the different cosmological models. For example, in Figure 1.13 (upper panels), the mass functions from data are compared with the ones predicted by the open Universe with no cosmological constant (left panel) and the Λ CDM model (right panel), for different redshifts. We see that the first under predicts the mass function for a redshift range of the data. The Λ CDM model is instead compatible with the data.

Allen et al. (2008) have developed a powerful technique to extract Ω_M from the measurements of the total mass and the X-ray mass of clusters. The fraction of gas in clusters, defined as

$$f_{\text{gas}} = \frac{\text{X ray gas mass}}{\text{total cluster mass}}, \quad (1.38)$$

is related to the cosmological parameters by

$$\Omega_M = \frac{b\Omega_b}{f_{\text{stars}} + f_{\text{gas}}}. \quad (1.39)$$

Therefore, by taking the estimation of Ω_b provided by the nucleosynthesis and the CMB studies and the value for b given by simulations, one can determine Ω_M . In the lower panels of

Figure 1.13, f_{gas} measurements for relaxed clusters are compared with the predictions for a flat Λ CDM model and a flat model with no cosmological constant.

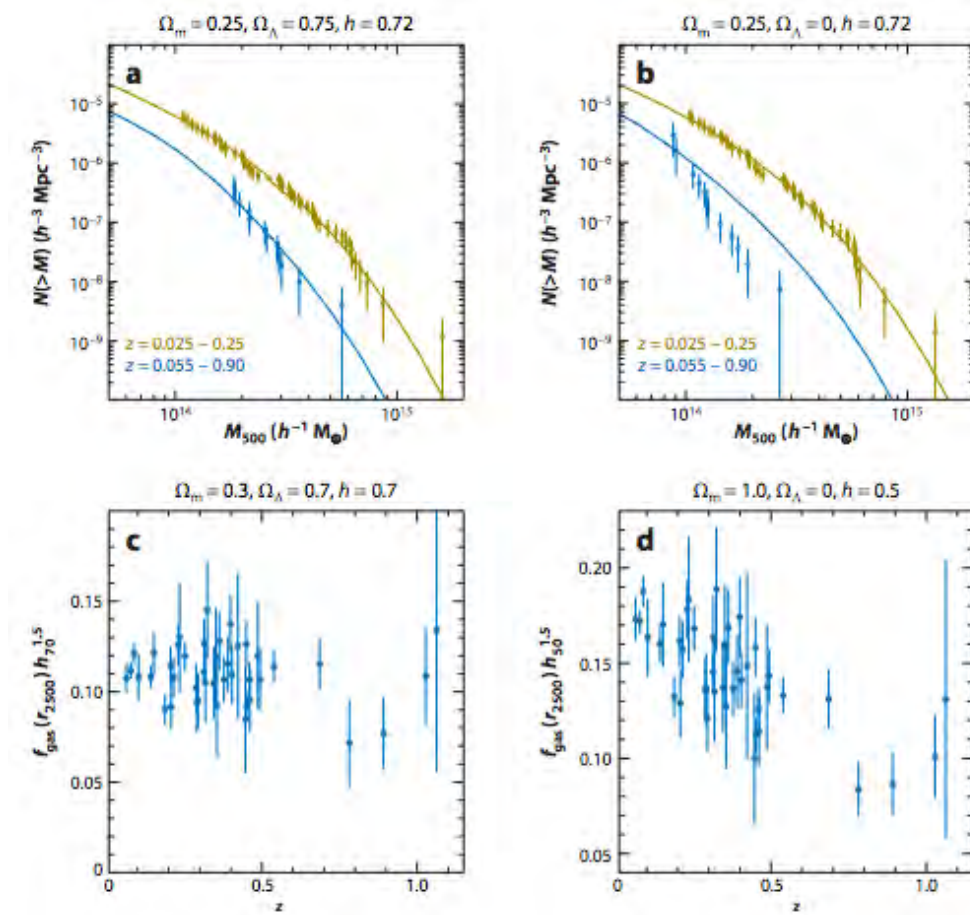


Figure 1.13 Upper panels: measured mass functions of clusters at low and high redshifts are compared with predictions of a flat, Λ CDM model and an open model without cosmological constant. Lower panels: f_{gas} measurements for relaxed clusters are compared for a flat Λ CDM model and a flat model with no cosmological constant. Figure from Allen et al. (2011).

In all the methods summarized in this section, an accurate estimation of the total cluster mass is crucial. Several techniques for measuring the cluster mass have been proposed. They all are affected by both theoretical and observational issues, which limit their accuracy and reliability, and they need to make important assumptions. We review the most common methods in the next chapter. The present thesis is devoted to contribute to the development of new cluster mass measurement methods, which can be complementary to the existent ones.

2

MASS ESTIMATION OF GALAXY CLUSTERS

Clusters of galaxies are one of the most important probes of the large scale structure formation and the overall dynamical state of the Universe. The measurement of the total mass of clusters provides a direct way to estimate the amount of dark matter in the Universe, as well as a tool for the determination of the nature and evolution of dark energy. However, determining the total cluster mass is not an easy task. Since most of the matter is in the form of dark matter, indirect ways for determining the total mass need to be developed.

Several methods have been proposed and applied to galaxy clusters, to constrain the total mass distribution at different scales. Strong lensing can provide constraints on very small scales ($< 0.1 h^{-1} Mpc$). The mass determination based on X-ray observations and the Jeans analysis both can be applied only within the virial radius, as they assume hydrostatic and dynamical equilibrium, respectively. So far, there are only two methods for deducing the cluster mass where the equilibrium assumptions break down: the weak gravitational lensing and the identification of caustics in redshift space.

Since all the existing methods rely on strong assumptions and are affected by observational limitations, a combination of different independent approaches and the development of new techniques are necessary. In this work, we approach the problem of determining the cluster mass by the study of the dynamics. Unlike most of the standard dynamical analysis, we look at kinematical data of galaxies very far away from the cluster center. We develop two novel methods. The first one allows to obtain a measure of the total cluster mass within the virial radius. The idea is to infer it only from the knowledge of the kinematic of galaxies far away from the center. The main key of this method is to detect and analyze the motion of galactic filaments and sheets flowing around the cluster. The second aims to extend the mass distribution measurement to the regions where galaxies are infalling and thus not in equilibrium. Therefore, this method is not based on the equilibrium hypothesis, and can be used to extract the mass up to three or four times the virial radius.

In this chapter, I will briefly summarize the main features of the most common standard mass determination methods, both in the equilibrium and non-equilibrium regions. I will focus in particular on the dynamical Jeans analysis, as it is strongly related to our work. I will describe the main features of our proposed methods.

2.1 THE VIRIAL THEOREM METHOD

The oldest method to measure the mass of galaxy clusters is based on the application of the *virial theorem* (Zwicky, 1933). It states that for a virialized and self-gravitating system, the mean

potential energy $\langle U \rangle$ is twice the negative kinetic energy $\langle T \rangle$ (Collins, 1978):

$$2 \langle T \rangle + \langle U \rangle = 0. \quad (2.1)$$

The kinetic energy averaged over all the particles in the system is given by

$$\langle T \rangle = \frac{1}{2} N m v^2, \quad (2.2)$$

where m is the particle mass, N the total number of particles in the system and $v^2 \approx \sigma^2$ the mean velocity dispersion of particles in the system. The total gravitational potential energy of a uniform sphere of mass M and radius R is:

$$\langle U \rangle = -\frac{3}{5} \frac{G M^2}{R}. \quad (2.3)$$

Substituting equations (2.2) and (2.3) into the virial theorem equation, one has

$$N m \sigma^2 = \frac{3}{5} \frac{G M^2}{R}, \quad (2.4)$$

and since the total mass corresponds to $M = n m$, one obtains the following relation between the total mass and the velocity dispersion:

$$M \propto \frac{\sigma^2 R}{G}. \quad (2.5)$$

Therefore, the virial theorem gives us a method to estimate the virial mass of a cluster, if we can observe the overall extent of the system R_{vir} and the velocity dispersion σ_r^2 :

$$M_{\text{vir}} \propto \frac{R_{\text{vir}} \sigma_r^2}{G}. \quad (2.6)$$

For a typical rich cluster, $\sigma_r \approx 10^3 \text{ km/s}$ and $R_{\text{vir}} \approx 1 \text{ Mpc}$, so the mass is of the order $M_{\text{vir}} \approx 10^{15} M_{\odot}$.

2.2 ANALYSIS OF THE ICM PROPERTIES

Clusters of galaxies are strong X-ray emitters. The total mass of galaxy clusters can be determined when observations in the X-ray band provide the intra cluster (ICM) properties, like density, temperature, and pressure (Sarazin, 1988).

The two crucial assumptions underlying any mass measurement based on the ICM temperature concerns the existence of hydrostatic equilibrium and spherical symmetry. Under those assumptions, the integrated total mass profile $M_{\text{tot}}(< r)$ is related to the ICM properties by the hydrostatic equation (Ryden, 2003):

$$M_{\text{tot}}(< r) = -\frac{k_{\text{B}} T_{\text{gas}} r}{G \mu m_p} \left(\frac{d \ln \rho_{\text{gas}}}{d \ln r} + \frac{d \ln T_{\text{gas}}}{d \ln r} \right), \quad (2.7)$$

where T_{gas} and ρ_{gas} are the gas temperature and density profiles, k_{B} the Boltzmann's constant, μm_p the mean molecular weight of the gas, and G the gravitational constant.

Thus, the total mass within a given radius depends on the gas temperature at that radius and on the temperature and density gradients, without any assumption on the dark matter distribution. In the inner relaxed region of galaxy clusters, within 1 – 1.5 virial radii, measurements

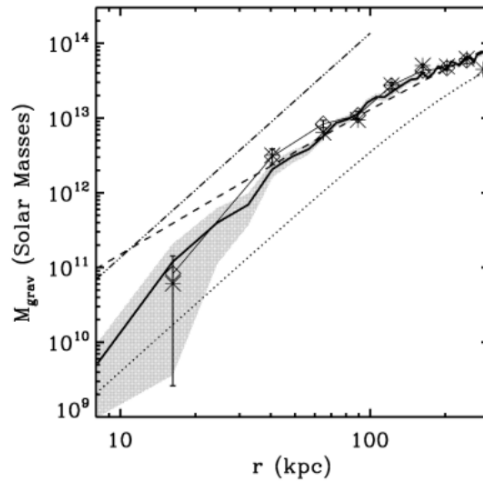


Figure 2.1 Gravitational mass profile of Abell1795. The mass is constrained from the deprojection analysis of the spectra, assuming that the X-ray emitting gas is in hydrostatic equilibrium (diamonds) and from the spatial deprojection of the X-ray surface brightness (solid line). The asterisks are the total mass values obtained from the spatial deprojection when the X-Ray centre is fixed on the cD galaxy. These values are compared with the best-fitting results on Rosat PSPC data using a β -model (dotted line) and a gas NFW model (dashed line). The three-dots-dash line indicates the upper limit from an assumed tidal shear in the $H\alpha$ filament due to the central cluster potential. Figure from Ettori et al. (2002a).

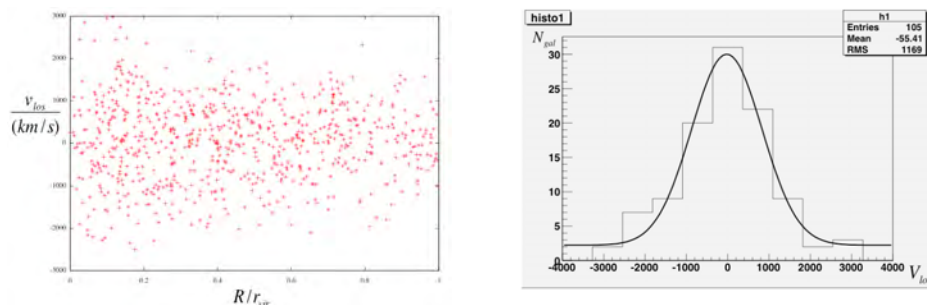
of gas temperature and density are resolved with high enough accuracy to allow accurate mass estimations with the X-ray analysis. In Figure 2.1, the gravitational mass distribution of the cluster of galaxies Abell1795 is shown, obtained by Ettori et al. (2002a) with the X-ray analysis. A measurement of the intensity or temperature fluctuation of the CMB, i.e. the SZ effect measurement, can also be used to determine the total mass of clusters (Motl et al., 2005).

An important problem in the X-rays analysis is the deprojection of the observed two-dimensional profiles to the three-dimensional profiles that are involved in the hydrostatic equation. Moreover the hydrostatic equilibrium and spherical symmetry hypothesis affect the accuracy of this method when the cluster is not fully equilibrated or significantly non spherical. For example, Balland & Blanchard (1997) found an uncertainty of a factor of 2 for the mass of the Coma cluster derived from X-ray data, assuming hydrostatic equilibrium for the intracluster gas.

2.3 THE JEANS DYNAMICAL APPROACH

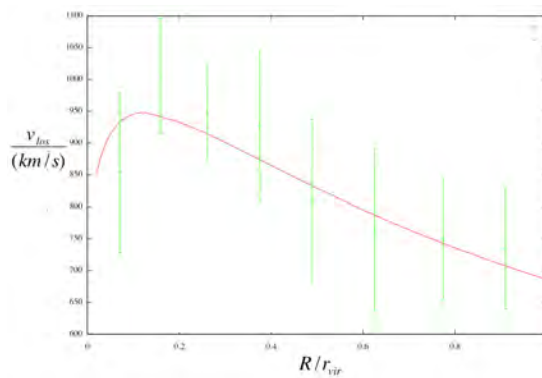
The mass distribution and internal dynamics of galaxy clusters are commonly studied by modeling their observed kinematics with the solutions of the Jeans equations. These equations relate the second-order velocity moments (or the velocity dispersions, if the mean streaming motion is known) directly to the density and the gravitational potential of the galaxies (the spherical Jeans equation has been derived in this thesis in section 1.5.1). The total mass of galaxy clusters can thus be determined by observing the projected phase-space distribution of galaxies. Specifically, the estimation of mass profiles with the standard Jeans analysis involves the modeling of the line-of-sight velocity dispersion of the tracer (i.e. galaxies in clusters): the predicted line-of-sight velocity dispersion in equation (1.36) is compared with the dispersions obtained from observed galaxy velocities and positions.

As an academic example, in Figure 2.2, I show the Jeans analysis I have performed for measuring the mass of the Coma cluster within the virial radius (Figure 2.2a). I used spectroscopic SDSS data for the galaxy members of the Coma cluster within $r_v \approx 2.7$ Mpc.



a: Spectroscopic observation of the Coma cluster up to the virial radius: line of sight velocity as function of the projected distance from the cluster center. The data is taken from the SDSS survey.

b: Number of galaxies as function of the observed velocity. The superimposed line is the best fit of a parametric function corresponding to a gaussian plus a constant background.



c: Green points: line of sight velocity dispersion obtained by the analysis of the data. Red line: fit to the data points with equation (1.36).

Figure 2.2 Jeans analysis on the Coma cluster.

One way to estimate the velocity dispersion, is to split the phase-space in radial bins and

look at the distribution of galaxies in each bin. I have then modeled the velocity distribution as a gaussian function and the background galaxies as an additive constant. As an example, in Figure 2.2*b*, I show the fit to the velocity distribution for the innermost radial bin. This procedure leads to the velocity dispersion data in Figure 2.2*c*. The Coma cluster mass has been obtained by fitting the observed velocity dispersion with equation (1.36), in the isotropic case ($\beta = 0$). The best value of the Coma mass from my analysis is $M_{\text{vir}} = 1.4 \times 10^{15} M_{\odot}$, with $\approx 30\%$ accuracy.

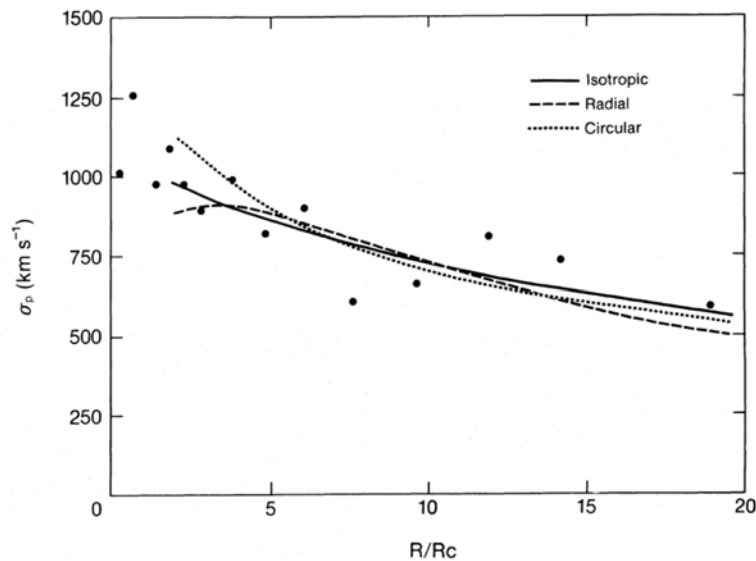


Figure 2.3 Projected velocity dispersion profiles for three very different Coma models. The dots are the projected velocity profiles for galaxies in Coma. The three curves correspond to models in which the galaxy orbits are isotropic, completely radial, and completely circular. Figure from Merritt (1987).

One step of the Jeans analysis is to measure the density distribution of the tracers, which needs to be inserted in equation (1.36). It can be extracted from a parametric fit to the number density of the observed galaxies. In the general case, the equation (1.36) still involves two unknown functions: $M(r)$ and $\beta(r)$. Therefore, the Jeans analysis is affected by the problem of the mass-anisotropy degeneracy: different combinations of $M(r)$ and $\beta(r)$ can lead to the same result for the line-of-sight velocity dispersion σ_{los} . This is shown in Merritt (1987), where they try different models to fit the velocity dispersion of the Coma cluster. Their result is reported in Figure 2.3. The Coma velocity dispersion is well reproduced by three very different models. Without information on $M(r)$ or $\beta(r)$, the only possible approach is to make some assumptions, either on the mass distribution or the anisotropy profile. For example in Girardi et al. (1998), they make the hypothesis that the galaxy number distribution traces the total mass distribution. They use three different samples of stacked halos. The clusters are divided in the three groups according to the shape of their profile and they use three different functional forms of $\beta(r)$ for the three cases. Their result is shown in Figure 2.4, where the right panels are the best fits for the velocity dispersions and the left panels show the corresponding best models for the anisotropy profile. In Biviano & Girardi (2003), they instead make no assumptions on the mass, but they assume isotropic orbits. They constrain the mass profile of a stack of clusters, by exploring

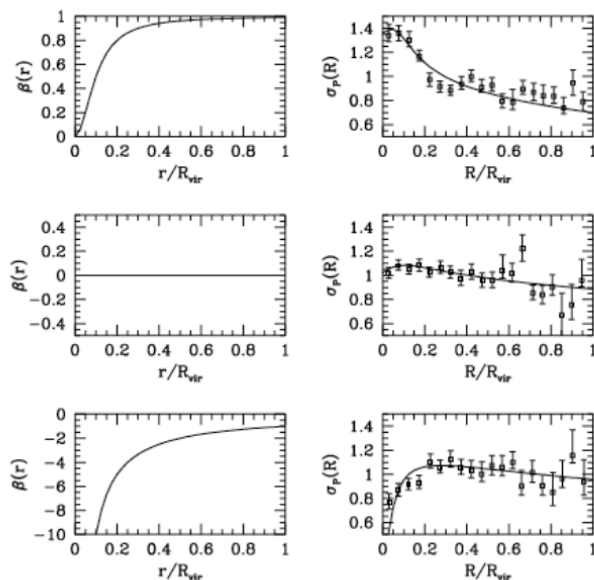


Figure 2.4 Clusters of three different types. Right panels show the normalized projected velocity dispersion σ_p as function of the normalized projected distance from the cluster center. The solid line represents the model for the velocity anisotropy parameter $\beta(r)$ shown in the corresponding panel on the left. Figure from Girardi et al. (1998).

models for the cluster mass density profile. They find three best models, which are consistent with data (see Figure 2.5).

Another way to break the degeneracy, is to make a joint analysis of independent observables, which can help to constrain either the mass or the anisotropy. Lokas & Mamon (2003) propose to look simultaneously at the velocity dispersion of clusters and their kurtosis, which is defined by

$$k_{\text{los}} = \frac{\overline{v_{\text{los}}^4}(R)}{\sigma_{\text{los}}^4(R)}. \quad (2.8)$$

The moment $\overline{v_{\text{los}}^4}$ of the velocity can be modelled by solving the fourth-order Jeans equation:

$$\frac{d(\rho v_{\text{los}}^4)}{dr} + \frac{2\beta}{r} \rho v_{\text{los}}^4 + 3\rho\sigma_r^2 \frac{d\Phi}{dr} = 0. \quad (2.9)$$

They parametrize the density distribution with a NFW profile, and consider β as a constant parameter. They obtain the result shown in Figure 2.6, where they report the best model that reproduces both the line-of-sight velocity dispersion of Coma and the kurtosis. Despite the joint

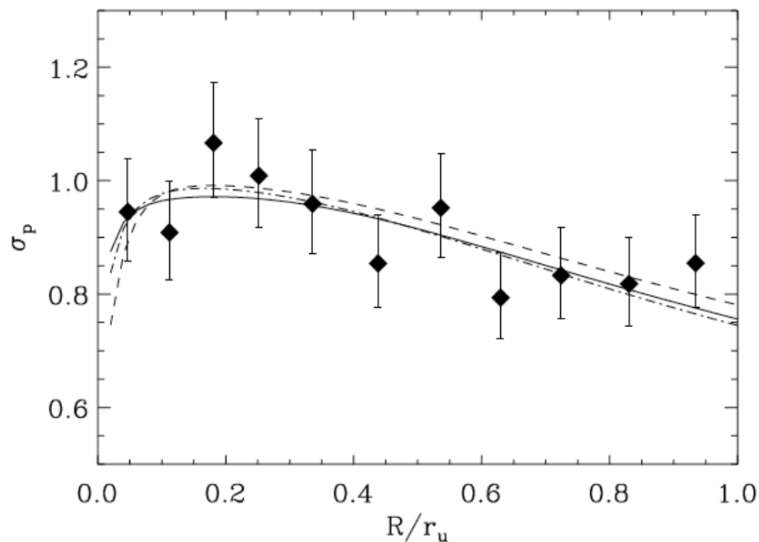


Figure 2.5 Predicted velocity dispersion profiles from the best-fit mass density models and the observed σ_p . The three different lines correspond to different parametric models for the total density profile. The figure is from Biviano & Girardi (2003).

analysis allows to determine the mass distribution and the anisotropy, they observe a strong degeneracy between the inner slope α and the concentration c in the NFW profile.

2.4 THE CAUSTIC METHOD

The caustic analysis is the only method proposed so far, that aims to extend the dynamical determination of the cluster mass profile beyond the virialization radius.

When observing the surrounding regions of virialized clusters in the redshift space, the infall pattern appears in a characteristic trumpet shape (see Figure 2.7). The boundaries of this trumpet are called caustics, and the caustic amplitude $A(R)$ is defined as the difference between the maximum and minimum line-of-sight velocity at the projected distance R from the cluster center.

Diaferio (1999) demonstrated that the caustic amplitude is related to the escape velocity of galaxies, when spherical symmetry is assumed. The escape velocities of galaxies directly depend on the gravitational potential of clusters by the formula

$$v_{esc}^2(r) = -2\Phi(r). \quad (2.10)$$

Therefore, the caustic amplitude can be used to estimate the mass profile of the cluster in the innermost part of the non-equilibrium region.

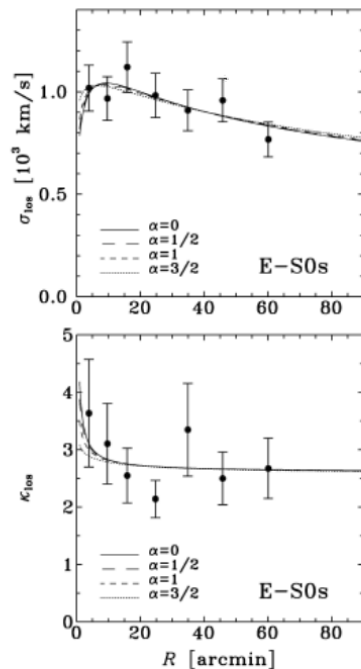


Figure 2.6 The best fitting line-of-sight velocity dispersion (upper panel) and kurtosis (lower panel) profiles of E-S0 galaxies in the Coma cluster. The dots represent the observed data. The figure is from Łokas & Mamon (2003).

They suggest that the three-dimensional cumulative mass can be estimated by

$$GM(< r) = \int_0^r A^2(R) F_\beta(R) dR, \quad (2.11)$$

where the function F_β is related to the anisotropy profile, as well as to the total potential, and is given by the relation

$$F_\beta(r) = -2\pi G \frac{\rho(r)r^2}{\phi(r)} \frac{3 - 2\beta(r)}{1 - \beta(r)}. \quad (2.12)$$

They find that, in a hierarchical clustering scenario, F_β is a slowly changing function of r , and therefore, they assume $F_\beta = \text{const}$. They also show that the value $F_\beta = 1/2$ provides accurate mass profiles both in N-body simulations and in real clusters, when compared with masses obtained with standard methods.

With this recipe, the equation (2.11) simplifies to

$$GM(< r) = \frac{1}{2} \int_0^r A^2(R) dR. \quad (2.13)$$

The equation (2.13) and the determination of the caustic curve, leads to the estimation of the

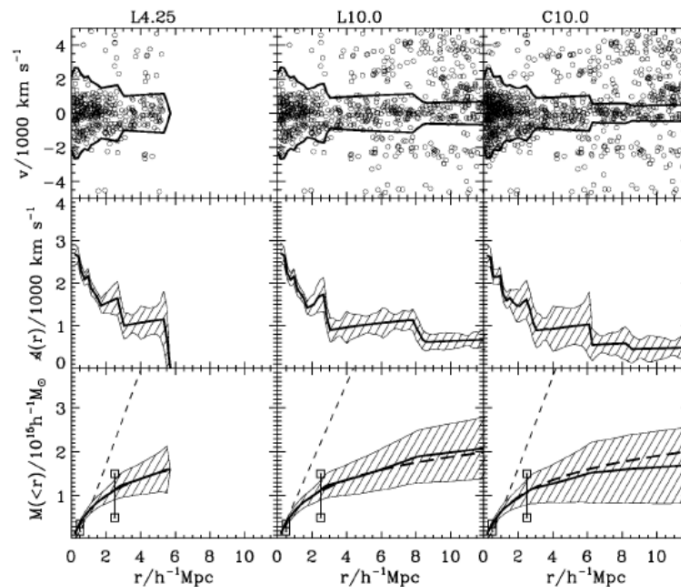


Figure 2.7 *Top panels:* Galaxy distribution in the redshift diagram of Coma for three galaxy samples of increasing size. The bold lines indicate the location of the caustic. *Middle panels:* Half of the distance between the caustics, that defines the amplitude $A(r)$ is shown. *Bottom panels:* The bold lines are the caustic mass profiles. The two error bars show the range of the X-ray mass estimates listed in Hughes (1989). The figure is from Girardi et al. (1998).

total mass distribution, independently of the anisotropy profile. The method only requires the galaxy positions and redshifts of galaxy in and around the cluster.

The caustic technique was tested on simulated data sample (Diaferio, 1999) and applied to the observation of many local clusters (Rines et al., 2003). The mass estimates obtained using this technique are consistent with those based on X ray and weak lensing observations (Diaferio et al., 2005). As an example, Figure (2.7) shows the analysis made on three galaxy samples of increasing size, belonging to the Coma cluster.

Even though the caustic method appears to be a powerful tool to constraint the cluster mass in the outskirts, it also suffers of some problems. The accuracy of this method strongly relies on the correct determination of the caustic curve, i.e. on the definition of the cluster's borders and the identification of the infalling galaxies in the phase-space. A precise caustic surfaces amplitude is achieved when a large number of galaxy members, in and outside clusters is available. Therefore, the method may be affected by uncertainties when applied to poorly populated clusters. Moreover, a crucial role is played by the selection of members and the interlopers removal. Thus, the main uncertainty is introduced by projection effects.

Another issue resides in the approximation made on the function F_β . Although it is very useful to make the analysis independent of the anisotropy profile, the parametrization of F_β , i.e. $\beta(r)$, with a changing function with r , might improve the results on the clusters mass estimation.

2.5 THE GRAVITATIONAL LENSING

The mass of galaxy clusters can be determined through the property of clusters acting as gravitational lens for distant background objects: the cluster mass distribution perturbs the paths of the light emitted by such objects, whose images appear distorted and magnified.

Due to the lensing effect, a source at a position β is observed at position x , that satisfy

$$\beta = x - \alpha(x), \quad (2.14)$$

where α is the deflection angle.

The resulting source's image is characterized by the *shear*, that quantifies the gravitational field of the lensing mass distribution and is responsible for the image distortion, and the *convergence*, that causes the image contraction. The convergence k is related to the surface mass density Σ of the lens by

$$k = \frac{\Sigma}{\Sigma_c}. \quad (2.15)$$

The critical surface density Σ_c in equation (2.15) is a geometric factor given by

$$\Sigma_c = \frac{c^2}{4\pi G} \frac{D_s}{D_L D_{LS} (1 + z_L)^2}, \quad (2.16)$$

where D_L , D_S and D_{LS} are angular diameter distances to the lens, to the source and between the source and the lens, respectively. The shear γ has two components, which are related to the second derivatives of the lensing potential by

$$\gamma_1 = \frac{1}{2} \left(\frac{\partial^2 \Phi}{\partial x_1^2} - \frac{\partial^2 \Phi}{\partial x_2^2} \right) \quad \text{and} \quad \gamma_2 = \frac{\partial^2 \Phi}{\partial x_1 \partial x_2}. \quad (2.17)$$

Therefore, a measure of the convergence and the shear allows to recover the lens potential, i.e. the cluster mass.

Two different types of lensing effects can be observed with clusters:

- *Strong lensing.* When the mass density of the cluster is bigger than the critical density ($\Sigma > \Sigma_c$), the presence of a distant source, such as a galaxy, produces elongated curves, called "giant arcs". The strong lensing is usually characterized by the production of multiple images from a single source.
- *Weak lensing.* In addition to the giant arcs, a cluster can also produce weakly distorted images of a large number of background galaxies. These images are called "arclets".

In the case of the strong lensing, the location of an arc provides a measure of the cluster mass within the circle traced by the long arc. Since it requires a high density of the lens, the strong lensing is suited for the study of the cluster density profiles in the inner regions ($< 0.1 h^{-1} \text{ Mpc}$). The weak lensing is instead caused by any density fluctuation, and therefore it can be used for the determination of the mass profile also in the outer regions of galaxy clusters. However, the weak signal from individual arclets needs to be statistically averaged over several sources. This feature limits the precision with which masses are determined.

Several techniques for measuring the mass distribution of clusters up to large distances from the cluster center, based on the application of weak lensing, have been developed (see e.g. Kaiser et al. (1995); Hoekstra et al. (1998); Lombardi & Bertin (1999)). The weak lensing methods suffer from the important problem of the mass sheet degeneracy. This means that

the projected mass profile can be determined only up to a degeneracy addition of an arbitrary constant, due to the projection effects. Assumptions on the mass distribution are needed in order to constrain the constant value. The advantage of this methods is that, in contrast to other dynamical technique for probing gravitational fields, no assumption needs to be made on the dynamical state of the matter.

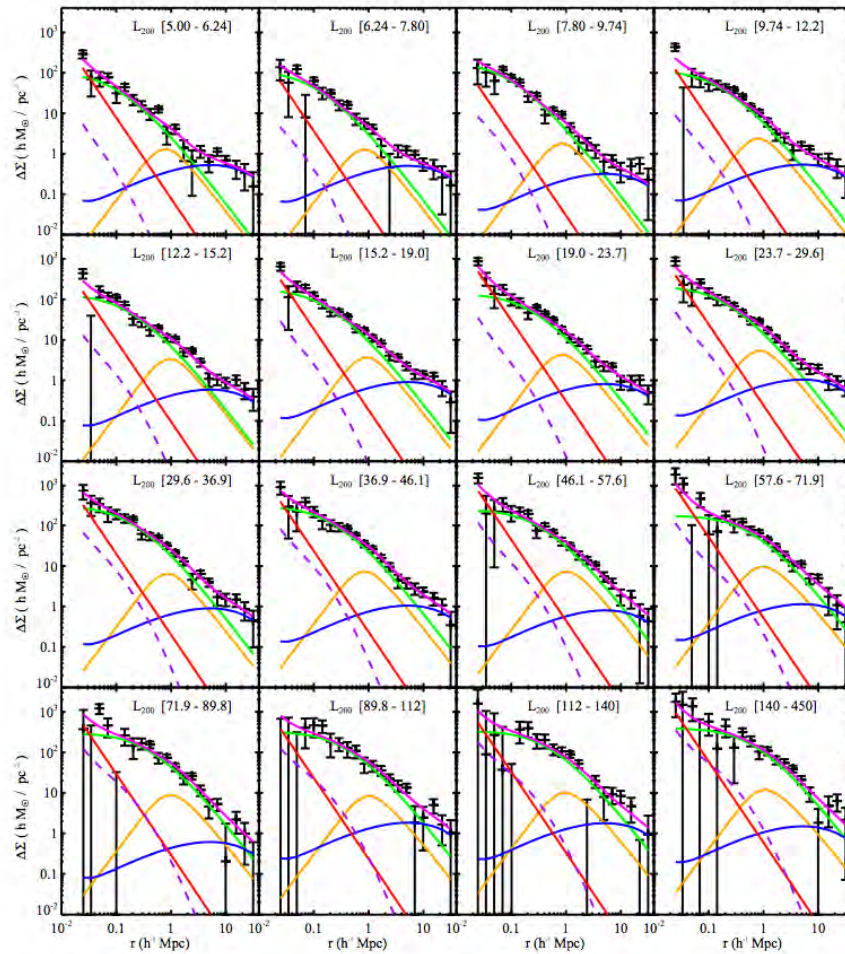


Figure 2.8 Lensing signal as a function of luminosity: halo model fits to the density profile of SDSS MaxBCG clusters, for 16 luminosity bins. For each bin a model is fitted (magenta), that consists of different components: the NFW halo profile (green), miscentered halo component (orange), the central BCG (red), neighboring halos (blue), and the non-linear contribution (purple dashed). Figure from Johnston et al. (2007).

Figure 2.8 shows the lensing signal as a function of luminosity L_{200} around clusters from the SDSS MaxBCG sample.

2.6 THIS THESIS: NEW APPROACHES TO THE CLUSTER MASS ESTIMATION

In this thesis we aim to implement new approaches for the determination of the total galaxy cluster mass. In particular, we propose two methods, both using dynamical arguments. They are based on an accurate analysis of the dynamics of galaxies in the non equilibrated outer region.

In section 1.5.2 we have discussed the non equilibrium dynamics of a galaxy cluster in its outskirts. Here we schematically summarize the feature of the radial motion of galaxies around a cluster up to very large distances from the center. The following description comes from combining the results of cosmological simulations with the informations from observations and theoretical models.

- In the equilibrated cluster, which corresponds to the sphere within the virial radius r_v , the mean radial velocity is settled around zero. This means that in the inner region there is no overall radial infall motion, and the approximation of equilibrium is valid. The dynamics of this region is described by the Jeans formalism.
- Both observations and simulations show that in the region $r_v < r \leq 4r_v$ the infall dominates. The mean radial velocity is indeed negative at that scale, reaching a minimum around $2 - 3r_v$. In this region, groups of galaxies and filaments are sitting. These structures are bound to the cluster but they have not yet reached the virial equilibrium. Therefore, the steady-state assumption behind the Jeans equation does not hold at this scale, and the dynamics cannot be described by the standard formalism.
- At the turnaround radius $r_t \approx 3 - 4r_v$ the total radial velocity is zero, meaning that the peculiar motion is balanced by the expansion of the Universe, that makes the galaxies move away from the cluster.
- For larger radii ($4r_v < r < 8r_v$) the mean velocity shows a positive increasing quasi-linear pattern. This is the transition region between the infall regime and the Hubble regime, dominant at the very large distances. In this region we expect to find filaments and sheets that are flowing away from the cluster, but they are still gravitationally affected by it. In fact, their motion is not a pure Hubble flow, but is instead perturbed by the gravitational potential generated by the presence of the massive cluster.
- When looking at the mean radial velocity for very large radii, $r > 8r_v$, the motion is asymptotically approaching the Hubble flow relative to the cluster center.

Our idea is to use the dynamics in the infall and the transition regions to determine the mass distribution of the cluster. However, the two methods we propose are quite different.

The first one is a quite new approach. It aims to measure the total mass of clusters within the virial radius, by using information on the dynamics in the transition region ($4r_v < r < 8r_v$). Compared to the several existing methods for measuring the virial mass, ours doesn't need to assume hydrostatic or dynamical equilibrium of the cluster, as only the outskirts needs to be analyzed. With the second one, we want to extend the standard Jeans approach to the infall region of galaxy clusters, in order to obtain the mass distribution up to $\approx 4r_v$. This method would be added to the only other two current techniques: the caustic and the gravitational lensing. As those, our method does not rely on the assumption of dynamical equilibrium.

In this following chapters I present the results and the current status of our work.

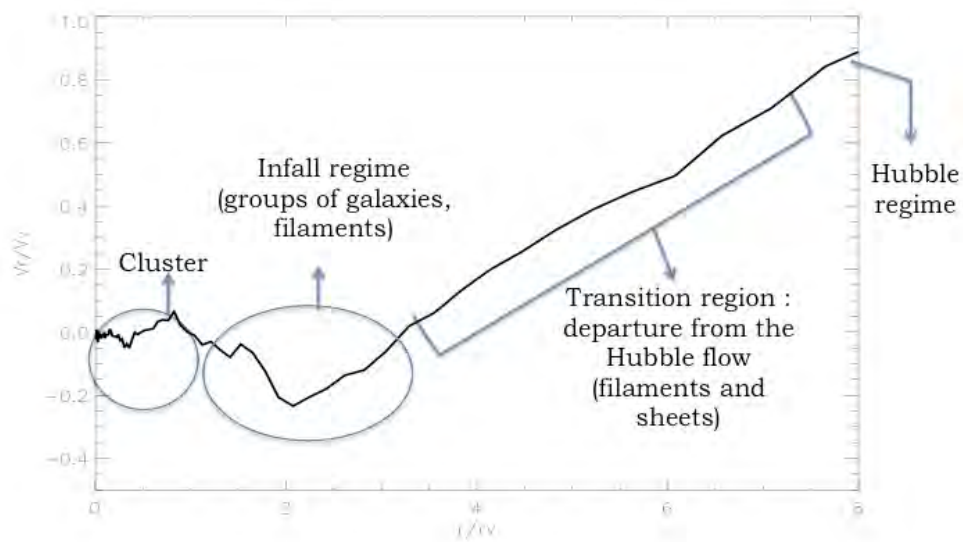


Figure 2.9 Mean radial velocity profile of a halo from cosmological simulations as function of the distance from the halo center. The different regions are indicated.

3

MASS ESTIMATION IN THE INNER REGION OF GALAXY CLUSTERS FROM THE OUTSKIRTS

A new method to measure the mass of galaxy clusters

Martina Falco¹, Steen H. Hansen¹, Radoslaw Wojtak¹, Thejs Brinckmann¹, Mikkel Lindholmer¹
and Stefania Pandolfi¹

¹ Dark Cosmology Centre, Niels Bohr Institute, University of Copenhagen, Juliane Maries Vej
30, 2100 Copenhagen, Denmark

Submitted to MNRAS, arXiv:1309.2950.

Abstract

The mass measurement of galaxy clusters is an important tool for the determination of cosmological parameters describing the matter and energy content of the Universe. However, the standard methods rely on various assumptions about the shape or the level of equilibrium of the cluster. We present a novel method of measuring cluster masses. It is complementary to most of the other methods, since it only uses kinematical information from outside the virialized cluster. Our method identifies objects, as galaxy sheets or filaments, in the cluster outer region, and infers the cluster mass by modeling how the massive cluster perturbs the motion of the structures from the Hubble flow. At the same time, this technique allows to constrain the three-dimensional orientation of the detected structures with a good accuracy. We use a cosmological numerical simulation to test the method. We then apply the method to the Coma cluster, where we find two galaxy sheets, and measure the mass of Coma to be $M_{\text{vir}} = (9.2 \pm 2.4) \times 10^{14} M_{\odot}$, in good agreement with previous measurements obtained with the standard methods.

3.1 SUMMARY

The virial mass of galaxy clusters can be measured in several independent ways, as mentioned in the previous chapter. They all need to make strong assumptions on the dynamical state of matter in the cluster and on the geometry of the system. The main ones are the steady-state hypothesis and the approximation of the cluster to a spherical system. A complementary approach, namely a comparison with results obtained from different techniques, is therefore fundamental for an accurate determination of clusters mass as well as for testing the reliability of such methods.

I have implemented and applied a new mass determination method, that, although it keeps the assumption of sphericity and is model dependent, does not need the hypothesis of equilibrium of matter within the cluster. The new feature of our method is that it only uses galaxies very far away (5-15 Mpc) from the cluster center to infer the virial cluster mass. The starting point is that, in the hierarchical scenario of structure formation, galaxy clusters are located at the intersection of large scale structures, such as one one-dimensional filaments and two-dimensional sheets. The idea is to extract the mass of a cluster from these surrounding structures. Such large scale objects move with a decelerated Hubble flow with respect to the cluster center, as the gravitational potential generated by the cluster mass is attracting them against the expansion. Cosmological simulations allow us to deduce a fairly universal quantitative relation between the velocity of these structures and the virial cluster mass. The velocity profile that we observe on the sky also depends on the orientation of the structures in 3D, and I also take this effect into account when implementing the velocity model.

The first step is naturally the detection of filaments and sheets in the environment of clusters, by using the velocities and positions of their galaxy members. The underlying argument is that if a filament or a sheet is close to be face-on and it has a coherent motion with respect to the cluster, it will appear as an overdensity in the phase space, forming a nearly linear pattern. We also require its galaxy members to be confined in a relatively small area on the sky.

Spectroscopic observations of the galaxies allow us to measure the line of sight velocity v_{los} of each galaxy. When fitting the velocity of galaxies in the detected structures with the universal model from simulation, one is able to determine the mass of the galaxy cluster, without even looking at the virialized part.

After testing the method on cosmological simulations, I have applied it to the Coma cluster data. We detect two galaxy sheets in the environment of the Coma cluster, and we used them to infer the Coma cluster virial mass.

All the details are described in this chapter.

3.2 INTRODUCTION

The picture of the large-scale structures reveals that matter in the Universe forms an intricate and complex system, defined as “cosmic web” (Zeldovich et al., 1982; Shandarin & Zeldovich, 1983; Einasto et al., 1984; Bond et al., 1996; Aragón-Calvo et al., 2010).

First attempts of mapping the three-dimensional spatial distribution of galaxies in the Universe (Gregory et al., 1978; de Lapparent et al., 1986; Geller & Huchra, 1989; Shectman et al., 1996), as well as more recent large galaxy surveys (Colless et al., 2003; Tegmark et al., 2004; Huchra et al., 2005), display a strongly anisotropic morphology. The galactic mass distribution seems to form a rich cosmos containing clumpy structures, as clusters, sheets and filaments, surrounded by large voids (van de Weygaert & Bond, 2008). A similar cosmic network has emerged from cosmological N-body simulations of the dark matter distribution (Bond et al., 1996; Aragón-Calvo et al., 2007; Hahn et al., 2007).

The large scale structures are expected to span a range of scales that goes from a few up to hundreds of megaparsec. Despite the many well-established methods to identify clusters and voids, there is not yet a clear characterization of filaments and sheets. Due to their complex shape, there is not a common agreement on the definition and the internal properties of these objects (Bond et al., 2010). Moreover, their detection in observations is extremely difficult due to the projection effects. Nevertheless, several automated algorithms for filament and sheet finding, both in 3D and 2D, have been developed (Novikov et al., 2006; Aragón-Calvo et al., 2007; Sousbie et al., 2008; Bond et al., 2010). Several galaxy filaments have been detected by eye (Colberg et al., 2005; Porter et al., 2008) and dark matter filaments have also been detected from their weak gravitational lensing signal (Dietrich et al., 2012). Powerful methods for the cosmic web classification, are based on the study of the Hessian of the gravitational potential and the shear of the velocity field (Hahn et al., 2007; Hoffman et al., 2012).

From the qualitative point of view, several elaborate theories have been proposed. The cosmic web nature is intimately connected with the gravitational formation process. In the standard model of hierarchical structure formation, the cosmic structure has emerged from the growth of small initial density fluctuations in the homogeneous early Universe (Peebles, 1980; Davis et al., 1985; White & Frenk, 1991). The accretion process involves the matter flowing out of the voids, collapsing into sheets and filaments, and merging into massive clusters. Thus, galaxy clusters are located at the intersection of filaments and sheets, which operate as channels for the matter to flow into them (van Haarlem & van de Weygaert, 1993; Colberg et al., 1999). The innermost part of clusters tends to eventually reach the virial equilibrium.

As result of this gravitational collapse, clusters of galaxies are the most recent structures in the Universe. For this reason, they are possibly the most easy large-scale systems to study. Mass measurement of galaxy clusters is of great interest for understanding the large-scale physical processes and the evolution of structures in the Universe (White et al., 2010). Moreover, the abundance of galaxy clusters as function of their mass is crucial for constraining cosmological models: the cluster mass function is an important tool for the determination of the amount of dark matter in the Universe and for studying the nature and evolution of dark energy (Haiman et al., 2001; Cunha et al., 2009; Allen et al., 2011). The oldest method for the cluster mass determination is based on the application of the virial theorem to positions and velocities of the cluster members (Zwicky, 1933). This method suffers from the main limitation that the estimated mass is significantly biased when the cluster is far from virialization. More recent and sophisticated techniques also rely strongly on the assumption of hydrostatic or dynamical equilibrium. The cluster mass profile can be estimated, for example, from observations of density and temperature of the hot X-ray gas, through the application of the hydrostatic equilibrium

equation (Ettori et al., 2002b; Borgani et al., 2004; Zappacosta et al., 2006; Schmidt & Allen, 2007; Host & Hansen, 2011). Another approach is based on the dynamical analysis of cluster-member galaxies and involves the application of the Jeans equations for steady-state spherical system (Girardi et al., 1998; Łokas & Mamon, 2003; Łokas et al., 2006; Mamon & Boué, 2010). Additional cluster mass estimators have been proposed, which are independent of the cluster dynamical state. A measurement of the total cluster mass can be achieved by studying the distortion of background galaxies due to gravitational lensing (Mandelbaum et al., 2010; Lombriser, 2011). The lensing technique is very sensitive to the instrument resolution and the projection effects. The caustic method has been proposed by Diaferio (1999). This method requires very large galaxy surveys, in order to determine the caustic curve accurately. Therefore, the development of new techniques and the combination of different independent methods, is extremely useful for providing a more accurate cluster mass measurement.

The Coma cluster of galaxies (Abell 1656) is one of the most extensively studied system of galaxies (Biviano, 1998), as the most regular, richest and best-observed in our neighborhood. The X-ray observations have provided several mass estimates (Hughes, 1989; Watt et al., 1992), obtained by assuming hydrostatic equilibrium. Dynamical mass measurements with different methods, based on the assumption of dynamical equilibrium, are reported in (The & White, 1986; Łokas & Mamon, 2003). Geller et al. (1999) perform a dynamical measurement of the Coma cluster, using the caustic method, and weak lensing mass estimates of Coma have been carried on by Kubo et al. (2007) and Gavazzi et al. (2009).

In the present paper we propose a new method for estimating the mass of clusters. We intend to infer total cluster mass from the knowledge of the kinematics in the outskirts, where the matter has not yet reached equilibrium. The key of our method is the analysis of filamentary and sheetlike structures flowing outside the cluster. We apply our method for the total virial mass estimate to the Coma cluster, and we compare our result with some of the previous ones in the literature. Our method also provides an estimation of the orientation of the structures we find, in the three dimensional space. This can be useful to identify a major merging plane, if a sufficient number of structures are detected and at least three of them are on the same plane.

The paper is organized as follows. In section 2 we derive the relation between the velocity profile of galaxies in the outer region of clusters and the virial cluster mass. In section 3 we propose a method to detect filaments or sheets by looking at the observed velocity field. In section 4 we test the method to a cosmological simulated cluster-size halo and we present the result on the mass measurement. In section 5 we present the structures we find around the Coma cluster and the Coma virial mass determination.

3.2.1 MASS ESTIMATE FROM THE RADIAL VELOCITY PROFILE

Galaxy clusters are characterized by a virialized region where the matter is approximately in dynamical equilibrium. The radius that delimitates the equilibrated cluster, i.e. the virial radius r_v , is defined as the distance from the centre of the cluster within which the mean density is Δ times the critical density of the Universe ρ_c . The virial mass is then given by

$$M_v = \frac{4}{3}\pi r_v^3 \Delta \rho_c. \quad (3.1)$$

The critical density is given by

$$\rho_c = \frac{3H^2}{8\pi G}, \quad (3.2)$$

where H is the Hubble constant and G the universal gravitational constant.

The circular velocity V_v at $r = r_v$, i.e. the virial velocity, is defined as

$$V_v^2 = \frac{G M_v}{r_v}. \quad (3.3)$$

The immediate environments of galaxy clusters outside the virial radius are characterized by galaxies and groups of galaxies which are falling towards the cluster centre. These galaxies are not part of the virialized cluster, but they are gravitationally bound to it. The region where the infall motion is most pronounced extends up to three or four times the virial radius (Mamon et al., 2004; Wojtak et al., 2005; Rines & Diaferio, 2006; Cuesta et al., 2008; Falco et al., 2013b). At larger scales, typically beyond $6 - 10 r_v$, the radial motion of galaxies with respect to the cluster centre, is essentially dominated by the Hubble flow. In the transition region between the infall regime and the Hubble regime, the galaxies are flowing away from the cluster, but they are still gravitationally affected by the presence of its mass. At this scale, the gravitational effect of the inner cluster mass is to perturb the simple Hubble motion, leading to a deceleration.

The total mean radial velocity of galaxies outside clusters is therefore the combination of two terms:

$$\bar{v}_r(r) = H r + \bar{v}_p(r), \quad (3.4)$$

the pure Hubble flow, and a mean negative infall term $\bar{v}_p(r)$, that accounts for the departure from the Hubble relation. Section (3.2.2) is dedicated to the characterization of the function $\bar{v}_p(r)$.

The mean infall velocity depends on the halo mass, being more significant for larger mass haloes. Therefore, we can rewrite equation (5.21) as

$$\bar{v}_r(r, M_v) = H r + \bar{v}_p(r, M_v), \quad (3.5)$$

where we include the dependence on the virial mass M_v .

Therefore, once we know the relation between \bar{v}_p and M_v , equation (3.5) can be used to infer the virial mass of clusters.

In the next section, we will derive the equation that connects the peculiar velocity of galaxies \bar{v}_p with the virial mass of the cluster M_v .

3.2.2 RADIAL INFALL VELOCITY PROFILE

Simulations have shown a quite universal trend for the radial mean velocity profile of cluster-size haloes, when normalized to their virial velocities (Prada et al., 2006; Cuesta et al., 2008). This feature can be seen, for example, in Fig. 3.1, where the median radial velocity profile for three samples of stacked simulated haloes is displayed. The units in the plot are the virial velocity V_v and virial radius r_v . The virial masses for the samples are: $M_v = 0.8 \times 10^{14} M_\odot$ (blue, triple-dot dashed line), $M_v = 1.1 \times 10^{14} M_\odot$ (green dot dashed line), $M_v = 4.7 \times 10^{14} M_\odot$ (red dashed line). The cosmological N-body simulation we used is described in section 3.4.

In order to derive an approximation for the mean velocity profile, the spherical collapse model has been assumed in several works (Peirani & de Freitas Pacheco, 2006, 2008; Karachentsev & Nasonova (Kashibadze), 2010; Nasonova et al., 2011). Here we make a more conservative choice. We parametrize the infall profile using only the information that it must reach zero at large distances from the halo centre, and then we fit the universal shape of the simulated haloes profiles. Therefore, we don't assume the spherical infall model.

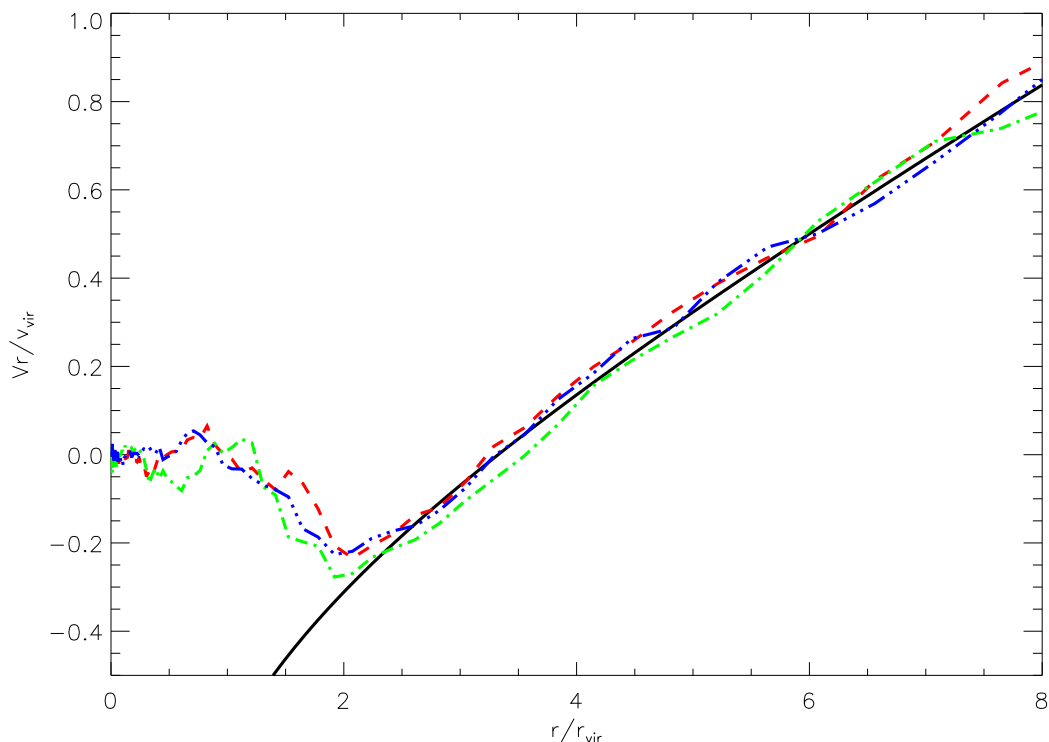


Figure 3.1 Median radial velocity profile for three samples of stacked simulated halos. The virial masses for the samples are: $M_v = 0.8 \times 10^{14} M_\odot$ (blue, triple-dot dashed line), $M_v = 1.1 \times 10^{14} M_\odot$ (green dot dashed line), $M_v = 4.7 \times 10^{14} M_\odot$ (red dashed line). The black solid line is our simultaneous fit to the three profiles.

In the region where the Hubble flow starts to dominate and the total mean radial velocity becomes positive, a good approximation for the infall term is

$$\bar{v}_p(r) \approx -v_0 \left(\frac{r}{r_v} \right)^{-b}, \quad (3.6)$$

with $v_0 = a V_v$, where V_v is the virial velocity, and r_v is the virial radius.

We fit equation (3.6) to the three profiles in Fig. 3.1 simultaneously, with a and b as free parameters. The fit is performed in the range $r = 3 - 8 r_v$. The best fit is the black solid line, corresponding to parameters: $a = 0.8$ and $b = 0.42$.

This allows to fix a universal shape for the mean velocity of the infalling matter, as function of the virial velocity, i.e. the virial mass, in the outer region of clusters.

3.3 FILAMENTS AND SHEETS AROUND GALAXY CLUSTERS

The method we propose for measuring the virial cluster mass, consists in using only observed velocities and distances of galaxies, which are outside the virialized part of the cluster, but whose motion is still affected by the mass of the cluster. Given the dependence of the infall velocity on the virial mass, we wish to estimate M_v by fitting the measured velocity of galaxies

moving around the cluster with equations (3.5) and (3.6).

To this end, we need to select galaxies which are sitting, on average, in the transition region of the mean radial velocity profile. For the fit to be accurate, the galaxies should be spread over several megaparsec in radius.

Observations give the two-dimensional map of clusters and their surroundings, namely the projected radius of galaxies on the sky R , and the component of the galaxy velocities along the line of sight v_{los} . The reconstruction of the radial velocity profile would require the knowledge of the radial position of the galaxies, i.e. the radius r . The velocity profile that we infer from observations is also affected by the projection effects. If the galaxies were randomly located around clusters, the projected velocities would be quite uniformly distributed, and we would not see any signature of the radial velocity profile. The problem is overcome because of the strong anisotropy of the matter distribution. At several megaparsec away from the cluster centre, we will select collections of galaxies bound into systems, as filaments or sheets. The presence of such objects can break the spatial degeneracy in the velocity space.

In sections (3.3.1) and (3.3.2), we explain in details how such objects can be identified as filamentary structures in the projected velocity space.

3.3.1 LINE OF SIGHT VELOCITY PROFILE

In order to apply the universal velocity profile (3.6) to observations, we need to transform the 3D radial equation (5.21) in a 2D projected equation. We thus need to compute the line of sight velocity profile v_{los} as function of the projected radius R .

Let's consider a filamentary structure forming an angle α between the 3-dimensional radial position of galaxy members r and the 2-dimensional projected radius R . Alternatively, let's consider a sheet in the 3D space lying on a plan with inclination α with respect to the plan of the sky (see the schematic Fig. 3.2).

The transformations between quantities in the physical space and in the redshift space are

$$R = \cos \alpha r \quad (3.7)$$

for the spatial coordinate, and

$$v_{\text{los}}(R) = \sin \alpha v_r(r) \quad (3.8)$$

for the velocity.

By inserting equation (3.5) in equation (3.8), we obtain the following expression for the line of sight velocity in the general case:

$$v_{\text{los}}(R, \alpha, M_v) = \sin \alpha \left[H \frac{R}{\cos \alpha} + v_p \left(\frac{R}{\cos \alpha}, M_v \right) \right]. \quad (3.9)$$

If we use our model for the infall term, given by equation (3.6), the line of sight velocity profile in equation (3.9) becomes

$$v_{\text{los}}(R, \alpha, M_v) = \sin \alpha \left[H \frac{R}{\cos \alpha} - a V_v \left(\frac{R}{\cos \alpha r_v} \right)^{-b} \right]. \quad (3.10)$$

By using equation (3.10), it is, in principle, possible to measure both the virial cluster mass M_v and the orientation angle α of the structure. In fact, if we select a sample of galaxies which

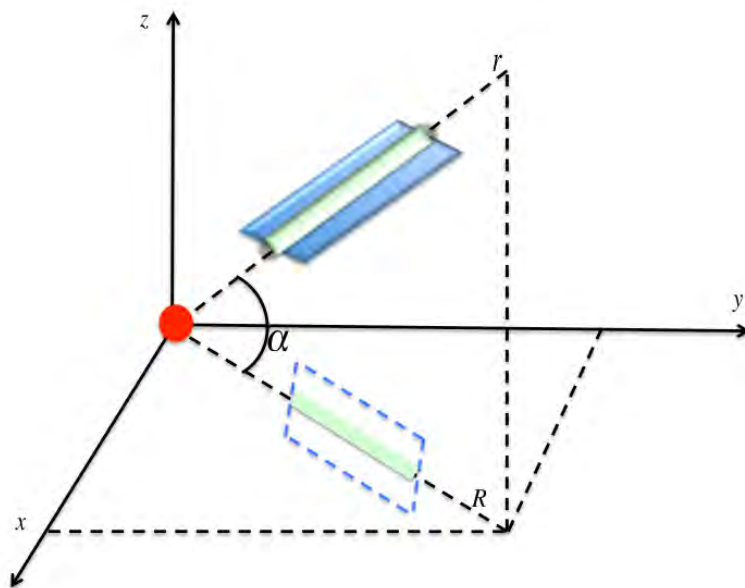


Figure 3.2 Schematic drawing of a filament or a sheet in 3D with inclination α between the radial distance r and the projected radius R . The cluster is represented by the red circle in the centre of the frame. The z -axis corresponds to the observer line of sight.

lie in a sheet or a filament, we can fit their phase-space coordinates (R, v_{los}) with equation (3.10), where only two free parameters (α, M_v) are involved. The identification of structures and the accuracy on the mass estimate require a quite dense sample of galaxies observed outside the cluster.

3.3.2 LINEAR STRUCTURES IN THE VELOCITY FIELD

Our interest here is thus in finding groups of galaxies outside clusters, that form a bound system with a relatively small dispersion in velocity, and that lie on a preferential direction in the 3D space. In particular, we are interested in such objects when they are far enough from the cluster, to follow a nearly linear radial pattern in the velocity space, corresponding to a decelerated Hubble flow.

We expect these objects to form filament-like structures in the projected velocity space. In fact, if we apply the formula in equation (3.9) to galaxies with the same orientation angle α within a small scatter, the radial velocity shape given by equation (3.5) is preserved. Thus, these galaxies can be identified as they are collected on a line in the observed velocity space.

Nevertheless, we can look at the structure in the 2D map (the (x, y) plane in Fig. 3.2). If all the selected galaxies lie on a line, within a small scatter, also in the (x, y) plane, they can be defined as a filament. If they are confined in a region within a small angular aperture, they might form a sheet (see the Fig. 3.2). Complementary papers will analyze properties of such sheets (Brinckmann et al., 2013; Sparre, 2013; Wadekar & Hansen, 2013).

We want to point out here that Fig. 3.2 describes the ideal configuration for filaments and sheets to have a quasi-linear shape in the observed velocity plane. Therefore, not all the filaments and sheets will satisfy this requirement, i. e. not all the structures outside clusters can be

detected by looking at the velocity field.

Our method for identifying these objects is optimized towards structures which are narrow in velocity space, while still containing many galaxies, and therefore which are closer to face-on than edge-on. It consists in selecting a region in the sky, and looking for a possible presence of an overdensity in the corresponding velocity space. We will describe the method in details in the next section.

3.4 TESTING THE METHOD ON COSMOLOGICAL SIMULATION

As a first test of our method, we apply it to a cluster-size halo from a cosmological N-body simulation of pure dark matter (DM).m

The N-body simulation is based on the *WMAP3* cosmology. The cosmological parameters are $\Omega_M = 0.24$ and $\Omega_\Lambda = 0.76$, and the reduced Hubble parameter is $h = 0.73$. The particles are confined in a box of size $160 h^{-1}$ Mpc. The particle mass is $3.5 \times 10^8 M_\odot$, thus there are 1024^3 particles in the box. The evolution is followed from the initial redshift $z = 30$, using the MPI version of the ART code (Kravtsov et al., 1997; Gottloeber & Klypin, 2008). The algorithm used to identify clusters is the hierarchical friends-of-friends (FOF) with a linking length of 0.17 times the mean interparticle distance. The cluster centres correspond to the positions of the most massive substructures found at the linking length eight times shorter than the mean interparticle distance. We define the virial radius of halos as the radius containing an overdensity of $\Delta = 93.8$ relative to the critical density of the Universe. More details on the simulation can be found in (Wojtak et al., 2008).

For our study, we select, at redshift $z = 0$, a halo of virial quantities $M_v = 4.75 \times 10^{14} M_\odot$, $r_v = 2.0$ Mpc and $V_v = 1007.3$ km/s.

We treat the DM particles in the halo as galaxies from observations. The first step is to project the 3D halo as we would see it on the sky. We consider three directions as possible lines of sight. For each projection, we include in our analysis all galaxies in the box $x = [-20, 20]$ Mpc and $y = [-20, 20]$ Mpc, where x, y are the two directions perpendicular to the line of sight.

The method described in the next section is applied to all the three projections.

3.4.1 IDENTIFICATION OF FILAMENTS AND SHEETS FROM THE VELOCITY FIELD

Our goal is to find structures confined in a relatively small area in the (x, y) plane. To this end, we split the spatial distribution into eight two-dimensional wedges (for example in Figure 3.3 the orange points represent one of the wedges) and we look at each of them in the (R, v_{los}) -space (for example in Fig. 3.4 we look at the orange wedge in Fig. 3.3, in the velocity space), where we aim to look for overdensities.

We confine the velocity field to the box: $v_{\text{los}} = [-4000, 4000]$ km/s and $R = [4, 20]$ Mpc, and we divide the box into 50 cells, 4 Mpc large and 400 km/s high.

For each of the selected wedges, we want to compare the galaxy number density n_i in each cell i , with the same quantity calculated for the the rest of the wedges in the same cell. More precisely, in each cell, we calculate the mean of the galaxy number density of all the wedges but the selected one. This quantity acts as background for the selected wedge, and we refer to it as n_i^{bg} .

In Fig. 3.3, the wedge under analysis is represented by the orange points, and the background by the green points. We exclude from the background the two wedges adjacent to the

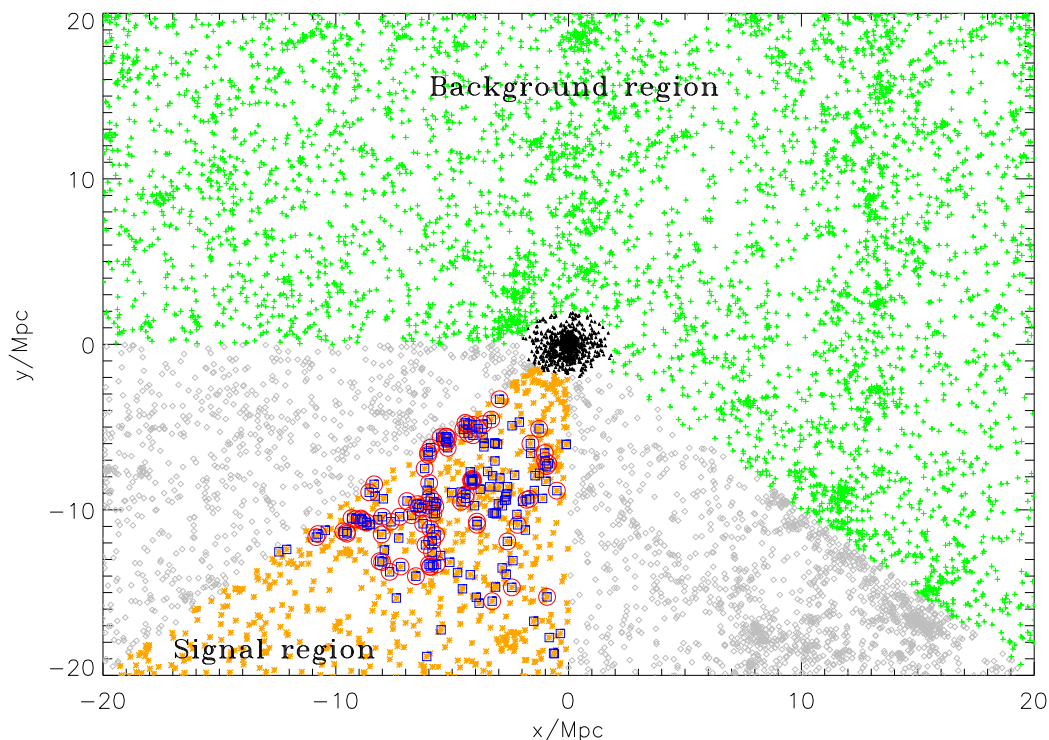


Figure 3.3 Two-dimensional projection of the simulation box, centered on the selected simulated halo. The black triangles represent the particles inside the virial radius of the halo. The orange points belong to one of the eight wedges we select in the (x, y) plane. The background for the selected wedge is given by the green crosses. The two wedges adjacent to the selected wedge, gray diamonds, are excluded from the analysis. In the selected wedge, we identify a sheet that is represented by the red circles. The blue squares correspond to the total overdensity we find in the wedge, with the method described in the text.

selected one (gray points in Fig. 3.3). We need this step because, if any structure is sitting in the selected wedge, it might stretch to the closest wedges.

The overdensity in the cell i is evaluated as

$$m_i = \frac{n_i - n_i^{bg}}{n_i^{bg}}, \quad (3.11)$$

and we calculate the probability density $p(m_i)$ for the given wedge. We take only the cells in the top 1σ region of the probability density distribution, i.e. where the integrated probability is above $(100 - 16.8)\%$, in order to reduce the background noise. Among the galaxies belonging to the selected cells, we take the ones lying on inclined lines within a small scatter, while we remove the unwanted few groups which appear as blobs or as horizontal strips in the (R, v_{los}) -space. We apply this selection criterion because we are interested in extended structures which have a coherent flow relative to the cluster.

This method leaves us with only one structure inside the wedge in Fig. 3.3 (red points). It is a sheet, as it appears as a two-dimensional object on the sky, opposed to a filament which

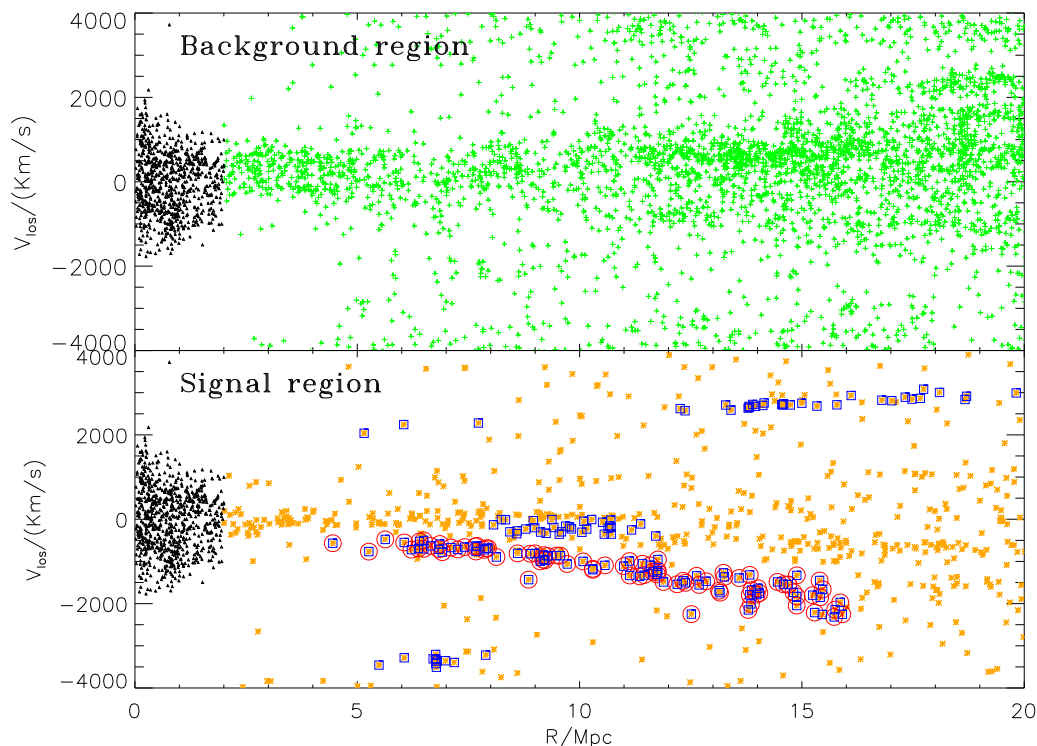


Figure 3.4 Line of sight velocity v_{los} as function of the projected distance R from the centre of the simulated halo. *Upper panel:* The background in the analysis is represented by the green crosses. The black triangles are all the particles within the virial radius. *Bottom panel:* The orange points represent our signal, i.e. the selected wedge. The blue points correspond to the overdensity in the wedge. The only almost straight inclined line is shown in red circles. We identify this filamentary-like structure as a sheet.

should appear one-dimensional. We see such sheet only in one of the three projections we analyse. The bottom panel of Fig. 3.4 shows the velocity-distance plot corresponding to all the galaxies belonging to the selected wedge (orange points), while the selected strips of galaxies are shown as blue points. The desired sheet (red points) is an almost straight inclined line crossing zero velocity roughly near 5-10 Mpc and contains 88 particles. The background wedges are displayed in the upper panel of Fig. 3.4.

3.4.2 ANALYSIS AND RESULT

Having identified one sheet around the simulated halo, we can now extract the halo mass, using the standard Monte Carlo fitting methods. We apply the Monte Carlo Markov chain to the galaxies belonging to the sheet. The model is given by equation (3.10), where the free parameters are (α, M_{vir}) . We set $\Delta = 93.8$ and $H = 73 \text{ km}/(\text{s Mpc})$, as these are the values set in the cosmological simulation. We run one chain of 5000 combinations of parameters and then we remove the burn-in points.

In Fig. 3.5 we show the scatter plot on the plane of the two parameters, and the one-dimensional

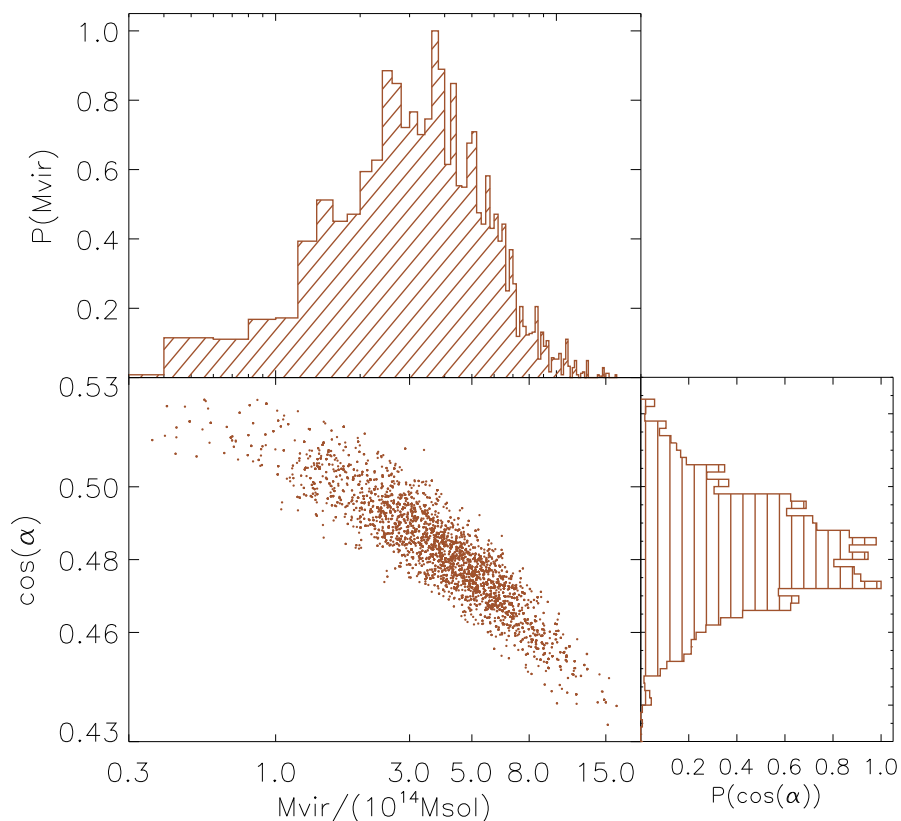


Figure 3.5 Result of the Monte Carlo Markov chain applied to the sheet found outside the simulated halo. *Central panel*: Scatter plot of the two free parameters ($\cos(\alpha)$, M_{vir}) obtained by the MCMC chain. *Upper panel*: Probability density function of the virial mass. *Left panel*: Probability density function of the viewing angle. The initial number of points is 5000 and we remove the points of burn-in. The mean value for the virial mass and the cosine of the angle are $M_{\text{vir}} = (4.3 \pm 2.2) \times 10^{14} M_{\odot}$ and $\cos(\alpha) = 0.48 \pm 0.02$, which are comparable to the true halo virial mass $M_{\text{vir}} = 4.75 \times 10^{14} M_{\odot}$ and angle $\cos(\alpha) = 0.5$.

probability distribution functions of the virial mass and the orientation angle. The mean value for the virial mass is $M_{\text{vir}} = (4.3 \pm 2.2) \times 10^{14} M_{\odot}$, which is comparable to the true halo virial mass $M_{\text{vir}} = 4.75 \times 10^{14} M_{\odot}$. The mean value for the cosine of the angle between R and r is $\cos(\alpha) = 0.48 \pm 0.02$, corresponding to $\alpha = -1.07 \pm 0.02$ rad. In Fig. 3.6 we show the sheet in the 3D space (blue points). The best fit for the plane where the sheet is laying, is shown as the green plane, and the corresponding angle is $\alpha = -1.05$ rad, giving $\cos(\alpha) = 0.5$. Our estimation is thus consistent, within the statistical error, with the true orientation of the sheet in 3D.

Although our method provides the correct halo mass and orientation angle within the errors, the results slightly underestimate the true values, for both parameters. Systematic errors on the mass and angle estimation might be due to the non ideal shape of the structures. The sheet we find has finite thickness, and it is not perfectly straight in the 3D space. The closer the detected structure is to an ideal infinite thin and perfectly straight object, the smaller the

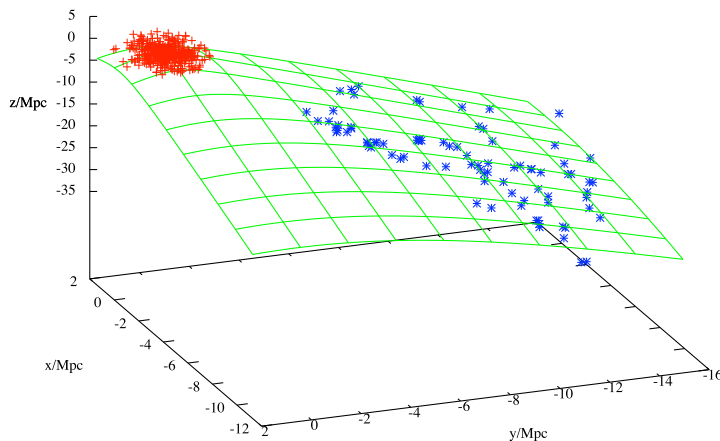


Figure 3.6 The sheet we found outside the simulated halo in the three-dimensional space. The z -axis corresponds to the line of sight direction. The blue points represent the particles belonging to the sheet, and the green plane is the best fit for the sheet's plane, corresponding to $\alpha = -1.05$ ($\cos(\alpha) = 0.5$) rad. The red points represent the particles within the virial radius of the halo.

errors would be. Another problem might reside in the assumption of spherical symmetry. The median radial velocity profile of a stack of haloes, might slightly differ from the real velocity profile of each individual halo. Intrinsic scatter of the simulated infall velocity profiles leads to additional systematic errors on the determination of the best fitting parameters. Our estimate of this inaccuracy yields 50% for the virial mass and 2.5% for the angle.

The presence of this systematic is confirmed by Fig. 3.7. The bottom panel represents our result of the sheet analysis, when using a fit to the real mean radial velocity of the halo, which is shown in the upper panel. The best fit parameters to the radial velocity profile of the halo, with equation (3.6), are $a = 1.5$ and $b = 0.89$. In Fig. 3.7, the black solid line is the fit to the halo velocity profile (red dashed line) and the green dot-dashed line is the universal velocity profile used in the previous analysis. The two profiles overlap in the range $\approx 3 - 5 r_v$, but they slightly differ for larger distances, where our sheet is actually sitting. Replacing the universal radial velocity profile with the true one, eliminates the small off set caused by the departure of the two profiles. In the new analysis, the mean value for the virial mass is $M_{\text{vir}} = (4.67 \pm 1.9) \times 10^{14} M_{\odot}$, while the mean value for the cosine of the angle between R and r is $\cos(\alpha) = 0.5 \pm 0.01$. They are in very good agreement with the true values of the parameters $M_{\text{vir}} = 4.7 \times 10^{14} M_{\odot}$ and $\cos(\alpha) = 0.5$.

3.5 RESULT ON COMA CLUSTER

In this section, we will apply our method to real data of the Coma cluster.

We search for data in and around the Coma Cluster in the SDSS database (Abazajian et al.,

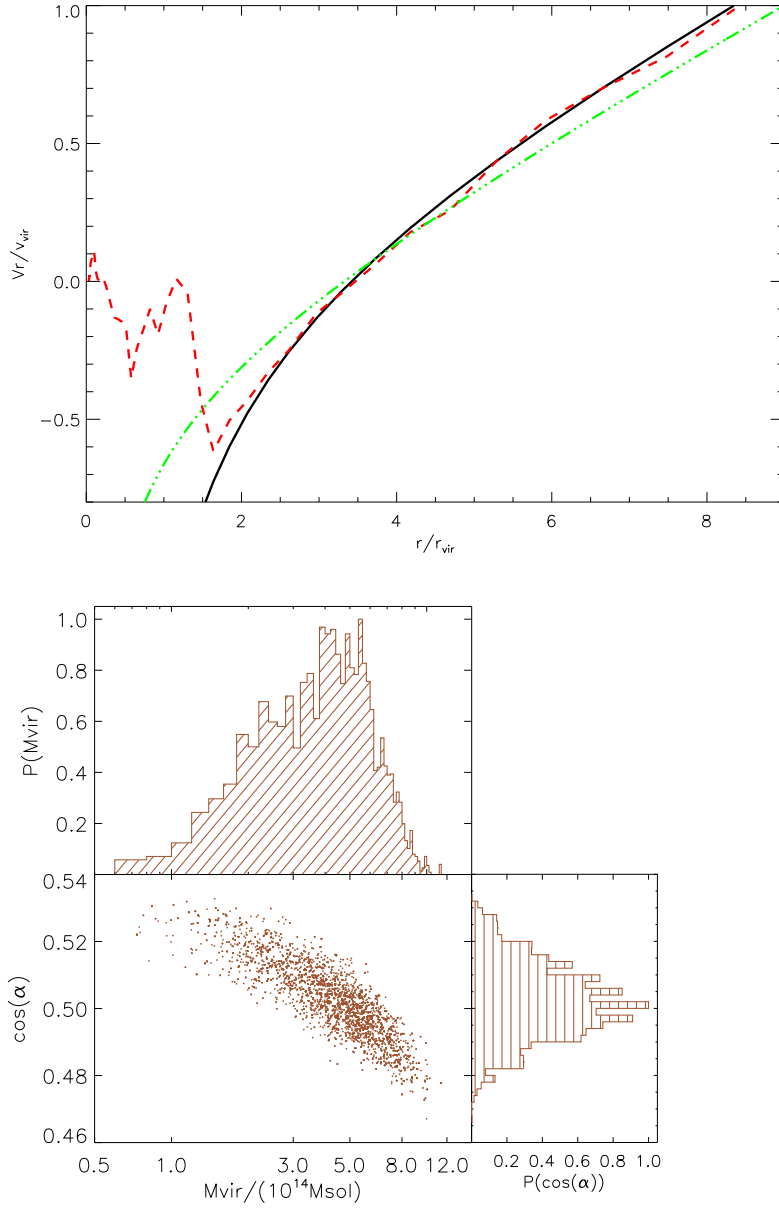


Figure 3.7 The top figure shows the median radial velocity profile for the simulated halo (red dashed line). The black solid line is our fit to the profile. The green dot-dashed line is the universal radial profile showed in Fig. 3.1. The bottom figure shows the result of the Monte Carlo Markov chain applied on the sheet found around the simulated halo, using the fit to the mean velocity profile of the halo (top figure). *Central panel:* Scatter plot of the two free parameters ($\cos(\alpha)$, M_{vir}) obtained by the MCMC chain. *Upper panel:* Probability density function of the virial mass. *Left panel:* Probability density function of the viewing angle. The initial number of points is 5000 and we remove the points of burn-in. The mean value for the virial mass is $M_{vir} = (4.67 \pm 1.9) \times 10^{14} M_{\odot}$, which is very close to the true halo virial mass $M_{vir} = 4.75 \times 10^{14} M_{\odot}$. The mean value for the cosine of the angle is $\cos(\alpha) = 0.5 \pm 0.01$, in agreement with the real value $\cos(\alpha) = 0.5$.

2009). We take the galaxy NGC 4874 as the centre of the Coma cluster (Kent & Gunn, 1982), which has coordinates: RA=12h59m35.7s, Dec=+27deg57'33". We select galaxies within 18 degrees from the position of the Coma centre and with velocities between 3000 and 11000 km/s. The sample contains 9000 galaxies.

We apply the method for the identification of structures outside clusters to the Coma data. We detect two galactic sheets in the environment of Coma. We denote our sheets as *sheet 1* and *sheet 2*.

Fig. 3.8 shows the Coma cluster and its environment up to 18 degrees from the cluster centre. The number of galaxies with spectroscopically measured redshifts within 2.5 Mpc, which is roughly the virial radius of Coma, is 748. These galaxies are indicated as black triangles. The sheets are the red circles. The upper panel refers to the *sheet 1*, which contains 51 galaxies. The bottom panel refers to the *sheet 2*, which is more extended and contains 228 galaxies. In Fig. 3.9, we show the sheets in the velocity space. They both appear as inclined straight lines. The *sheet 1* goes from ≈ 7 Mpc to ≈ 14 Mpc. As the velocities are negative, the sheet is between us and Coma. The *sheet 2* goes from ≈ 11 Mpc to ≈ 22 Mpc. As the velocities are positive, the sheet is beyond Coma.

As we did for the cosmological simulation, we have removed the collections of galaxies which are horizontal groups in (R, v_{los}) -space by hand. For example, in the case of the *sheet 1* in the upper panel of Fig. 3.9, we define the sheet only by including the inclined pattern and therefore, by excluding the horizontal part of the strip.

We then fit the line of sight velocity profiles of the two sheets with equation (3.10). We set $\Delta = 93.8$ and $H = 73 \text{ km}/(\text{s Mpc})$, as for the cosmological simulation.

In Fig. 3.10 we show the scatter plot on the plane of the two parameters $(\cos(\alpha), M_{\text{vir}})$, and the one-dimensional probability distribution functions of the virial mass and the orientation angle, for both the sheets. The angle α can be very different for different sheets, as it only depends on the position of the structure in 3D. Instead, we expect the result on the cluster mass M_{vir} to be identical, as it refers to the same cluster.

In Fig. 3.11, we overplot the probability distributions for the virial mass of Coma, from the analysis of the two sheets. The two probability distributions are very similar. The mean value of the virial mass is $M_{\text{vir}} = (9.7 \pm 3.6) \times 10^{14} M_{\odot}$ for the *sheet 1* and $M_{\text{vir}} = (8.7 \pm 3.3) \times 10^{14} M_{\odot}$ for the *sheet 2*. When applying equation (3.1), these values give a virial radius of $r_{\text{vir}} = 2.5$ Mpc and $r_{\text{vir}} = 2.4$ Mpc, respectively. The best mass estimate based on the combination of these measurements is: $M_{\text{vir}} = (9.2 \pm 2.4) \times 10^{14} M_{\odot}$.

Our result is in good agreement with previous estimates of the Coma cluster mass. In Hughes (1989), they obtain a virial mass $M_{\text{vir}} = (13 \pm 2) \times 10^{14} M_{\odot}$ from their X-ray study. From the galaxy kinematic analysis, Łokas & Mamon (2003) report a virial mass $M_{100} = (15 \pm 4.5) \times 10^{14} M_{\odot}$, corresponding to a density contrast $\Delta = 100$, which is very close to our value. Geller et al. (1999) find a mass $M_{200} = 15 \times 10^{14} M_{\odot}$, corresponding to a density contrast $\Delta = 200$. The weak lensing mass estimate in Kubo et al. (2007) gives $M_{200} = 2.7^{+3.6}_{-1.9} \times 10^{15} M_{\odot}$.

The mean value for cosine of the orientation angle is $\cos(\alpha) = 0.36 \pm 0.01$, corresponding to $\alpha = -1.2 \pm 0.01$ rad, for the *sheet 1* and $\cos(\alpha) = 0.64 \pm 0.02$, corresponding to $\alpha = 0.87 \pm 0.02$ rad, for the *sheet 2*. These results are affected by a statistical error of 50% for the mass and 2.5% for the angle, as discussed in Section 3.4.2.

The value obtained for the orientation α of a sheet corresponds to the mean angle of all the galaxies belonging to the sheet. By knowing α , we can calculate the corresponding coordinate along the line of sight for all the galaxies, and therefore, we reconstruct the three dimensional map of the two structures, as shown in Fig. 3.12. The sheets we find are lying on two different

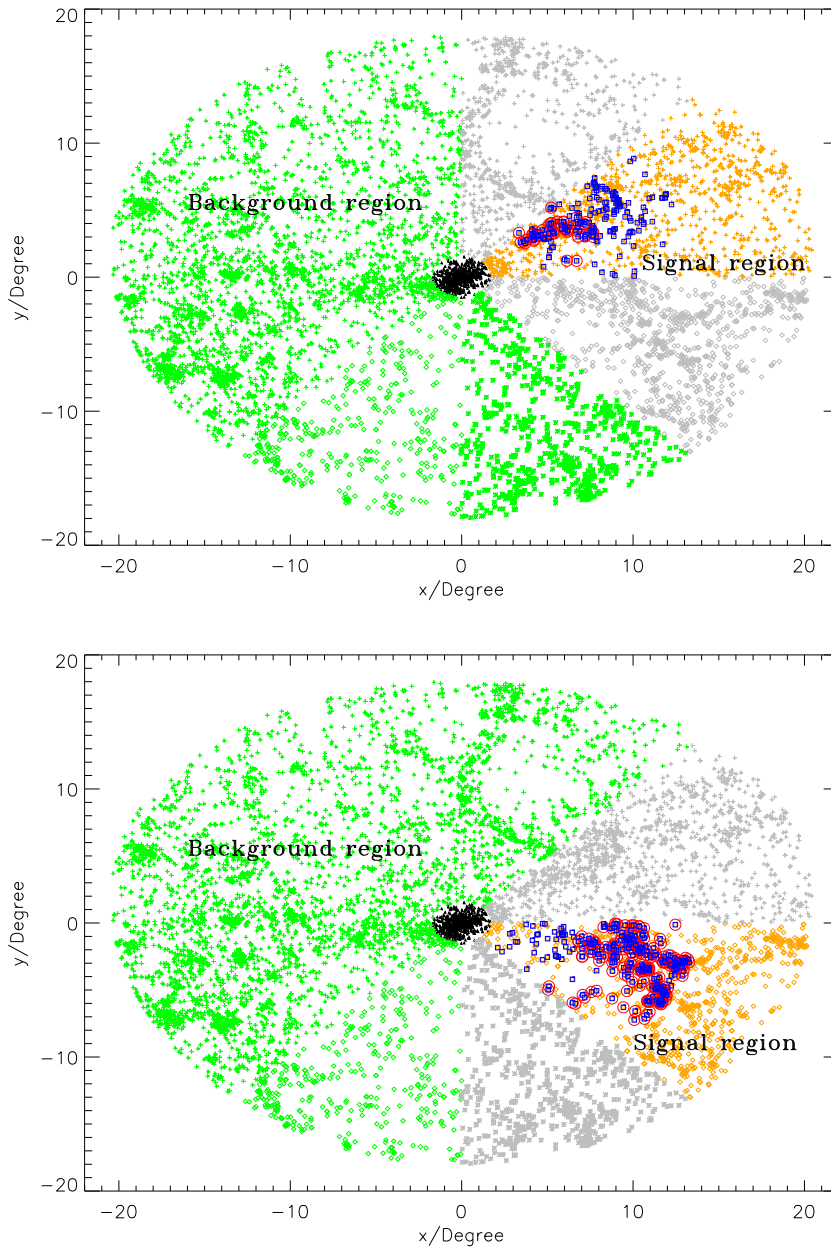


Figure 3.8 Sky map of the Coma cluster. The top figure shows the *sheet 1* and the bottom figure shows the *sheet 2*. The black triangles represent the particles inside the virial radius of Coma. The orange points belong to one of the eight wedges we select in the (x, y) plane. The background for the selected wedge is given by the green crosses. The two wedges adjacent to the selected wedge, gray diamonds, are excluded from the analysis. In the selected wedge, we identify a sheet that is represented by the red circles. The blue squares correspond to the total overdensity we find in the wedge, with the method described in the text.

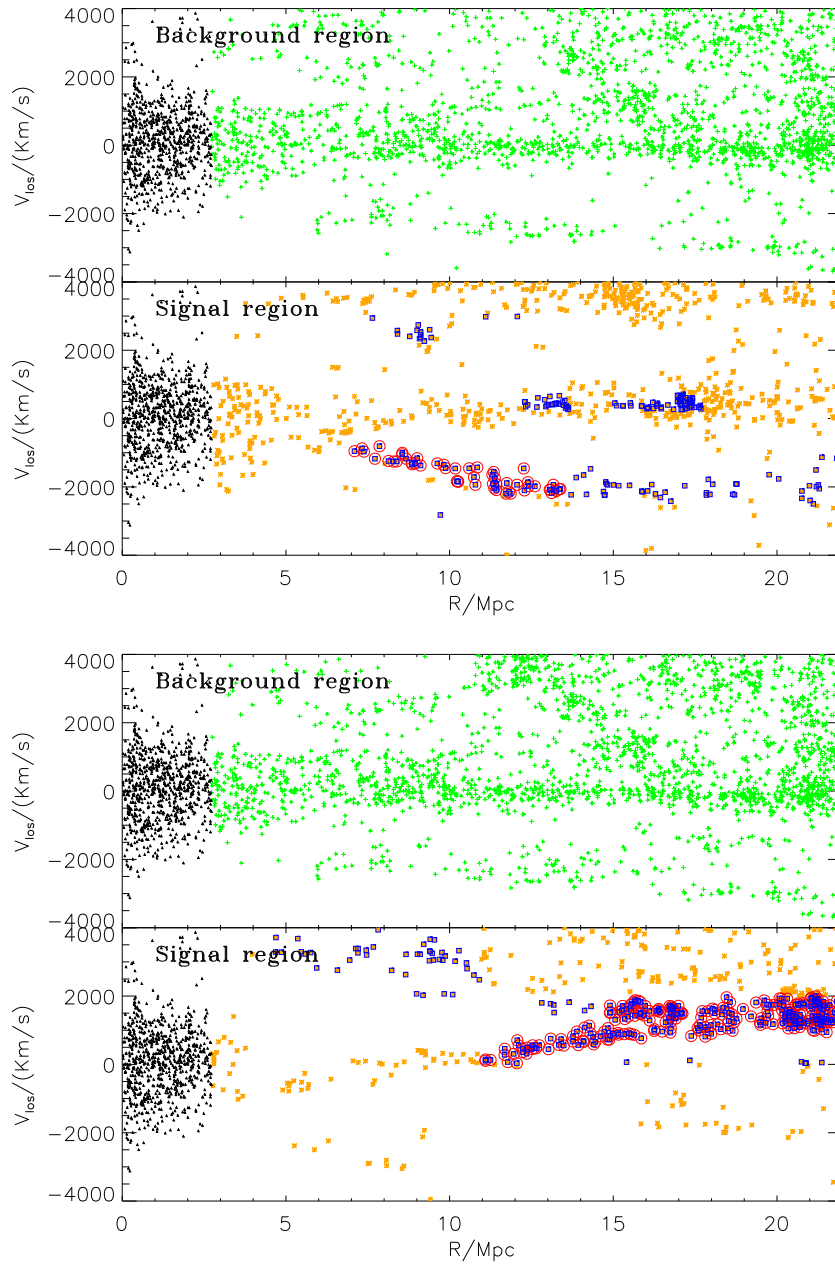


Figure 3.9 Line of sight velocity v_{los} as function of the projected distance R from the centre of Coma. The velocities are scaled by the velocity of Coma $v_{\text{Coma}} = 4000\text{km/s}$. The top figure shows the *sheet 1* and the bottom figure shows the *sheet 2*. *Upper panels*: The background in the analysis is represented by the green crosses. The black triangles are all the galaxies within $r = 2.5$ Mpc. *Bottom panel*: The orange points represent the signal, i.e. the selected wedge. The blue points correspond to the overdensity. The almost straight inclined lines are shown in red circles. We identify these filamentary-like structures as sheets.

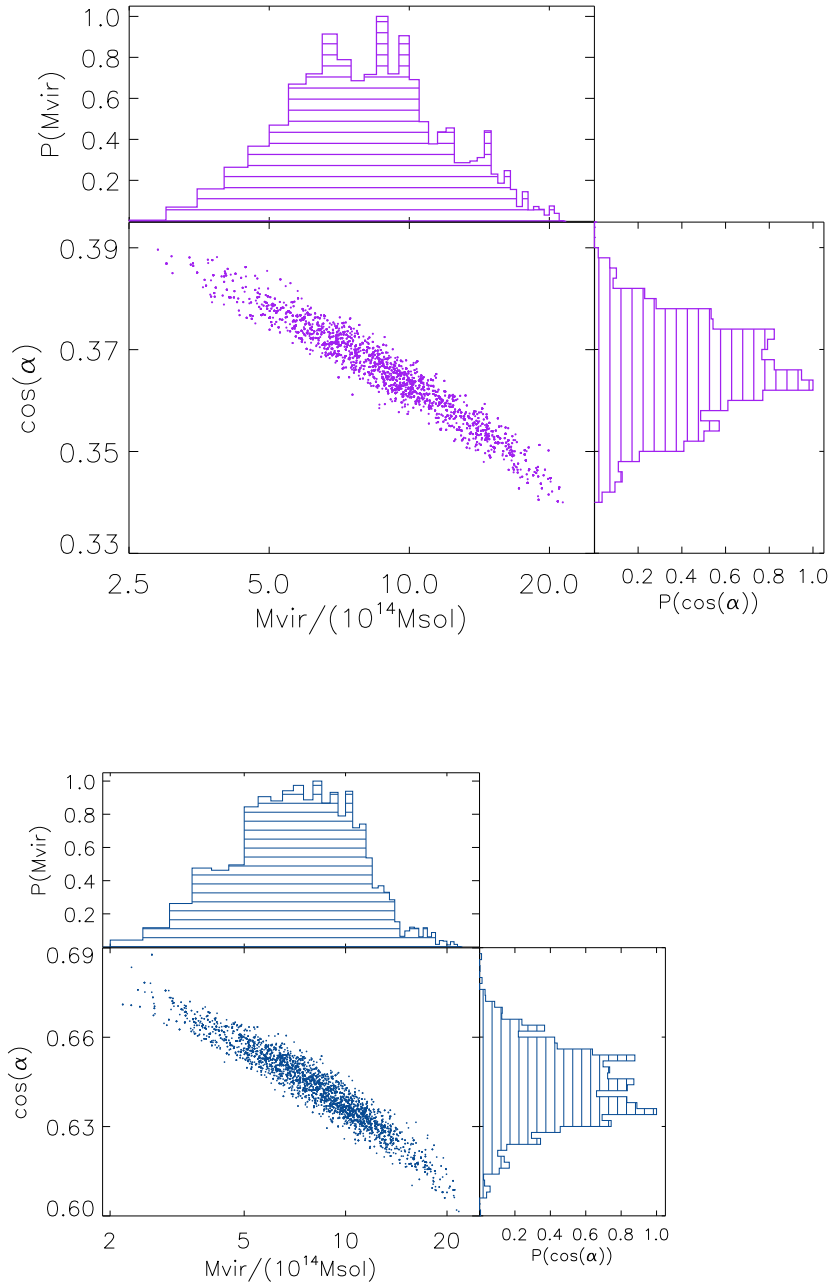


Figure 3.10 Result of the Monte Carlo Markov chain applied to the two sheets found outside the Coma cluster. The top figure refers to the *sheet 1* and the bottom figure refers to the *sheet 2*. *Central panels*: Scatter plot of the two free parameters ($\cos(\alpha)$, M_{vir}) obtained by the MCMC chain. *Upper panels*: Probability density function of the virial mass. *Right panels*: Probability density function of the viewing angle. The initial number of points is 5000 and we remove the points of burn-in.

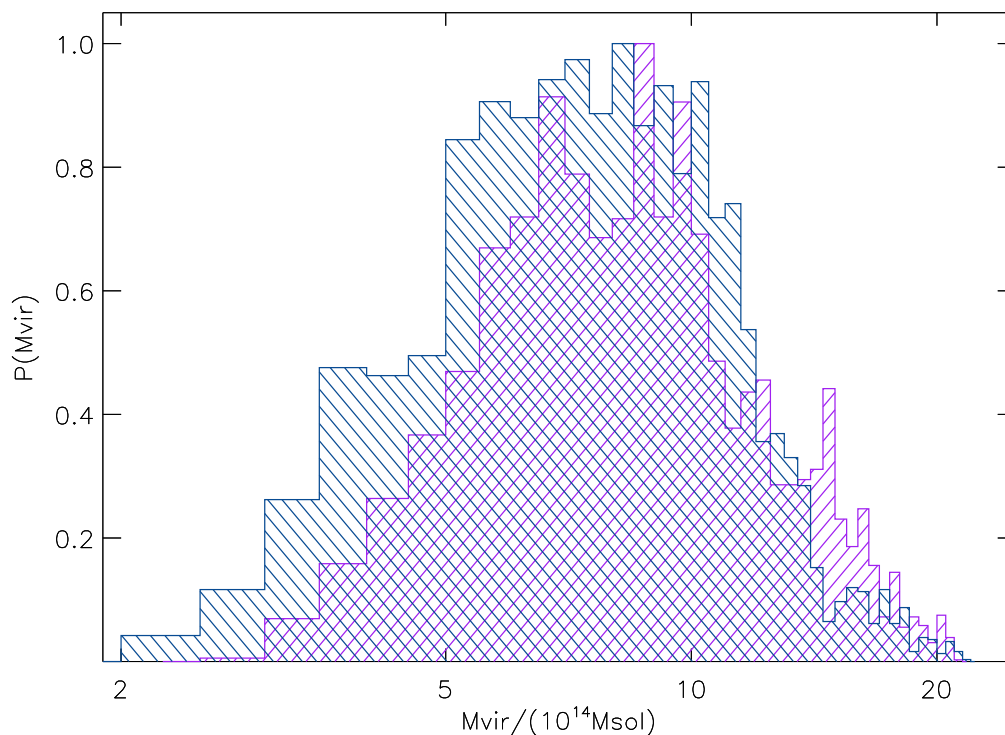


Figure 3.11 The probability density function of the Coma virial mass, derived through the sheet technique. The distribution coming from the *sheet 2* is the blue one, slightly to the left. The violet slightly narrower distribution corresponds to the *sheet 1*. The best mass estimate based on these measurement is: $M_{\text{vir}} = (9.2 \pm 2.4) \times 10^{14} M_{\odot}$.

planes.

3.6 SUMMARY AND CONCLUSION

The main purpose of this paper is to propose and test a new method for the mass estimation of clusters within the virial radius. The idea is to infer it only from the kinematical data of structures in the cluster outskirts.

In the hierarchical scenario of structure formation, galaxy clusters are located at the intersection of filaments and sheets. The motion of such non-virialized structures is thus affected by the presence of the nearest massive cluster.

We found that modeling the kinematic data of these objects leads to an estimation of the neighbor cluster mass. The gravitational effect of the cluster mass is to perturb the pure Hubble motion, leading to a deceleration. Therefore, the measured departure from the Hubble flow of those structures allows us to infer the virial mass of the cluster. We have developed a technique to detect the presence of structures outside galaxy clusters, by looking at the velocity space. We underline that the proposed technique doesn't aim to map all the objects around clusters, but it is limited to finding those structures that are suitable for the virial cluster mass estimation.

Our mass estimation method doesn't require the dynamical analysis of the virialized region of the cluster, therefore it is not based on the dynamical equilibrium hypothesis. However,

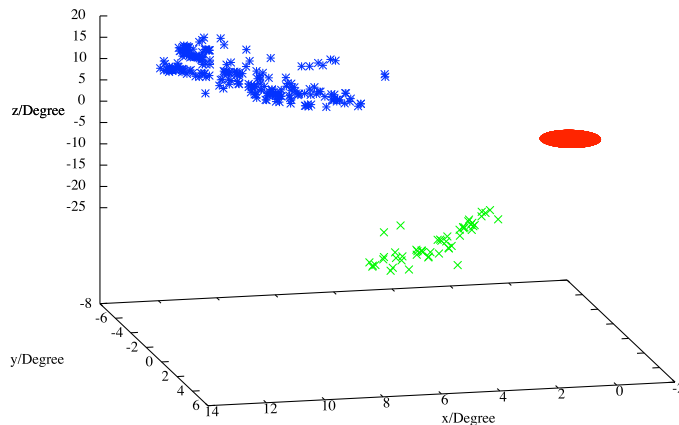


Figure 3.12 The sheets we found outside the Coma cluster in the three-dimensional space. The blue and the green points represent the particles belonging to the *sheet 1* and the *sheet 2*, respectively. The Coma cluster is indicated as a red sphere centered at $(x, y, z)=(0,0,0)$.

our method rely on the assumption of spherical symmetry of the system. In fact, we assume a radial velocity profile. Moreover, our method is biased by fixing the phenomenological fit to the radial infall velocity profile of simulation, as universal infall profile. From the practical point of view, this technique requires gathering galaxy positions and velocities in the outskirts of galaxy clusters, very far away from the cluster centre. A quite dense sample of redshifts is needed, in order to identify the possible presence of structures over the background. Once the structures are detected, the fit to their line of sight velocity profiles has to be performed. The fitting procedure involves only two free parameters: the virial mass of the cluster and the orientation angle of the structure in 3D. This makes the estimation of the virial cluster mass quite easy to obtain.

We have analysed cosmological simulations first, in order to test both the technique to identify structures outside clusters and the method to extract the cluster mass. We find one sheet outside the selected simulated halo, and we infer the correct halo mass and sheet orientation angle, within the errors.

We then applied our method to the Coma cluster. We have analysed the SDSS data of projected distances and velocities, up to 20 Mpc far from the Coma centre. Our work led to the detection of two galactic sheets in the environment of the Coma cluster. The estimation of the Coma cluster mass through the analysis of the two sheets, gives $M_{\text{vir}} = (9.2 \pm 2.4) \times 10^{14} M_{\odot}$. This value is in agreement with previous results from the standard methods. We note however that our method tends to underestimate the Coma virial mass, compared with previous measurements, which either assume equilibrium or sphericity.

In the near future, we aim to apply our technique to other surveys, where redshifts at very large distances from the clusters centre are available. If a large number of sheets and filaments

will be found, our method could also represent a tool to deproject the spatial distribution of galaxies outside galaxy clusters into the three-dimensional space.

The authors thank Stefan Gottloeber, who kindly agreed for one of the CLUES simulations (<http://www.clues-project.org/simulations.html>) to be used in the paper. The simulation has been performed at the Leibniz Rechenzentrum (LRZ), Munich. The Dark Cosmology Centre is funded by the Danish National Research Foundation.

4

MASS ESTIMATION IN THE OUTER REGION OF GALAXY CLUSTERS

Dynamical signatures of infall around galaxy clusters: a generalized Jeans equation

Martina Falco¹, Gary Mamon², Radoslaw Wojtak¹, Steen H. Hansen¹

Published in MNRAS, arXiv:1306.6637.

Abstract

We study the internal kinematics of galaxy clusters in the region beyond the sphere of virialization. Galaxies around a virialized cluster are infalling towards the cluster center with a non-zero mean radial velocity. We develop a new formalism for describing the dynamical state of clusters, by generalizing the standard Jeans formalism with the inclusion of the peculiar infall motions of galaxies and the Hubble expansion as well as the contributions due to background cosmology. Using empirical fits to the radial profiles of density, mean radial velocity and velocity anisotropy of both a stacked cluster-mass halo and two isolated halos of a cosmological dark matter only simulation, we verify that our generalized Jeans equation correctly predicts the radial velocity dispersion out to 4 virial radii. We find that the radial velocity dispersion inferred from the standard Jeans equation is accurate up to 2 virial radii, but overestimated by $\approx 20\%$ for the stacked halo and by $\approx 40\%$ for the isolated halos, in the range $\approx 2 - 3$ virial radii. Our model depends on the logarithmic growth rate of the virial radius (function of halo mass or concentration), which we estimate in 7 different ways, and on the departure from self-similarity of the evolution of the peculiar velocity profile in virial units.

4.1 SUMMARY

The standard Jeans analysis for the cluster mass estimation gives quite accurate results for the mass distribution within the virial radius. As the other traditional methods, it depends on the hypothesis that the cluster is in equilibrium. Therefore, the Jeans analysis cannot be applied beyond the fully virialized cluster zone. The only way to extend the same analysis to larger radii from the cluster center is to implement a correct description for the galaxy cluster dynamics, that includes the case of non-equilibrium configuration.

I have established a dynamical analysis that does not rely on the equilibrium assumption, by modifying the standard Jeans equation with the inclusion of extra terms, which are related to the non-equilibrium cluster dynamics and the underlying cosmology. Specifically, the changes made in the standard formalism can be summarized in the following effects, which we take into account:

- Effect due to the background mean density of the Universe.
- Effect due to the cosmological constant.
- Effect of the expansion of the Universe: Hubble velocity of galaxies around the cluster.
- Effect of the Peculiar infall velocity of galaxies around the cluster.

The first three are related to the cosmology, while the last one is a purely kinematical effect. The first two effects will affect the gravitational potential of the system, while the last two will change the dynamical side of the equation. We show that all the new terms due to the cosmology perfectly cancel each other (see chapter 5). The terms left are therefore only related to the peculiar motion of galaxies. Going a bit more in technical details, these extra terms have been obtained by making the same steps that lead from the Boltzmann equation to the Jeans equation, but dropping the assumption of steady-state system. This means that we compute and keep all the terms involving the radial infall \bar{v}_r and all the time derivatives. We still approximate the cluster to a spherically symmetric system.

With this work, we thus obtain a *generalized Jeans equation*, that in principle holds at all scales. I have tested the new formalism on cosmological simulations. Our model reproduces accurately the radial velocity dispersion profiles of cluster-size halos up to at least four times the virial radius.

All the details on the derivation of the generalized Jeans equation and the test on cosmological simulation are described in this chapter.

4.2 INTRODUCTION

Galaxy clusters are the largest gravitationally bound structures in the Universe. Cluster studies represent a particularly deep source of information in modern cosmology, since they provide constraints on the growth of structures in the universe and on cosmological parameters, in particular the dark energy equation of state parameter w , from the evolution of the cluster mass function (Haiman et al., 2001; Voit, 2005; Cunha et al., 2009). A crucial role is played by the accuracy to which we can determine the cluster mass. Therefore, the estimation of the cluster total mass has become an important research field, which still remains a demanding task, mainly because most of the matter content in clusters is not visible.

Clusters are characterized by a virialized region within which all components (galaxies, intracluster medium and dark matter) are in rough dynamical equilibrium, where galaxy motions are well described by the Jeans formalism.

The cluster mass distribution can be measured through many complementary methods. The first approach to the cluster mass determination was the application of the virial theorem to the member galaxies (Zwicky, 1933). More sophisticated techniques are based on the hydrostatic measure of X-ray emissivity and temperature of the hot cluster gas (Ettori et al., 2002b; Borgani et al., 2004; Zappacosta et al., 2006; Schmidt & Allen, 2007; Host & Hansen, 2011), on the analysis of large-scale velocity field (Mohayaee & Tully, 2005) and on the analysis of the galaxy motions in clusters through the Jeans formalism. The radial profiles of total mass and velocity anisotropy of clusters have been constrained by Jeans analysis in several ways: predicting the observed radial profile of the line-of-sight velocity dispersion (Girardi et al., 1998), as well as kurtosis (Łokas & Mamon, 2003; Łokas et al., 2006); by isotropic (Katgert et al., 2004) or anisotropic mass inversion (Mamon & Boué, 2010). Alternative methods to use galaxy motions, are by fitting the Λ CDM distribution function (Wojtak et al., 2008) to the distribution of galaxies in projected phase-space density (Wojtak et al., 2009; Wojtak & Łokas, 2010) or by applying the caustic technique (Diaferio, 1999).

Observations (Rines & Diaferio, 2006), N-body simulations (Mamon et al., 2004; Wojtak et al., 2005; Cuesta et al., 2008) and a combination of both (Mahajan et al., 2011) have shown that virialized clusters are surrounded by infall zones from which most galaxies move into the relaxed cluster, as predicted by Gunn & Gott (1972). These galaxies are gravitationally bound to the cluster but are not fully virialized. This picture sparks multiple questions: does the infall motion affect the standard formalism? Can we detect the effect of the infall in cluster observations? Can this detection help to constrain the total mass of clusters? Below we will attempt to answer some of these questions.

The dynamical and X-ray based mass estimators depend on the hypothesis that the cluster is in steady-state dynamical or hydrostatic (for X-rays) equilibrium. The presence of non-stationary motions just outside the virial sphere may invalidate this assumption at that scale. For example, the standard Jeans formalism involves outwards integration along the line-of-sight, beyond the virial radius, hence into the regions with negative mean radial velocities, which are not accounted for. Moreover, the Jeans analysis relies on the assumption that the mean matter density of the Universe doesn't contribute to the gravitational potential (the so-called *Jeans Swindle*), and doesn't take into account the effect of the expansion of the Universe. Therefore, the mass estimated through the usual methods may be significantly biased and not be the true dynamical mass of the cluster. Two additional methods have been developed to address this issue: gravitational lensing (e.g. Mandelbaum et al., 2010; Lombriiser, 2011), and the caustic technique (Diaferio, 1999; Serra et al., 2011), which are both independent of the dynamical state of the system. Zu & Weinberg (2013) developed also a novel technique for constrain-

ing the radial profiles of the infall velocity from the projected velocity distributions of galaxies around clusters.

The aim of this paper is to generalize the standard Jeans formalism to include radial streaming motions (i.e. infall), as well as cosmological terms. This leads to a more general Jeans equation that also describes the outer cluster region and simplifies to the standard Jeans equation when the infall and cosmological corrections are negligible, like inside the virial radius. Our motivation is to build a formalism with this *generalized Jeans equation* to measure more accurately the mass profiles of clusters beyond the virial radius. In Sect. 4.3, we develop the formalism of the generalized Jeans equation. We analyze a cosmological simulation in Sect. 4.4 to show that our generalized Jeans equation correctly reproduces the radial velocity dispersion and we determine the bias on the velocity dispersion obtained with the standard Jeans equation.

4.3 NON-EQUILIBRIUM DYNAMICS OF GALAXY CLUSTERS: THE GENERALIZED JEANS EQUATION

The lowest-order Jeans equation relates the gravitational potential Φ of the cluster to the dynamical properties of the galaxies. In spherical coordinates, the *standard Jeans equation* is (e.g., Binney & Mamon, 1982):

$$\begin{aligned} -\rho(r) \frac{d\Phi}{dr} &= -\rho(r) \frac{GM(r)}{r^2} \\ &= \frac{d(\rho\sigma_r^2)}{dr} + 2 \frac{\beta}{r} \rho\sigma_r^2. \end{aligned} \quad (4.1)$$

Here $\rho(r)$ is the density distribution of a tracer (e.g., the number density of galaxies in and around clusters), $M(r)$ is the *total* mass distribution (including dark matter) in the cluster, $\sigma_r(r)$ is the galaxy velocity dispersion along the radial direction and $\beta(r)$ is the velocity anisotropy parameter defined by

$$\beta(r) = 1 - \frac{\sigma_\theta^2(r) + \sigma_\phi^2(r)}{2\sigma_r^2(r)}, \quad (4.2)$$

where $\sigma_\theta(r)$ and $\sigma_\phi(r)$ are the longitudinal and azimuthal velocity dispersions (and are equal by spherical symmetry). The anisotropy parameter expresses the cluster's degree of radial velocity anisotropy. The value of β can vary from $\beta = -\infty$, corresponding to circular orbits ($\sigma_r = 0$), to $\beta = 1$, if orbits are perfectly radial ($\sigma_\theta = \sigma_\phi = 0$). When $\sigma_\theta = \sigma_\phi = \sigma_r$ the system is isotropic ($\beta = 0$).

In eq. (5.5), we neglect streaming motions and any time-dependence, i.e. the mean velocity components \bar{v}_i are identically zero and, therefore, the velocity dispersions correspond to the second moment of the velocity components $\sigma_i^2 = \overline{v_i^2}$.

We now wish to go beyond the stationary approximation and to take into account the possible presence of an infall motion of galaxies outside the virialized core of clusters.

When we include the galaxies with mean radial velocity $\bar{v}_r \neq 0$ and retaining time derivatives, the Jeans equation (obtained by taking the first velocity moment of the collisionless Boltzmann equation) becomes

$$-\rho \frac{d\Phi}{dr} = \frac{\partial(\rho\overline{v_r^2})}{\partial r} + \frac{\rho}{r} \left[2\overline{v_r^2} - (\overline{v_\theta^2} + \overline{v_\phi^2}) \right] + \frac{\partial(\rho\bar{v}_r)}{\partial t}. \quad (4.3)$$

The second-order velocity moment for the radial component is now related to the radial velocity dispersion σ_r and the first velocity moment, i.e. the mean radial velocity \bar{v}_r , by the

general expression

$$\overline{v_r^2} = \sigma_r^2 + \overline{v_r}^2. \quad (4.4)$$

We keep $\overline{v_\theta^2} = \sigma_\theta^2$ and $\overline{v_\phi^2} = \sigma_\phi^2$, since we still assume no net longitudinal and azimuthal motions, i.e. we ignore bulk meridional circulation and rotation. Using the continuity equation

$$\frac{\partial \rho}{\partial t} = -\frac{\partial(\rho \overline{v_r})}{\partial r} - \frac{2}{r} \rho \overline{v_r}, \quad (4.5)$$

the Jeans equation (4.3) can be put in the following form:

$$-\rho \frac{d\Phi}{dr} = \frac{\partial(\rho \sigma_r^2)}{\partial r} + 2 \frac{\beta}{r} \rho \sigma_r^2 + \rho \left[\overline{v_r} \frac{\partial \overline{v_r}}{\partial r} + \frac{\partial \overline{v_r}}{\partial t} \right]. \quad (4.6)$$

Therefore, the inclusion of non-equilibrated material leads to a modification in the dynamical terms on the r.h.s. of the standard Jeans equation (5.5), namely to the addition of two extra terms involving the mean radial motion of galaxies. This correction is negligible in the virialized core of the cluster, but it can become significant in the outer region.

Since we are now considering distances very far from the center of the cluster, we also need to take into account effects due to the underlying cosmology, meaning that the gravitational term in the Jeans equation also needs to be modified. The galaxies are subject to an attractive potential from the mean density of the background and a repulsive potential from the cosmological constant, and when we add these contributions, the potential gradient is given by

$$\frac{d\Phi}{dr} = \frac{GM(r)}{r^2} + \frac{4\pi}{3} G \rho_b r - \frac{1}{3} \Lambda r. \quad (4.7)$$

Here ρ_b is the mean density of the Universe, Λ the cosmological constant and $H = \dot{a}/a$ the Hubble constant. Introducing the dimensionless density parameter and cosmological constant commonly used

$$\Omega_m = \frac{8\pi G \rho_b}{3H^2}, \quad \Omega_\Lambda = \frac{\Omega_\Lambda}{3H^2}, \quad (4.8)$$

eq. (4.7) reads:

$$\frac{d\Phi}{dr} = \frac{GM(r)}{r^2} + qH^2 r, \quad (4.9)$$

in terms of the deceleration parameter:

$$q = -\frac{\ddot{a}a}{\dot{a}^2} = \frac{\Omega_m}{2} - \Omega_\Lambda. \quad (4.10)$$

In general, the radial velocity of galaxies can be written as the sum of the Hubble flow and a peculiar (infall) velocity flow:

$$\overline{v_r}(r, t) = H(t) r + \overline{v_p}(r, t), \quad (4.11)$$

and beyond the infall region surrounding the clusters, the peculiar velocity becomes negligible compared to the Hubble expansion:

$$\overline{v_r}(r, t) \approx H(t) r \quad \text{when } r \rightarrow \infty.$$

One can now compute the non-stationary terms in eq. (5.20) using eq. (5.21)

$$\overline{v_r} \frac{\partial \overline{v_r}}{\partial r} + \frac{\partial \overline{v_r}}{\partial t} = \overline{v_p} \frac{\partial \overline{v_p}}{\partial r} + H \left(\overline{v_p} + r \frac{\partial \overline{v_p}}{\partial r} \right) - qH^2 r + \frac{\partial \overline{v_p}}{\partial t}, \quad (4.12)$$

where we have written the time derivative of the Hubble parameter in terms of eq. (5.18) :

$$\dot{H} = -(q+1)H^2. \quad (4.13)$$

Inserting eqs. (4.9) and (5.22) into eq. (5.20), we obtain the *generalized Jeans equation*

$$\frac{\partial(\rho\sigma_r^2)}{\partial r} + 2\frac{\beta}{r}\rho\sigma_r^2 = -\rho \left[\frac{GM(r)}{r^2} + S(r,t) \right]. \quad (4.14)$$

Here ρ is the density of tracer. In this work, when applying the generalized Jeans equation to test halos, we will consider only the particles belonging to the selected halo as our tracer. The mass $M(r)$ is thus the test halo mass, without the contribution from other halos or the diffuse Universe.

Equation (4.14) differs from eq. (5.5) by the inclusion of the new term

$$S(r,t) = qH^2r + \left(v_r \frac{\partial v_r}{\partial r} + \frac{\partial v_r}{\partial t} \right) \quad (4.15)$$

$$= \bar{v}_p \frac{\partial \bar{v}_p}{\partial r} + H \left(\bar{v}_p + r \frac{\partial \bar{v}_p}{\partial r} \right) + \frac{\partial \bar{v}_p}{\partial t}. \quad (4.16)$$

Equations (4.14) and (4.16) extend the standard Jeans formalism to describe also the non-stationary dynamics of clusters, and in principle, hold at any radius.

In equation (4.16), the background density and the cosmological constant contributions to the gravitational potential, cancel exactly with the velocity term relative to the pure Hubble flow. Thus, including all the effects due to the underlying cosmology, corresponds to applying the Jeans Swindle (Falco et al., 2013a).

Therefore, the extra term $S(r,t)$ differs from zero only in the presence of infall velocity, i.e. setting $v_p(r,t) = 0$, we immediately recover the standard Jeans equation (5.5).

The most general solution of equation (4.14) provides the following expression for the radial velocity dispersion profile, depending on $\rho(r)$, $M(r)$, $\beta(r)$ and $\bar{v}_p(r,t)$

$$\begin{aligned} \sigma_r^2(r) &= \frac{1}{\rho(r)} \exp \left[-2 \int_0^r \frac{\beta(s)}{s} ds \right] \\ &\times \int_r^\infty \exp \left[2 \int_0^s \frac{\beta(\tilde{s})}{\tilde{s}} d\tilde{s} \right] \\ &\times \rho(s) \left[\frac{GM(s)}{s^2} + S(s,t) \right] ds, \end{aligned} \quad (4.17)$$

using equation (4.16) for $S(s,t)$.

4.4 COMPARISON WITH COSMOLOGICAL SIMULATIONS

4.4.1 THE SIMULATION

We analyze an N-body simulation with WMAP3 cosmological parameters, $\Omega_m = 0.24$, $\Omega_\Lambda = 0.76$, the dimensionless Hubble parameter $h = 0.73$, the spectral index of primordial density perturbations $n = 0.96$ and the power spectrum normalization $\sigma_8 = 0.76$. A box of size $160 h^{-1} \text{Mpc}$ and 1024^3 particles was used. Starting from a redshift $z = 30$, the evolution was followed using the MPI version of the Adaptive Refinement Tree (ART) code. A hierarchical friends-of-friends (FOF) algorithm was used for identifying clusters. The linking length

was $b = 0.17$ times the mean inter-particle distance, corresponding roughly to an overdensity relative to the mean of the Universe of $\Delta = (1.96/b^3) [\ln(c+1) - c/(c+1)] (1+c)^2/c^2 \simeq 549 (c/5)^{0.39}/(b/0.17)^3$ (adapted from More et al., 2011), where c is the concentration parameter, for halos with a NFW density profile (Navarro et al., 1996).¹ We define the virial radius of our halos as the radius of overdensity $\Delta = 387$ (i.e. overdensity of $\Delta_c = 92.8$ relative to the critical density of the Universe) appropriate for the cosmology of the simulation (with the approximation of Bryan & Norman, 1998).

In order to test the generalized Jeans equation, which includes the effect of the infall motion, we shall look at cosmological simulations of clusters, and we demonstrate how to reproduce their radial velocity dispersions for radii larger than the virial radius. To this end, we first need to choose functions to parametrize the density, the mass, the anisotropy parameter and the infall velocity of the simulation to handle them as analytical functions in equations (4.16) and (5.7).

4.4.2 ANALYTICAL APPROXIMATIONS TO DENSITY, ANISOTROPY AND MEAN RADIAL VELOCITY PROFILES

N-body simulations show that the density distribution of a Dark Matter halo, in the inner virialized region, is well described by a double power-law profile² (Kravtsov et al., 1998)

$$\rho_h(r) = \frac{\rho_s}{(r/r_s)^\eta (1+r/r_s)^\xi}. \quad (4.18)$$

Here r_s is the scale radius, ρ_s is the scale density, η and ξ are the slopes, with values close to 1 and 2 respectively, which correspond to the NFW model.

According to cosmological dark matter simulations (e.g. Mamon & Łokas, 2005 and references therein), the radial anisotropy typically varies from ($\approx 0 - 0.1$) at $r \approx 0$, increasing with the distance and reaching a maximum value ($\approx 0.3 - 0.8$) around 1 – 2 times the virial radius. Looking at larger radii, $\beta(r)$ also shows an almost universal trend: it drops to negative values, reaching a minimum, and then it approaches zero asymptotically (Wojtak et al., 2005; Ascasibar & Gottlöber, 2008). If we define r_0 as the radius at which $\beta(r)$ passes through zero before becoming negative, we can parametrize the anisotropy function as

$$\beta(r) = A \left(\frac{r}{r_v} \right)^\mu \left(\frac{r_0 - r}{r_v} \right) \left[1 + B \left(\frac{r}{r_v} \right)^\nu \right]^{-\chi}, \quad (4.19)$$

where r_v is the virial radius.

The new formalism also includes the mean infall velocity of galaxies as an additional unknown function. Simulations show a quite universal trend for the radial profile of the mean velocity up to very large radii. Figure 4.1 displays the mean radial velocity with the Hubble flow subtracted, i.e. the peculiar component \bar{v}_p , up to 4 virial radii, for three samples of stacked halos. The samples contain the same number of halos and the mass ranges are: a very narrow bin around $5 \times 10^{13} M_\odot$ (green dot-dashed line), $(0.78 - 1.00) \times 10^{14} M_\odot$ (black, solid line), $(1.4 - 1.8) \times 10^{14} M_\odot$ (red dashed line). The velocity is negative everywhere, clearly showing the infall motion, particularly pronounced between ≈ 1 and $4 r_v$. The three profiles appear to look very similar.

¹The approximation $\Delta \simeq 549 (c/5)^{0.39}/(b/0.17)^3$ is accurate to 0.7% for $2.5 < c < 10$.

²In the case of pure Dark Matter halos, the tracer corresponds to Dark Matter particles, thus: ρ in equation (5.7) corresponds to the density in eq (4.18).

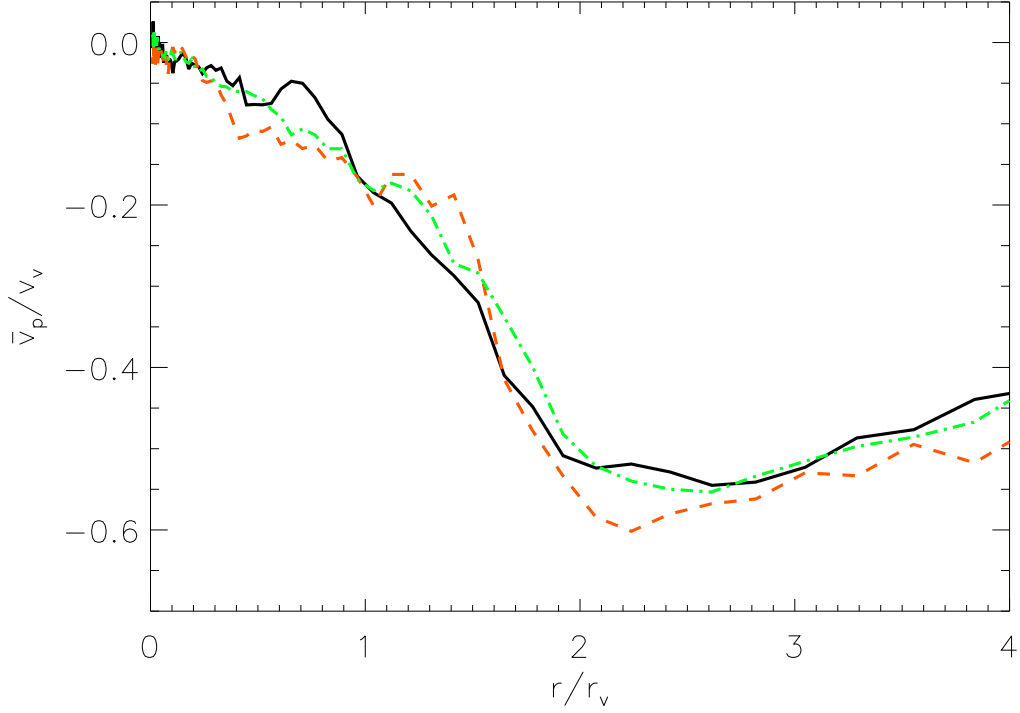


Figure 4.1 Mean peculiar radial velocity of three samples of stacked halos. The mass ranges for the samples are: a very narrow mass range around $5 \times 10^{13} M_{\odot}$ (green dot-dashed line), $(0.78 - 1.00) \times 10^{14} M_{\odot}$ (black, solid line), $(1.00 - 1.27) \times 10^{14} M_{\odot}$ (red dashed line).

In the innermost region, the cluster is fully equilibrated ($\bar{v}_r = 0$). The peculiar velocity profile can then be approximated, for $r \ll r_v$, as

$$\bar{v}_p(r, t) \approx -H r \quad . \quad (4.20)$$

In general, the mean peculiar velocity can be written as

$$\bar{v}_p(r, t) = -H(t) r_v(t) f\left(\frac{r}{r_v(t)}\right) , \quad (4.21)$$

where $f(r/r_v)$ must be such that the condition (4.20) is satisfied. As we will show in the next sections, the function $f(r/r_v)$ is well approximated by the formula:

$$f\left(\frac{r}{r_v}\right) = \left\{ \left[\left(\frac{r}{r_v}\right)^{-a} + C \left(\frac{r}{r_v}\right)^b \right]^{1/a} - D \right\}^{-1} . \quad (4.22)$$

Equation (4.16) involves the time derivative of the radial infall velocity. Equations (4.21) and (4.22) describe a profile where the dependence on time is through $H(t)$ and $r_v(t)$. The function that describes the radial shape of the velocity, eq. (4.22), might change in time as well. We parametrize this dependence by multiplying eq. (4.21) by a factor that involves time only:

$$\bar{v}_p(r, t) = -H(t) r_v(t) f\left(\frac{r}{r_v(t)}\right) \left(\frac{t}{t_0}\right)^{\alpha} , \quad (4.23)$$

where t_0 is the present age of the Universe.

We can now explicitly calculate the time derivative of $v_p(r)$ and complete the computation of the extra term $S(r, t)$, which then obeys

$$\begin{aligned} \frac{t S(r, t)}{v_p(r, t)} = & H t \left[1 + \frac{d \ln f}{d \ln x} - \frac{d f}{d x} \left(\frac{t}{t_0} \right)^\alpha \right] \\ & + \frac{d \ln H}{d \ln t} + \frac{d \ln r_v}{d \ln t} \left(1 - \frac{d \ln f}{d \ln x} \right) + \alpha, \end{aligned} \quad (4.24)$$

where $x = r/r_v$.

The parameter α describing the departure from self-similarity of the evolution of the infall velocity profile in virial units is not well known. In the following sections, we analyze Figure 13c of Cuesta et al. (2008), describing this evolution for stacked halos, to deduce that $\alpha \approx -0.55 \pm 0.1$ (see Fig. 4.2). Since we are analyzing our simulation at $z = 0$, the precise value of α probably depends on the radial shape of the velocity at the present time. We consider it as a free parameter of our model, and we expect it to vary with a small scatter, when considering different velocity profiles.

In what follows, we estimate $d \ln r_v / d \ln t$ using the mass growth rates measured in cosmological simulations as well as through analytical theory, to conclude that the mean growth of halos at $z = 0$ for the cosmology of our simulation and for the halo mean mass and concentration parameter is $d \ln r_v / d \ln t \simeq 0.7$. We note that observers will tend to discard clusters having undergone recent mergers, while we stack 27 halos regardless of their recent merger history, so that observers will effectively choose halos with slightly smaller values of $d \ln r_v / d \ln t$. We also compute the minimal growth of a fully isolated halo in an expanding universe, and find $d \ln r_v / d \ln t \simeq 0.68$, which is only very slightly lower.

Having expressions for ρ , M , β , and \bar{v} , we can then use eq. (5.7) to calculate the radial velocity dispersion of simulated halos, which we can compare to the true dispersion profile. In the next sections, we show the results obtained for a sample of stacked halos and for two isolated halos.

Departure from self-similarity of the evolution of the peculiar velocity

Cuesta et al. (2008) have measured the mean radial infall velocity as a function of radius, averaging over haloes of different mass, and repeating the exercise at $z = 0, 1$ and 2. Their fig. 13c shows that the infall pattern is not self-similar, but instead decreases in time (in virial units). We converted their mean radial velocity to peculiar velocity (subtracting the Hubble flow). Fig. 4.2 shows that the evolution of the mean peculiar velocity in virial units is not self-similar: the black curves do not lie on top of one another. Assuming that $v_p(r, t) / [H(t)r_v(t)]$ scales as $(t/t_0)^\alpha$ improves the self-similarity. The peak peculiar velocities are reproduced for $\alpha = -0.65$, but the absolute peculiar velocities at large radii are overpredicted. Choosing $\alpha = -0.45$ represents a good compromise over the range of radii that are relevant: those where we measure the radial velocity dispersion and those slightly beyond that take part in the outwards integration of equation (4.14).

Growth rate of the virial radius

There are several ways to compute the logarithmic growth rate of the virial radius, $d \ln r_v / d \ln t$.

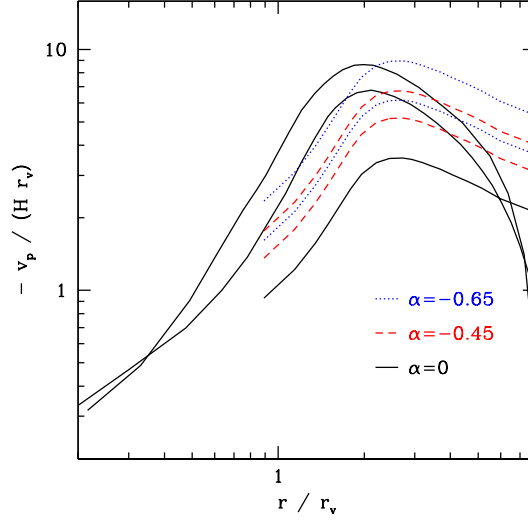


Figure 4.2 Time evolution of the mean peculiar velocity profile (in virial units). The black curves show the peculiar velocity measured in simulations at $z = 0, 1,$ and 2 (going upwards at $r = 2r_v$), adapted from fig. 13c of Cuesta et al. (2008). The red and blue curves show the predictions for $z = 1$ and 2 obtained by extrapolating the $z = 0$ curve with $(t/t_0)^\alpha$. Two values of α are shown: one ($\alpha = -0.65$) that matches best the maximum absolute value of the peculiar velocity and one ($\alpha = -0.45$) that represents a best compromise over the relevant range of radii.

Self-similar growth in Einstein de Sitter universe For a single halo in a universe with present-day density and dark energy parameters $\Omega_m = 1$ and $\Omega_\Lambda = 0$, one simply has $d \ln r_v / d \ln t = 8/9 \simeq 0.89$, independent of the halo mass (Gunn & Gott, 1972).

Exponential halo mass evolution with redshift Wechsler et al. (2002) analysed cosmological simulations and derived $M_v(z) = M(z=0) \exp(-\alpha z)$, with $\alpha \approx 0.6$ for haloes of mass close to those considered here ($M \approx 8 \times 10^{13} M_\odot$). With

$$M_v = \frac{\Delta}{2} \frac{H^2 r_v^3}{G}, \quad (4.25)$$

this yields

$$\frac{d \ln r_v}{d \ln t} = \frac{1}{3} \left(\frac{d \ln M_v}{d \ln t} - \frac{d \ln \Delta}{d \ln t} - 2 \frac{d \ln H}{d \ln t} \right). \quad (4.26)$$

One can write $d \ln M_v / d \ln t = -\alpha / (d \ln t / dz)$. Given that, for a flat universe, one has (Peebles, 1993, equation 13.20)

$$H_0 t(z) = \frac{2}{3\sqrt{1-\Omega_m}} \sinh^{-1} \left(\frac{\sqrt{(1/\Omega_m) - 1}}{(1+z)^{3/2}} \right), \quad (4.27)$$

one finds

$$\left(\frac{d \ln t}{dz} \right)_{z=0} = -\frac{3}{2} \frac{\sqrt{1-\Omega_m}}{\sinh^{-1} \sqrt{1/\Omega_m - 1}}, \quad (4.28)$$

which tends to -0.975 for the density parameter of our simulation, $\Omega_m = 0.24$. We deduce that $d \ln M_v / d \ln t \simeq 0.615$.

Given that, for a flat universe, one also has (Peebles, 1993, equation 13.3)

$$E(z) = \frac{H(z)}{H_0} = \sqrt{\Omega_m(1+z)^3 + 1 - \Omega_m}, \quad (4.29)$$

one deduces

$$\begin{aligned} \frac{d \ln H}{d \ln t} &= -\frac{\Omega_m}{\sqrt{1 - \Omega_m}} (1+z)^3 \frac{\sqrt{1 - \Omega_m [1 - (1+z)^3]}}{1 + \Omega_m z (3 + 3z + z^2)} \sinh^{-1} \left(\frac{\sqrt{1/\Omega_m - 1}}{(1+z)^{3/2}} \right) \\ &= -\frac{\Omega_m}{1 - \Omega_m} \sinh^{-1} \left(\sqrt{1/\Omega_m - 1} \right) \quad (z = 0), \end{aligned} \quad (4.30)$$

$$\simeq -0.402 - 1.08 (\Omega_m - 0.27) - [0.638 + 0.698 (\Omega_m - 0.27)] z, \quad (4.31)$$

where the approximation is from a series expansion and is accurate to better than 1.7% (0.7% rms) for $0 < z < 0.2$ and $0.24 < \Omega_m < 0.3$. So for our case of $\Omega_m = 0.24$ and $z = 0$, equation (4.30) yields $d \ln H/d \ln t \simeq -0.37$.

Finally, using the approximation (Bryan & Norman, 1998)

$$\Delta \simeq 18 \pi^2 + 82 [\Omega_m(z) - 1] - 39 [\Omega_m(z) - 1]^2 \quad (4.32)$$

where

$$\Omega_m(z) = \frac{\Omega_m (1+z)^3}{E^2(z)} \quad (4.33)$$

(see eq. [4.29]), we find the series expansion

$$\frac{d \ln \Delta}{d \ln t} \simeq -0.841 + 0.570 (\Omega_m - 0.27) + [0.337 + 5.47 (\Omega_m - 0.27)] z + [1.447 - 6.01 (\Omega_m - 0.27)] z^2, \quad (4.34)$$

which is accurate to better than 2.4% (0.9% rms) for $0 < z < 0.2$ and $0.24 < \Omega_m < 0.3$. For $\Omega_m = 0.24$ and $z = 0$, equation (4.34) yields $d \ln \Delta/d \ln t \simeq -0.85$. Putting this altogether, we deduce that $d \ln r_v/d \ln t \simeq 0.735$.

Scaling with inverse Hubble time Zhao et al. (2003) noted that $r_v \propto 1/H$. With $d \ln H/d \ln t \simeq -0.37$ (Section 4.4.2), we obtain $d \ln r_v/d \ln t \simeq 0.37$ for the Zhao et al. approximation.

Constant circular velocity Mamon et al. (2012) noted that the mean growth of haloes follows roughly $v_{\text{circ}}(r_v) = \text{const.}$ Equation (4.25) then implies that $r_v \propto 1/(H\sqrt{\Delta})$. With $d \ln H/d \ln t \simeq -0.37$ and $d \ln \Delta/d \ln t \simeq -0.85$ (Section 4.4.2), we derive $d \ln r_v/d \ln t \simeq 0.795$ for the constant circular velocity approximation, close to the $\Omega_m = 1$ slope, but far from the slope with the Zhao et al. approximation.

Halo merger rate in Millennium simulations Fakhouri et al. (2010) have measured the halo merger rate in the Millennium and Millennium-II cosmological dark matter simulations. Their equation (2) provides the mean and median mass growth rates as $dM_v/dt = a (M_v/10^{12} M_\odot)^{1.1} (1 + bz) E(z)$, with $a = 46$ (mean) or 25 (median) $M_\odot \text{ yr}^{-1}$ and $b = 1.11$ (mean) or 1.65 (median). Hence,

$$\frac{d \ln M_v}{d \ln t} = \frac{a}{10^{12}} t(z) \left(\frac{M_v}{10^{12} M_\odot} \right)^{0.1} (1 + bz) E(z), \quad (4.35)$$

where $t(z)$ is measured in yr. The (slightly) positive slope on mass recovers the fact that high-mass haloes are rare today and even rarer in the past, and must therefore grow faster. Combining with equation (4.25), one obtains

$$\begin{aligned} \frac{d \ln r_v}{d \ln t} \simeq & 0.548 + 0.00511 \frac{a}{h} + \left(0.530 - 0.005 \frac{a}{h}\right) (\Omega_m - 0.27) \\ & + \left[0.426 - 0.00308 \frac{a}{h} (1 - 1.66 b)\right] z + 0.00118 \frac{a}{h} (\log M - 14). \end{aligned} \quad (4.36)$$

Equation (4.36) is accurate to 4% (1.4% rms) for $0 < z < 0.2$, $0.24 < \Omega_m < 0.3$, and $12 < \log M/M_\odot < 15.4$. Equations (4.26) and (4.35) yield $d \ln r_v/d \ln t \simeq 0.74, 0.79, 0.86$, and 0.95 (mean) or $0.64, 0.67, 0.71$ and 0.76 (median) for $\Omega_m = 0.24$, $h = 0.73$, $z = 0$, and $\log M = 12, 13, 14$, and 15 , respectively.

Extended Press-Schechter theory Neistein & Dekel (2008) use extended Press-Schechter theory to derive a mass growth rate that can be written as $d \ln M_v/d \ln t = -\alpha t \dot{\omega} (M/10^{12} M_\odot)^\beta$ with $\dot{\omega} \simeq -0.047 [1 + z + 0.1(1+z)^{-1.25}]^{2.5} (h/0.73) \text{ Gyr}^{-1}$, $\alpha = 0.59$ and $\beta = 0.141$. With equations (4.29), (4.26), and (4.34), this leads to the series expansion

$$\begin{aligned} \frac{d \ln r_v}{d \ln t} \simeq & 0.548 + 0.264 \alpha 10^{2\beta} + (0.530 - 0.268 \alpha 10^{2\beta}) (\Omega_m - 0.27) \\ & + (0.426 + 0.259 \alpha 10^{2\beta}) z + 0.607 \alpha \beta 10^{2\beta} (\log M - 14). \end{aligned} \quad (4.37)$$

Equation (4.37) is good to 7.6% (2.4% rms) accuracy in the range $0 < z < 0.2, 0.24 < \Omega_m < 0.3, 12 < \log M/M_\odot < 15.4$. The exact solution yields $d \ln r_v/d \ln t = 0.69, 0.75, 0.84$, and 0.96 for $z = 0, \Omega_m = 0.24$, and $\log M = 12, 13, 14$ and 15 , respectively.

Minimum growth rate We can estimate a *minimum* growth rate by considering the growth of a single halo in a uniform universe. Assuming an NFW density profile at all times, with mass profile

$$M(r, t) = M(a) \widetilde{M} \left(\frac{r}{a} \right) \quad (4.38)$$

$$\widetilde{M} \left(\frac{r}{a} \right) = \frac{\ln(x+1) - x/(x+1)}{\ln 2 - 1/2}, \quad (4.39)$$

where a is the radius of slope -2 and does not vary in time. The virial radius r_v is the solution to

$$\frac{3 M(r, t) / (4\pi r^3)}{3 H^2(t) / 8\pi G} = \Delta(t) \quad (4.40)$$

i.e., using equation (4.39),

$$\frac{2 G M(a)}{a^3} \frac{\widetilde{M}(c)}{c^3} = \Delta(t) H^2(t), \quad (4.41)$$

where $c = r_v/a$ is the concentration parameter. Now we do not need to solve equation (4.41) for c to obtain the growth rate of r_v . Indeed, at time $t + dt$, where $dt \ll t$, equation (4.41) becomes

$$\frac{2 G M(a)}{a^3} \frac{\widetilde{M}(c)}{c^3} \left[1 + \left(\frac{d \ln \widetilde{M}}{d \ln x} \right)_{x=c} \frac{dc}{c} - 3 \frac{dc}{c} \right] = \Delta(t) H^2(t) + \frac{d(\Delta H^2)}{d \ln t} d \ln t. \quad (4.42)$$

Dividing equation (4.42) by equation (4.41), one obtains

$$\frac{d \ln r_v}{d \ln t} = \frac{d \ln c}{d \ln t} = \frac{(d \ln \Delta / d \ln t) + 2 (d \ln H / d \ln t)}{(d \ln \widetilde{M} / d \ln x)_{x=c} - 3}. \quad (4.43)$$

After a series expansion, equation (4.43) becomes

$$\frac{d \ln r_v}{d \ln t} \simeq 0.723 + 0.413 z + 0.698 (\Omega_m - 0.27) - 0.207 (\log c - 0.7) - 1.79 (\Omega_m - 0.27) z. \quad (4.44)$$

The approximation of equation (4.44) is accurate to 3.7% (1.4% rms) for $0 < z < 0.2$, $0.24 < \Omega_m < 0.3$, and $0.5 < \log c < 1$. For $\Omega_m = 0.24$ and $z = 0$, equation (4.43) yields $d \ln r_v / d \ln t = 0.75$, 0.70 , 0.67 , and 0.65 for $c = 3, 5, 7$, and 10 , respectively. One therefore notices that Zhao et al.'s approximation of $r_v \propto 1/H$ yields a slower growth rate for r_v than our minimum growth rate found here. Note that, for $\Omega_m = 1$ and $z = 0$, the minimum growth rate is $d \ln r_v / d \ln t \simeq 0.879 + 0.252 (\log c - 0.7)$, not far from the Einstein de Sitter universe growth rate (Gunn & Gott, 1972, see Section 4.4.2), with equality for $c = 4.57$.

Summary In summary, for the cosmology of our simulation, at $z = 0$ for our mean halo mass of $8.6 \times 10^{13} M_\odot$ and concentration parameter $c = 6.4$, we find $d \ln r_v / d \ln t = 0.86$ (from Fakhouri et al.'s analysis of the merger rate in the Millennium simulations), 0.795 (for our constant circular velocity approximation), 0.735 (from Wechsler et al. et al's exponential mass growth), 0.71 (from Neistein & Dekel's extended Press-Schechter theory), 0.68 for the minimal growth scenario, but only 0.37 for Zhao et al.'s scaling with inverse Hubble time. We consider this last scaling as inaccurate and we adopt $d \ln r_v / d \ln t = 0.7$, slightly above our minimal growth scenario.

Relations between slopes

Here we present the results of the simulations at slightly larger radii, and consider relations between parameters of interest, in particular we show the derivative of the density, γ , and of the radial velocity dispersion, κ . We also present plots in the 2 dimensional spaces $\gamma - \kappa$ and $\gamma - \beta$ for distances up to $\approx 6r_v$.

Various numerical simulations have identified a range of apparent universalities, where some are identified in cosmological simulations, and others are found in controlled simulations. Most of these universalities are usually considered in radial ranges where the systems are fully equilibrated. Since we are considering here radial ranges much beyond the virial radius, it is relevant to study these properties at large radii.

Probably the most famous universality is the density profile as a function of mass (Navarro et al., 1996). It suggests that the density slope

$$\gamma = \frac{d \log \rho}{d \log r} \quad (4.45)$$

has a smooth transition from -1 in the inner region, to -3 in the outer region. The corresponding plot is shown for the stacked clusters in Fig. 4.3. It is clearly seen that around the virial radius the density profile flattens out, and the logarithmic slope approaches -1 around three times the virial radius. The green line shows the prediction for the double slope profile with parameters in Table 4.2.

Fig. 4.4 shows the relation between γ and the velocity dispersion anisotropy given by equation (4.2). This is quite in agreement with the universality proposed in (Hansen & Stadel, 2003)

$$\beta = -0.2(\gamma + 0.8) \quad (4.46)$$

in the inner region, but departs significantly for $\gamma < -2.2$.

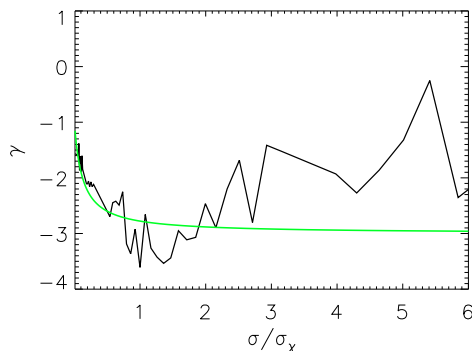


Figure 4.3 Logarithmic derivative of the density profile γ (equation 4.45). Starting from $\gamma \approx -1$, the slope of the density function decreases reaching ≈ -3.2 at around two times the virial radius, and in the outer region it increases again approaching zero. The green line shows the prediction for the double slope profile with parameters in Table 4.2

A connection between γ and the radial velocity dispersion was suggested by (Taylor & Navarro, 2001; Ludlow et al., 2011)

$$\frac{\rho}{\sigma^3} \approx r^{-\alpha}, \quad (4.47)$$

where $\alpha = 1.875$, in agreement with the prediction from the spherical infall model (Bertschinger, 1985). In Fig. 4.5 the derivative of the velocity dispersion is displayed:

$$\kappa = \frac{d \log \sigma_r^2}{d \log r}. \quad (4.48)$$

Equation (4.47) in terms of κ and γ reads

$$\gamma = -\alpha + \frac{3}{2}\kappa. \quad (4.49)$$

The connection in the $\gamma - \kappa$ space is in fair agreement with the formula (4.49), as we show in Fig. 4.6.

4.4.3 COMPARISON WITH A STACKED HALO

We begin by selecting a sample of 27 stacked cluster-size halos from our simulation, with virial masses in the range $[(0.78 - 1.0) \times 10^{14} M_\odot]$. We denote this sample as our *stacked halo*. The characteristic quantities of the stacked halo, are taken as the mean of the 27 individual halos, and are listed in Table 4.1.

Figure 4.7 shows the profiles of $r^2\rho(r)$ (top panel) and $\beta(r)$ (bottom panel) for the stacked halo. The black solid lines are the median profiles from the simulation, the black dotted lines correspond to the first and the third quartiles, and the red dashed lines are our fits.

The density can be well approximated in the region ($r < 3r_v$) using the double-power formula of equation (4.18), with parameters listed in Table 4.2. The simulated density profile increases beyond a turn-around radius of $3 - 4r_v$, due to the presence of other structures surrounding the halo. Our model describes an isolated system, therefore we don't take into account the presence of other structures.

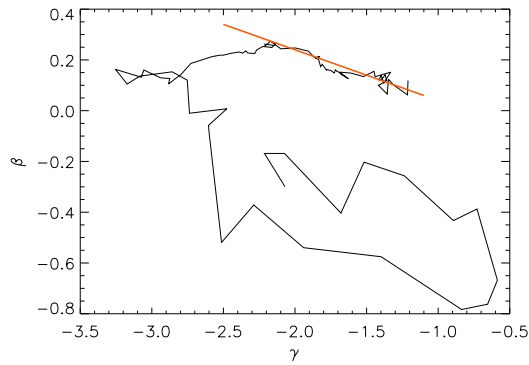


Figure 4.4 Velocity anisotropy β as a function of the radial derivative of the density profile γ . The red solid line corresponds to equation (4.46) (Hansen & Stadel, 2003).

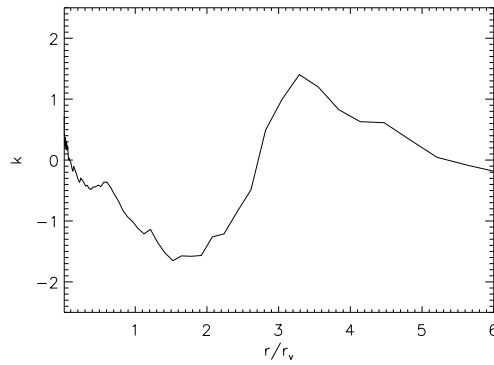


Figure 4.5 Logarithmic derivative of the radial velocity dispersion κ , as defined by equation 4.48.

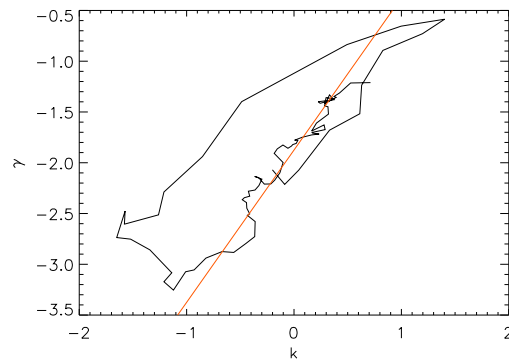


Figure 4.6 Derivative of the radial velocity dispersion κ as a function of the logarithmic slope of the density profile γ . The red solid line corresponds to the equation (4.49) (Taylor & Navarro, 2001; Ludlow et al., 2011).

Table 4.1 Virial parameters and concentrations of the halos

	M_v ($10^{13} M_\odot$)	r_v (Mpc)	v_v (km s^{-1})	c
Stacked	8.6	1.14	569	6.4
Halo 1	8.4	1.13	566	6.9
Halo 2	7.8	1.10	553	7.6

Table 4.2 Parameters of empirical fits to $\rho(r)$ (with eq. [4.18]), $\beta(r)$ (with eq. [4.19]) and $v_p(r)$ (with eq. [4.21]) for the stacked halos.

$\rho(r)$	$\beta(r)$	$v_p(r)$
$\rho_s = 2.4 M_v / r_v^3$	$\mu = 0.48$	$a = 9.7$
$r_s = 0.38 r_v$	$\nu = 9.5$	$b = 2.8$
$\eta = 1.35$	$\chi = 0.37$	$C = 5.7 \times 10^{-5}$
$\xi = 1.96$	$A = 0.35$	$D = 0.214$
	$B = 5 \times 10^{-5}$	

The anisotropy profile is well fit by eq. (4.19) up to $4 r_v$. In our case, $r_0 = 1.55 r_v$, and the other best-fit parameters for the anisotropy are listed in Table 4.2.

According to eq. (5.7), the radial velocity dispersion also requires the knowledge of the mean peculiar radial velocity profile of the sample. In the upper panel of Figure 4.8 are displayed the mean peculiar velocity of our sample (black solid line), quartiles (black dotted lines), and $\bar{v}_p(r)$ given by formula (4.21), with parameters listed in Table 4.2 (red dashed line). The green dashed-dotted line represents the case of zero peculiar velocity.

The radial velocity dispersion is shown in the central panel of Figure 4.8. The black solid line is the simulated profile and the black dotted lines are the first and the third quartiles. The green dashed-dotted line is the velocity dispersion profile from the standard Jeans equation (5.5). We compute the velocity dispersion by using equation (5.7) where the extra term is given by equation (4.24), and best parameters in Table (4.2) (red dashed line). We find that the best solution is given by setting $\alpha = -1$. This value of α is more negative than the value of $\approx -0.55 \pm 0.1$ that we infer (Fig. 4.2) from the evolution of the stacked cluster-mass halo of Cuesta et al. (2008).

The radial velocity dispersion profile measured for the halo matches very well the one predicted by our generalized Jeans equation (5.7) all the way out to $4 r_v$. The standard Jeans formalism can predict σ_r up to $\approx 2 r_v$, where the infall and the cosmological corrections are still very small or cancel out. In the region where these contributions are significant the radial velocity dispersion inferred from eq. (5.5) is overestimated by $\approx 20\%$ in the range $\approx 2 - 3$ virial radii, as shown in the bottom panel of Figure 4.8. The slope of σ_r becomes steeper in the region of non-equilibrium, and this is well reproduced by eq. (5.7).

4.4.4 COMPARISON WITH ISOLATED HALOS

The example in the previous section demonstrates the correctness of this generalized formalism when applied to a stacked sample of cluster-size halos. However, when taking the median profiles of the stacked sample, we are not guaranteed that the individual halos will have the same

Table 4.3 Parameters of empirical fits to $\rho(r)$ (with eq. [4.18]), $\beta(r)$ (with eq. [4.19]) and $v_p(r)$ (with eq. [4.21]) for the *halo 1* and the *halo 2*.

	$\rho(r)$	$\beta(r)$	$v_p(r)$
halo 1	$\rho_s = 2.45 M_v/r_v^3$	$\mu_{\text{inner}} = 0.5$	$a = 4.75$
	$r_s = 0.4 r_v$	$\mu_{\text{outer}} = 2.0$	$b = 2.5$
	$\eta = 1.37$	$\nu = 23.0$	$C = 4.8 \times 10^{-3}$
	$\xi = 2.22$	$\chi = 0.23$	$D = 0.29$
		$A = 0.6$	
		$B = 6 \times 10^{-11}$	
halo 2	$\rho_s = 41 M_v/r_v^3$	$\mu_{\text{inner}} = 0.57$	$a = 4.8$
	$r_s = 0.11 r_v$	$\mu_{\text{outer}} = 2.0$	$b = 2.6$
	$\eta = 0.9$	$\nu = 24.6$	$C = 2.4 \times 10^{-3}$
	$\xi = 2.1$	$\chi = 0.25$	$D = 0.21$
		$A = 0.5$	
		$B = 2.1 \times 10^{-11}$	

profiles. Our median quantities based upon a sample with an odd number of halos, effectively correspond to a single halo. However, the halo involved in the median density at a given radius, may not be the same as that involved in the median radial velocity, or that for the median velocity anisotropy.

A further test is therefore to apply the same approach also to individual halos in the sample, in order to be independent of the analysis of the median profiles. Our model describes the dynamics of clusters when they are isolated. Thus, we need to look for halos in our sample which are not surrounded by massive neighbors. In particular, we have searched for halos which have no neighbors with mass at least half of theirs, within a distance of $10 r_v$. With this criterion, we have selected two optimal halos among the 27 belonging to our sample. We denote our halos as *halo 1* and *halo 2*. The virial masses, radii, velocities as well as their concentrations are listed in Table 4.1.

Figure 4.9 shows the profiles $r^2\rho(r)$ (top panels) and $\beta(r)$ (bottom panels) for the two individual halos. We fit the profiles with equations respectively (4.18) for the density and (4.19) for the anisotropy. In the outer region, where the anisotropy takes negative values, the profiles of both halos are much steeper than the median profile of the stacked halo. Therefore, in eq. (4.19) it is convenient to use two different slopes : μ_{inner} for $r < r_0$ and μ_{outer} for $r > r_0$. For both halos, $r_0 = 1.75 r_v$. The best fit parameters are shown in Table (4.3).

The infall velocity profiles of the halos are displayed in the upper panels of Figure (4.10). The corresponding radial velocity dispersion profiles are shown in the middle panels. The black solid lines are the simulated profiles, and the red dashed lines correspond to the solution of eq. (5.7), in the case of $v_p(r)$ given by our fits. We find the value $\alpha = -0.65$ provides a good match to the velocity dispersion for both halos. The green dashed-dotted lines are the velocity dispersion profiles from the standard Jeans equation (5.5).

Also in the case of these two isolated halos, we find that our prediction of the velocity dispersion matches very well the measured profiles. The standard Jeans solution provides a good match up to $\approx 2 r_v$, while our generalized Jeans equation improves the match at distances $\approx 2 - 4 r_v$.

The bottom panels of Fig. (4.10) show the ratio between the standard Jeans solution and our

generalized solution. For the isolated halos, the ratio is slightly bigger than the one computed for the stacked sample. The velocity dispersion calculated by the standard Jeans equation is overestimated by $\approx 40\% - 60\%$ for the first halo and $\approx 40\%$ for the second halo, in the range $\approx 2 - 4$ virial radii.

Instead of considering σ_r for given mass and anisotropy profiles, one can estimate the error in the mass profile derived from the standard Jeans equation (5.5), relative to that derived from the generalized Jeans equation, for given $\sigma_r(r)$ and $\beta(r)$. Comparing with the standard and generalized Jeans equations, one finds that the mass derived from the standard Jeans equation (5.5) can be written as

$$M_{\text{std-Jeans}}(r) = \left[1 + \frac{S(r)}{GM(r)/r^2} \right] M(r), \quad (4.50)$$

where $M(r)$ is the mass profile obtained from the generalized Jeans equation. Figure 4.11 shows that beyond the virial radius, the corrections to the standard Jeans equation (5.5) are not negligible: in the range $\approx 2 - 4 r_v$, the correction causes the standard Jeans equation to underestimate the total mass by $\approx 20 - 60\%$ for *halo 1* and $\approx 20 - 40\%$ for *halo 2*.

4.5 CONCLUSIONS AND DISCUSSION

The general purpose of this work is to improve our understanding of the dynamics of galaxies that are still falling onto relaxed clusters, with the motivation of performing a Jeans analysis of the mass profile out to several virial radii, for possible cosmological applications. The standard Jeans equation describing the cluster dynamics, assumes the system to be in equilibrium, with no mean radial streaming motions, and therefore it cannot be applied beyond the fully virialized cluster zone.

We have presented a generalized Jeans equation that takes into account the non-zero mean radial velocities of galaxies outside the virial radius, as well as the background density and the cosmological constant terms. We accurately reproduce the radial velocity dispersion profiles of a stack of 27 cluster-mass halos and of two isolated halos, out to 4 virial radii. In particular, while the standard Jeans equation provides accurate radial velocity dispersions out to ≈ 2 virial radii, it over estimates the radial velocity dispersion by typically a factor 1.5 beyond ≈ 3 virial radii. In the standard Jeans formalism, the total mass is underestimated by $\approx 20 - 60\%$ in the region $\approx 2 - 4 r_v$.

A consistent description of cluster dynamics in the infall region can be useful for an accurate dynamical mass measurement at the infall scale. The estimation of mass profiles with the standard Jeans analysis involves the modeling of the line-of-sight velocity dispersion of the tracer (i.e. galaxies in clusters) by solving the lowest-order Jeans equation, to compare with that obtained from taking the 2nd moments of the observed galaxy line-of-sight velocities. This also involves a measurement of the radial velocity anisotropy of galaxies. Just as several approaches have been proposed to break the mass-velocity anisotropy degeneracy inherent to the standard Jeans equations, we wish to do the same when applying the generalized Jeans equation all the way to several virial radii, except that we also need to determine a third quantity : the mean infall velocity. As our parameterized approach to recover the radial velocity dispersion profile beyond the virial radius requires 12 free parameters, it should be viewed more as a proof of concept that the standard Jeans equation is adequate in determining the radial velocity dispersion profile up to 2 virial radii and inadequate beyond, rather than being a method to accurately determine the radial velocity dispersion profile from observational data. Karachentsev & Nasonova (2010) recover the infall pattern of the Virgo cluster, with the knowledge of the depth

along the line-of-sight obtained from distance indicators independent of redshift (Mei et al., 2007). However, the uncertainties on the velocities appear to be too large for reproducing the radial velocity dispersion profile more accurately with the generalized Jeans equation than with the standard Jeans equation.

The model also involves the logarithmic growth rate of the virial radius as well as the departure from self-similarity of the evolution of the infall velocity profile. We have presented 7 theoretical derivations for the logarithmic growth rate of the virial radius (as a function of mass or concentration), which lead to similar values. On the other hand, our stacked halo leads to a different non self-similarity parameter (α) than our two isolated halos. We suspect that this parameter is not universal, but strongly depends on the mass accretion history of the halo. It would be useful to analyze the non self-similarity parameter in more detail with simulations.

We finally note that with infall present, the kinetic energy is expected to be larger than in the case with no infall. The virial ratio, $2K/W = 1$ can be seen as a spatial integral over the Jeans equation, where K and W represent the total kinetic energy and the total potential energy of the system. One therefore expects the virial ratio to be larger than unity for systems where infall is important (Cole & Lacey, 1996; Power et al., 2012).

We are planning an extension of this work to test how far the standard Jeans equation is relevant in reproducing the line-of-sight velocity dispersion profile and possibly find signatures of infall in the shape of the line-of-sight velocity profile.

G.A.M. is indebted to James Binney and Ewa Łokas for useful discussions at a very early stage of this work and Avishai Dekel for useful comments throughout. He thanks DARK for their hospitality during the visit that launched the collaboration, while M.F. thanks the IAP for their hospitality during two visits. The authors thank Antonio Cuesta for providing simulation data in digital form, helping us to build Figure (4.2). The simulation has been performed at the Leibniz Rechenzentrum (LRZ) Munich. The Dark Cosmology Centre is funded by the Danish National Research Foundation.

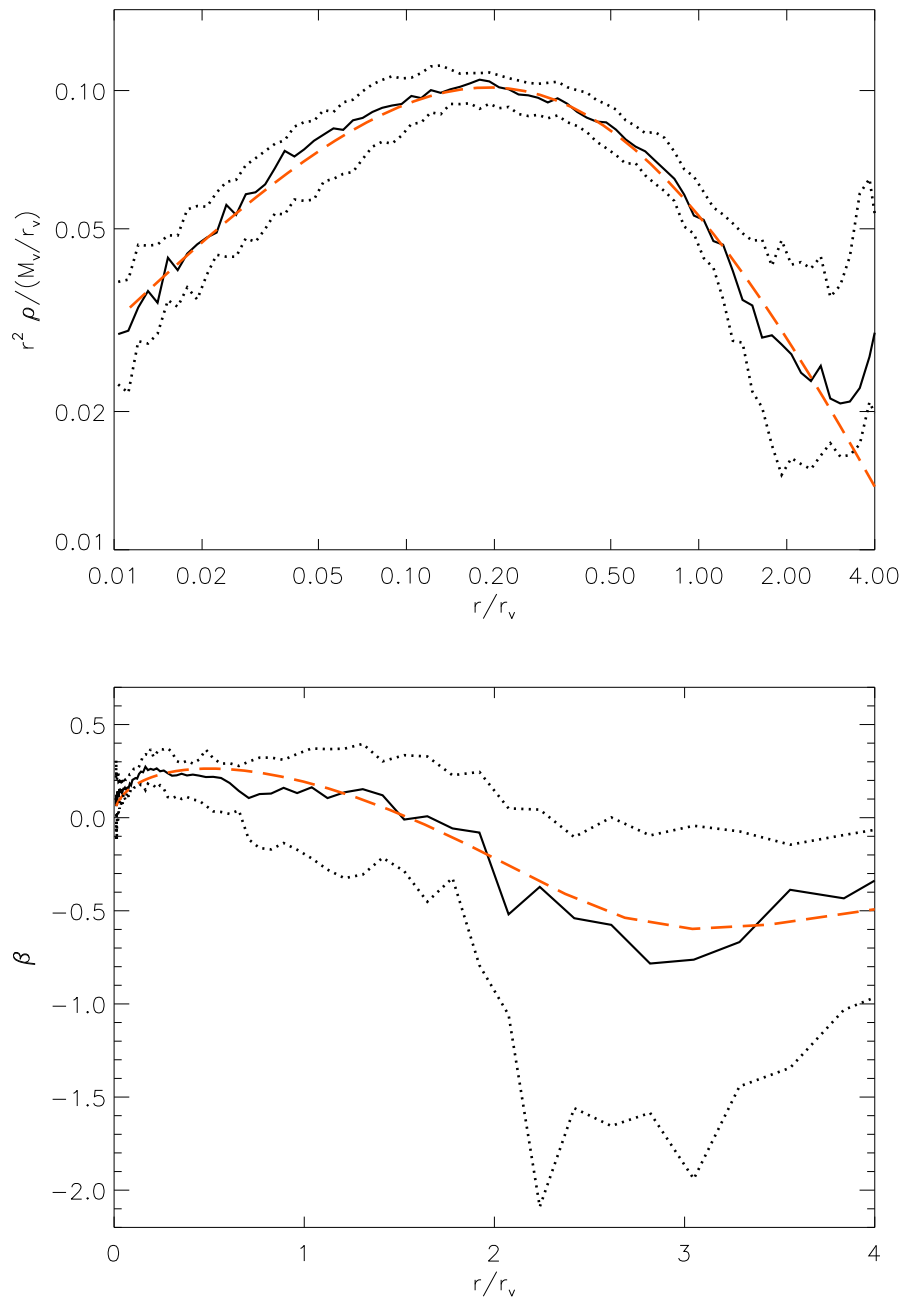


Figure 4.7 Density and anisotropy profiles of the stacked halo. *Top panel:* comparison between the quantity $r^2\rho(r)$, where $\rho(r)$ is the median density profile, from the simulation (black solid line), and from the parametric fit, with $\rho(r)$ given by equation (4.18) and best parameters listed in Table 4.2 (red dashed line). The black dotted lines are the quartiles. *Bottom panel:* Median (black solid) and quartiles (black dotted) velocity anisotropy profile. The red dashed line is the fitting function (4.19) with parameters quoted in Table 4.2.

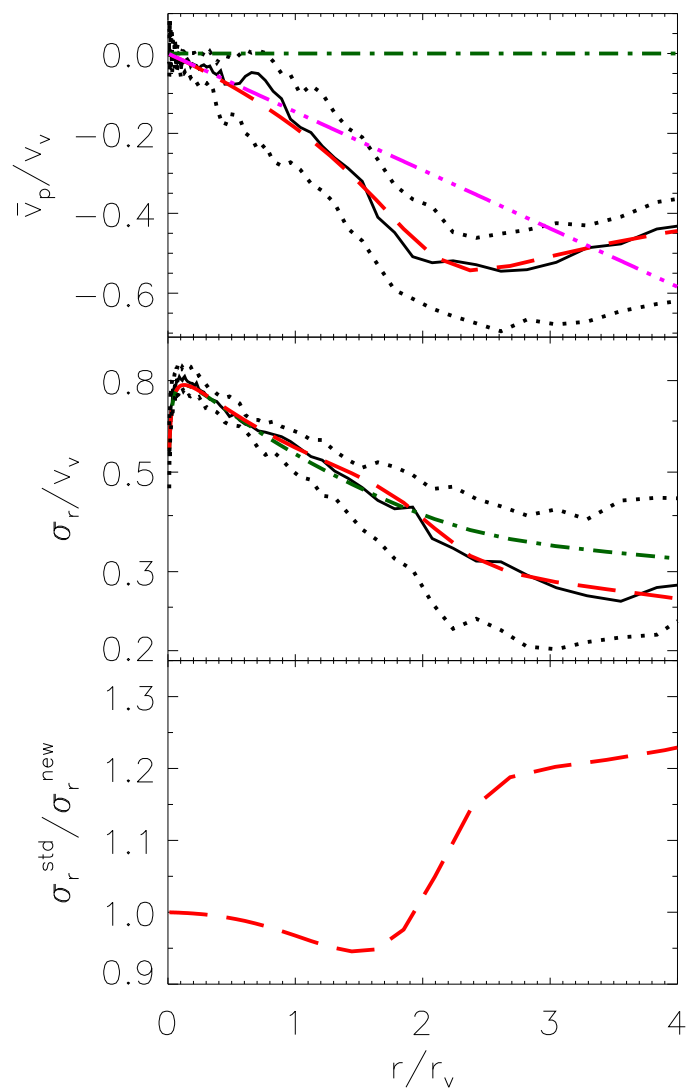


Figure 4.8 Mean peculiar radial velocity and radial velocity dispersion of the stacked halo. *Top panel:* Median (solid black) and quartiles (dotted black) of the mean peculiar radial velocity profile measured in the simulation, and a fit to the form in equation (4.21) with parameters quoted in Table 4.2 (red dashed line). The green dashed-dotted line represents the case of zero peculiar velocity. The magenta dashed-triple-dotted line corresponds to the inner limit $\bar{v}_p \approx -Hr$ for $r \ll r_v$. *Middle panel:* comparison between the radial velocity dispersion profile of the stacked halo, measured in spherical shells (black solid line) and the one computed by equation (5.7), where $\rho(r)$, $\beta(r)$ and $\bar{v}_p(r)$ are approximated with equations (4.18), (4.19) and (4.21), with the parameters of Table 4.2 (red dashed line). We set $\alpha = -1.0$ in eq. (4.24). The green dashed-dotted line is the velocity dispersion profile from the standard Jeans equation (5.5), i.e. for zero mean peculiar velocity. The black dotted lines are the quartiles. *Bottom panel:* Ratio between the dispersion calculated with the standard Jeans equation (the green dashed-dotted line in the middle panel) and with our new generalized equation (the red dashed line in the middle panel).

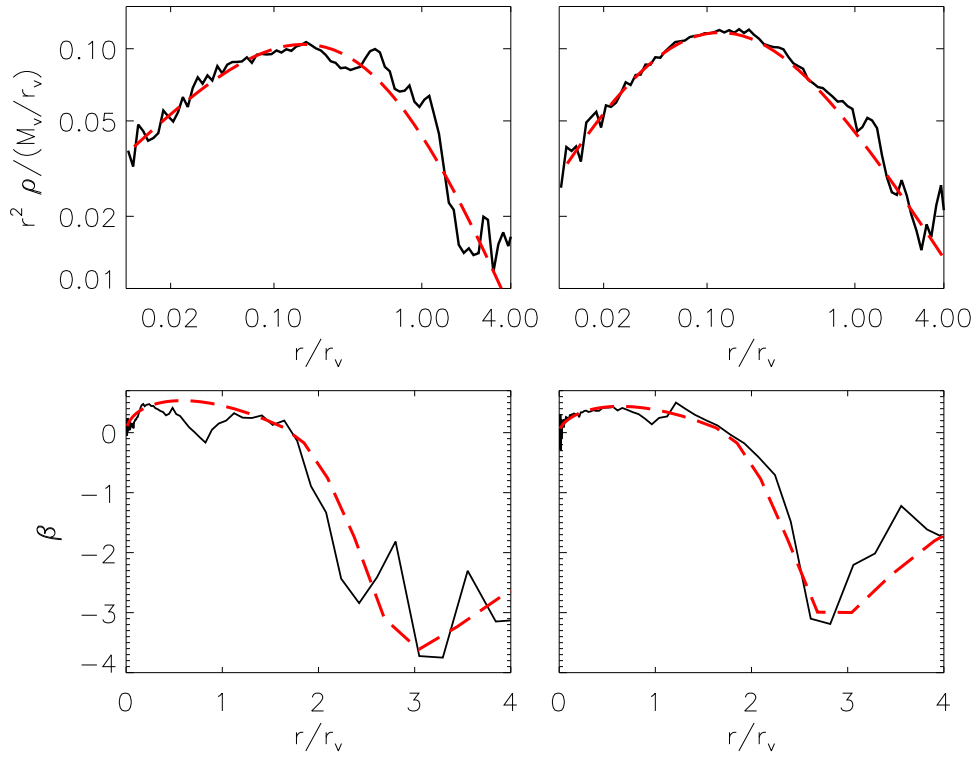


Figure 4.9 Density and anisotropy profiles of the isolated halos. The left panels correspond to *halo 1* and the right panels correspond to *halo 2*. *Top panels*: comparison between the quantity $r^2 \rho(r)$, where $\rho(r)$ is the radial density profile, from the simulation (black solid line), and from the parametric fit, with $\rho(r)$ given by equation (4.18) and best parameters listed in Table 4.3 (red dashed line). *Bottom panels*: radial velocity anisotropy profile (black solid line). The red dashed line is the fitting function (4.19) with parameters quoted in Table 4.3.

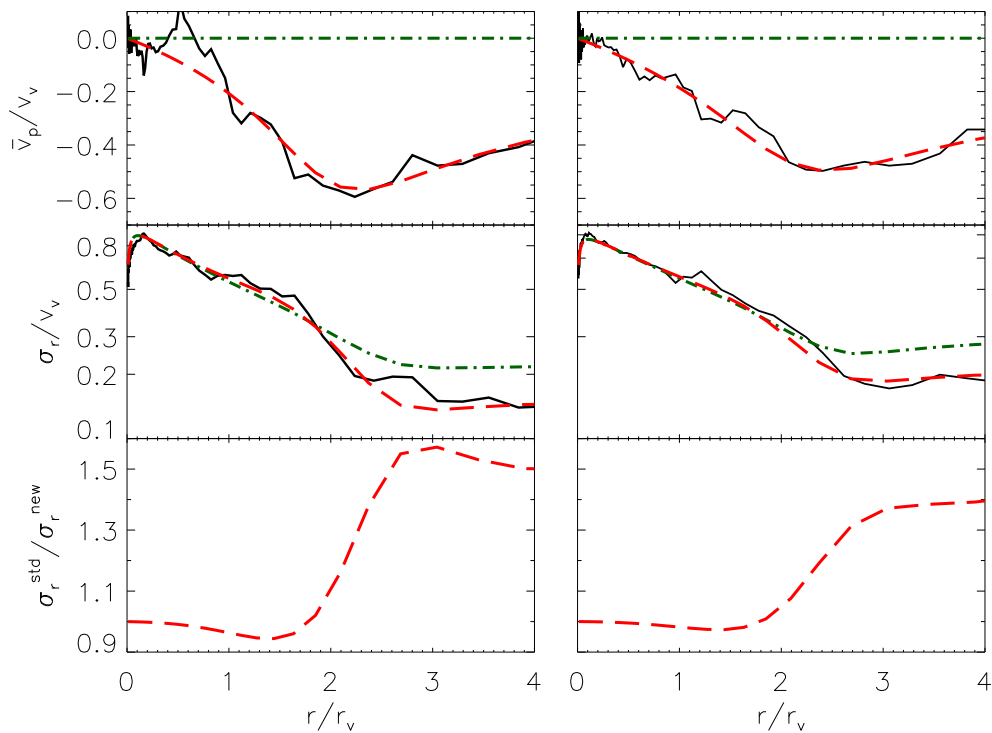


Figure 4.10 Mean peculiar radial velocity and radial velocity dispersion of the isolated halos. The left panels correspond to *halo 1* and the right panels correspond to *halo 2*. *Top panels*: Mean peculiar radial velocity profile measured in the simulation (black solid line), and a fit to the form in equation (4.21) with parameters quoted in Table 4.3 (red dashed line). The green dashed-dotted line represents the case of zero peculiar velocity. *Middle panels*: comparison between the radial velocity dispersion profile, measured in spherical shells (black solid line) and the ones computed by equation (5.7), where $\rho(r)$, $\beta(r)$ and $\bar{v}_p(r)$ are approximated with equations (4.18), (4.19) and (4.21), with the parameters of Table 4.3 (red dashed line). For both halos, we set $\alpha = -0.65$ in eq. (4.24). The green dashed-dotted line corresponds to the velocity dispersion profile from the standard Jeans equation (5.5), i.e. for zero mean peculiar velocity. *Bottom panels*: Ratio between the dispersion calculated with the standard Jeans equation (the green dashed-dotted line in the middle panel) and with our new generalized equation (the red dashed line in the middle panel).

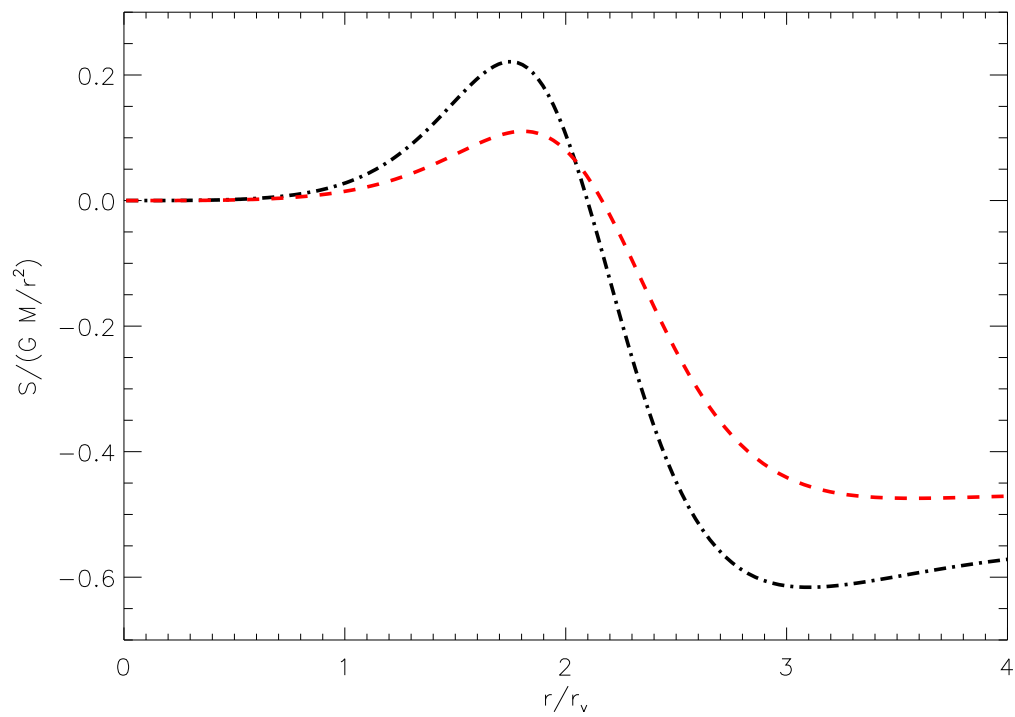


Figure 4.11 Relative mass excess deduced from the standard Jeans equation (5.5), relative to that from the generalized Jeans equation (4.14). The curves show the predictions using the parameters that we fit for the *halo 1* (black dot-dashed) and the *halo 2* (red long dashed).

5

THE JEANS SWINDLE

Why does the Jeans Swindle work?

Martina Falco¹, Steen H. Hansen¹, Radoslaw Wojtak¹, Gary Mamon²

¹ Dark Cosmology Centre, Niels Bohr Institute, University of Copenhagen, Juliane Maries Vej 30, 2100 Copenhagen, Denmark

² Institut d'Astrophysique de Paris (UMR 7095: CNRS & UPMC), 98 bis Bd Arago, 75014 Paris, France

Published in MNRAS-L, Volume 431, Issue 1, p.L6-L9.

Abstract

When measuring the mass profile of any given cosmological structure through internal kinematics, the distant background density is always ignored. This trick is often referred to as the “Jeans Swindle”. Without this trick a divergent term from the background density renders the mass profile undefined, however, this trick has no formal justification. We show that when one includes the expansion of the Universe in the Jeans equation, a term appears which exactly cancels the divergent term from the background. We thereby establish a formal justification for using the Jeans Swindle.



Figure 5.1 This figure shows Andromeda IX, the least luminous galaxy yet discovered. Most of the stars in this image are foreground stars from the Milky Way. CREDIT: Daniel Zucker; The Sloan Digital Sky Survey.

5.1 SUMMARY

When measuring the total mass of a system, such as a galaxy or a galaxy cluster, observers usually analyze the given structure by considering it as an isolated system. Instead, any cosmological object is surrounded by other structures, that can be seen as constant density background, while the object corresponds to an overdensity. When computing the gravitational potential of an overdensity in a homogeneous system, the cosmological background density is discarded. This has been considered a trick since 1902, and it is referred to as *Jeans Swindle*. This problem is related to a basic inconsistency of the Euler and the Poisson equations, relating the density ρ , pressure P , and velocity field \mathbf{v} of a gravitating system :

- Euler equation :

$$\frac{\partial \mathbf{v}}{\partial t} + (\mathbf{v} \cdot \nabla) \mathbf{v} = -\frac{1}{\rho} \nabla P - \nabla \Phi \quad (5.1)$$

- Poisson equation :

$$\nabla^2 \Phi = 4\pi G \rho \quad (5.2)$$

In the case of unperturbed system in equilibrium, the mean velocity \mathbf{v}_0 is zero, while the density ρ_0 and the pressure P_0 are constant. A system in such condition is affected by a fundamental contradiction in the formalism: the two equations above cannot be satisfied simultaneously. Substituting the static unperturbed quantities in the Euler equation implies :

$$\nabla \Phi_0 = 0 \implies \Phi_0 = \text{constant} . \quad (5.3)$$

This is inconsistent with the Poisson equation, which requires that $\nabla^2 \Phi > 0$. The Poisson equation can be satisfied only if $\rho_0 = 0$, which means requiring that the Universe is empty, or that the unperturbed potential is zero. The problem is well explained in the following quotation from (Binney & Tremaine, 2008) :

We remove the inconsistency by the by the ad hoc assumption that Poisson equation describes only the relation between the perturbed density and the perturbed potential, while the

unperturbed potential is zero. This assumption constitutes the Jeans swindle; it is a swindle, of course, because in general there is no formal justification for discarding the unperturbed gravitational field.

In the Jeans equation, which involves the gravitational potential of the system and its dynamical properties, the inclusion of the mean matter density, in the total potential of the system, leads to a divergence, and therefore the Jeans swindle needs to be applied. I have rederived the spherical Jeans equation by adding the background density contribution to the potential, as well as the effect of the Hubble velocity in the dynamical part of the equation:

$$\text{Gravity: } -\rho \frac{GM}{r^2} + \text{BG density potential} = \text{Dynamics: } \frac{d(\rho\sigma^2)}{dr} + \text{Expans. of the Universe,} \quad (5.4)$$

where M is the total mass of the system, σ the velocity dispersion of tracers and ρ the density of tracers.

I find that the divergent term from the background density is exactly cancelled by the term from the expanding universe. This means that the Jeans swindle is not an ad hoc trick, but it is the result of correctly including all the effects due to the cosmology, namely combining the mean matter density and the expansion of the Universe. The details of this work can be found in this chapter.

5.2 INTRODUCTION

A small overdensity in an otherwise infinite homogeneous gravitating system (like any cosmological structure in the Universe) is affected by a basic inconsistency, namely that such a system cannot be in equilibrium, and at the same time obey the Poisson's equation which relates the gravitational potential to the density distribution. A constant gravitational potential leads, via Poisson's equation, to a zero density (Jeans, 1929; Zeldovich & Novikov, 1971). The usual way to overcome this inconsistency is to assume that the infinite homogeneous system does not contribute to the gravitational potential, meaning that the gravitational potential is sourced only by fluctuations to this uniform background density. This assumption is called *Jeans Swindle* (Binney & Tremaine, 1987, 2008; Kiessling, 2003; Joyce, 2008; Ershkovich, 2011). Following Binney & Tremaine (1987) "*it is a swindle because in general there is no formal justification for discarding the unperturbed gravitational field*". It is vindicated by the right results it provides, but it is generally considered a limitation to the formalism.

The Jeans Swindle has several applications. Here we focus on the Jeans Swindle in the context of the Jeans analysis of internal kinematics, which for instance is relevant for stellar motions in dwarf galaxies and galaxy motions in galaxy clusters. The aim of this work is to explain the "swindle" through a clean derivation of the Jeans equation, including the crucial expansion of the Universe.

The Jeans equation describes systems in equilibrium, and it is therefore used to model for example dark matter halos inside the virial region, where they can be treated as equilibrated systems. Dark matter (DM) halos can be seen as a matter excesses over the mean matter density of the Universe. This constant background density is the main contribution to the density distribution at large distances from the halo center (Tavio et al., 2008). We show that the contributions from the background density, the cosmological constant and the Hubble expansion, cancel each other. When omitting the constant background density (the normal "swindle") one is actually excluding it together with the contribution from the expansion of the Universe. Thus, once we take into account the expansion of the Universe and the presence of the cosmological constant, we no longer need to invoke the Jeans Swindle.

5.3 JEANS SWINDLE IN THE JEANS EQUATION

The dynamics of DM halos, modelled as spherical and stationary systems of collisionless particles in equilibrium, is controlled by the spherical non-streaming Jeans equation (Binney, 1980)

$$-\rho(r) \frac{d\Phi}{dr} = \frac{d(\rho\sigma_r^2)}{dr} + 2 \frac{\beta}{r} \rho\sigma_r^2, \quad (5.5)$$

where σ_r is the radial velocity dispersion, $\beta = 1 - \sigma_\theta^2/\sigma_r^2$ the velocity anisotropy, ρ the density distribution of particles and Φ the total gravitational potential.

The potential gradient is given by Poisson's equation

$$\frac{d\Phi}{dr} = \frac{GM(r)}{r^2}. \quad (5.6)$$

In the simple case of an isotropic velocity distribution ($\beta = 0$), the solution to the standard Jeans equation (5.5) for the radial velocity dispersion is (from Binney, 1980)

$$\sigma_r^2(r) = \frac{1}{\rho(r)} \int_r^\infty \rho(s) \left[\frac{GM(s)}{s^2} \right] s. \quad (5.7)$$

Thus, the only quantity required for the calculation of the radial dispersion is the density distribution of the halo. DM-only cosmological N-body simulations indicate that a double slope profile provides a reasonable fit to the density profiles of halos within the virial radius (Navarro et al., 1996; Kravtsov et al., 1998). Since the integration in equation (5.7) extends all the way to infinity, we need a correct description of the DM distribution beyond the virial radius. The correct asymptotic value should be the mean matter density of the Universe ρ_{bg} , given by

$$\rho_{\text{bg}} = \Omega_M \rho_c = \frac{3 \Omega_M H^2}{8\pi G}, \quad (5.8)$$

where Ω_M the matter density parameter, ρ_c is the critical density of the Universe and $H = \dot{a}/a$ is the Hubble constant (a being the scale factor of the Universe).

Therefore, the double slope profile, reaching zero density at large distances from the cluster center, does not reproduce the right density profile in the external region (Tavio et al., 2008). As a first approximation, we can write the density as given by the sum of a term ρ_h that reproduces the inner part of the halo distribution and the constant background density that affects the profile only at large radii

$$\rho(r) = \rho_h(r) + \rho_{\text{bg}}. \quad (5.9)$$

As an example, we consider a finite mass density profile for a cluster-size halo, the Hernquist (1990) profile¹

$$\rho_h(r) = \frac{\rho_0}{r/r_v (1 + r/r_v)^3}, \quad (5.10)$$

where r_v is the virial radius and ρ_0 is the characteristic density, that can be written in terms of the virial overdensity Δ as

$$\rho_0 = \alpha \Delta \rho_c. \quad (5.11)$$

In Figure 5.2, we show the profile given by eq. (5.10) (black solid line) and the sum $\rho_h(r) + \rho_{\text{bg}}$ (green dash-dot line), where the asymptotic value is ρ_{bg} (red dashed line). In the calculation, we set $\Omega_M = 0.24$, $\Delta = 100$, $H = 73 \text{ km s}^{-1} \text{ Mpc}^{-1}$ and we fix α by imposing that the mass given by the density in eq. (5.10) within the sphere of radius r_v corresponds to the virial mass

$$M_v = \frac{4\pi}{3} r_v^3 \Delta \rho_c. \quad (5.12)$$

In Figure 5.2, the density is in units of $\Delta \rho_c$ and the radius is in units of the virial radius.

Once we insert the expression (5.9) in the integral (5.7) we get

$$\begin{aligned} \sigma_r^2(r) &= \frac{1}{\rho_h(r) + \rho_{\text{bg}}} \\ &\times \int_r^\infty G [\rho_h(s) + \rho_{\text{bg}}] [M_h(s) + M_{\text{bg}}(s)] \frac{s}{s^2}, \end{aligned} \quad (5.13)$$

which diverges, since the background mass diverges at large radii. In Fig. 5.3 we plot the solution (5.13) for different upper limits r_{max} in the integral: $r_{\text{max}} = 200 r_v$ (blue short-dashed line), $r_{\text{max}} = 500 r_v$ (green dash-dot line), $r_{\text{max}} = 1000 r_v$ (magenta dash-dot-dot line).

This clearly indicates that when integrating to infinity, the integral will diverge.

¹Here we discuss the simple Hernquist profile for academic reasons. Using any other finite mass structure would lead to the same conclusions.

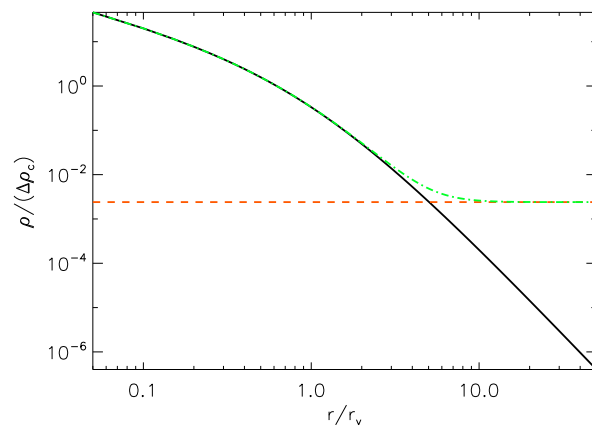


Figure 5.2 *Black solid line*: Hernquist profile given by equation (5.10). *Red dashed line*: background density given by equation (5.8). *Green dash-dot line*: the sum of the Hernquist profile and the constant background density.

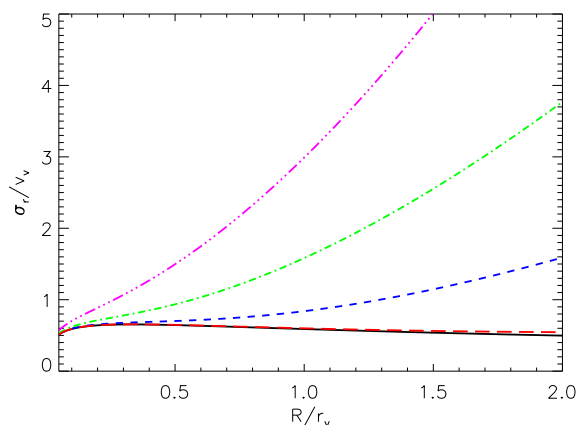


Figure 5.3 Radial velocity dispersion profiles. The black solid line corresponds to the standard Jeans solution (5.14). Solutions of equation (5.13) corresponding to different upper limits r_{\max} in the integral are shown: $r_{\max} = 200 r_v$ (blue short-dashed line), $r_{\max} = 500 r_v$ (green dash-dot line), $r_{\max} = 1000 r_v$ (magenta dash-dot-dot line). The red long-dashed line is the solution when including cosmological expansion and background density (eq. [5.24]). The radial velocity dispersion is in units of the virial velocity and the radius is in units of the virial radius.

The usual trick to avoid the divergence is to omit the contribution of the background density to the potential gradient (5.6), i.e. to set $\nabla\Phi_{\text{bg}} = 0$ (Binney & Tremaine, 1987, 2008; Ershkovich, 2011). Physically, this amounts to assume that the gravitational potential is sourced only by fluctuations to the uniform background density. For this requirement to be consistent with the Poisson's equation (5.6), the constant ρ_{bg} in equation (5.9) has to vanish. This assumption is called the *Jeans Swindle*. It has no justification other than to overcome a mathematical difficulty.

The Jeans analysis has always been performed by discarding the *unperturbed* density, so that

equation (5.7) is just

$$\sigma_r^2(r) = \frac{1}{\rho_h(r)} \int_r^\infty \rho_h(s) \left[\frac{G M_h(s)}{s^2} \right] s. \quad (5.14)$$

The black solid line in fig. 5.3 corresponds to the computation of equation (5.14), which is not divergent.

With this approach, the Jeans equation reproduces the radial dispersion of DM halos from cosmological simulations in the region of equilibrium (Sanchis et al., 2004; Wojtak et al., 2005; Cuesta et al., 2008), and gives finite masses for dwarf galaxies (Strigari et al., 2010; Salucci et al., 2012).

5.4 WHY THE JEANS SWINDLE WORKS

We wish to replace the Jeans Swindle by a formally correct analysis. Thus, we keep the background density ρ_{bg} and its contribution in the gravitational potential. The gradient of the potential due to ρ_{bg} can be put in the following form:

$$\frac{d\Phi_{\text{bg}}}{dr} = \frac{4}{3}\pi G\rho_{\text{bg}} r = \frac{\Omega_m}{2} H^2 r, \quad (5.15)$$

where we have used equation (5.8). However, in order to be consistent, we need to take into account all effects due to the underlying cosmology. For the case of a single halo embedded in a homogeneous Universe with a non-zero cosmological constant Λ , particles also feel a repulsive potential of the form (e.g. Peirani & de Freitas Pacheco, 2006; Nandra et al., 2012)

$$\frac{d\Phi_\Lambda}{dr} = -\frac{1}{3}\Lambda r = -\Omega_\Lambda H^2 r, \quad (5.16)$$

where we have used the relation

$$\Omega_\Lambda = \frac{\Lambda}{3H^2}. \quad (5.17)$$

Introducing the deceleration parameter

$$q = -\frac{\ddot{a}a}{\dot{a}^2} = \frac{\Omega_m}{2} - \Omega_\Lambda, \quad (5.18)$$

we can rewrite the total contribution of the cosmology to the gravitational potential gradient as

$$\frac{d\Phi_{\text{bg}}}{dr} + \frac{d\Phi_\Lambda}{dr} = q H^2 r. \quad (5.19)$$

Moreover, the Universe is not static, but it is subject to the Hubble expansion. Equation (5.5) holds for structures that have achieved dynamical equilibrium. This means that the radial, longitudinal and azimuthal bulk motions are not taken into account in its derivation. When excluding all these bulk velocity terms, the Hubble flow, which DM particles are subject to, is also discarded. The Hubble velocity, $v_H = H r$, might be neglected in the very inner region, but for large radii, it becomes important. Since the integration in equation (5.7) extends to infinity, the inclusion of v_H will affect the result.

When we include the terms involving the mean radial velocity, the Jeans equation becomes the more general formula (Falco et al., 2013b)

$$-\rho \frac{d\Phi}{dr} = \frac{d(\rho\sigma_r^2)}{dr} + 2\frac{\beta}{r}\rho\sigma_r^2 + \rho \left[\bar{v}_r \frac{\partial \bar{v}_r}{\partial r} + \frac{\partial \bar{v}_r}{\partial t} \right]. \quad (5.20)$$

In the most general case, v_r is the sum of the Hubble velocity and a peculiar infall velocity. The infall velocity occurs around cluster-sized haloes ($M_{\text{vir}} \approx 10^{13-14} M_{\odot}$), and is totally negligible around galactic haloes ($M_{\text{vir}} \approx 10^{12} M_{\odot}$) (Prada et al., 2006; Cuesta et al., 2008). Streaming motions around clusters are dominated by the infall velocity at radii between the virial radius and the turn-around radius, which is approximately equal to 3.6 virial radii (Cupani et al., 2008). At larger distances, it approaches the Hubble flow. Therefore, far outside the equilibrated cluster, we can neglect the mean radial peculiar motion of particles, so that the radial velocity corresponds to v_H only

$$\bar{v}_r(r, t) = H(t) r. \quad (5.21)$$

It is straightforward to calculate the additional term in square brackets in eq. (5.20)

$$\bar{v}_r \frac{\partial \bar{v}_r}{\partial r} + \frac{\partial \bar{v}_r}{\partial t} = H^2 r + \dot{H} r = -q H^2 r, \quad (5.22)$$

where we used

$$\dot{H} = -(q+1) H^2. \quad (5.23)$$

We can now write equation (5.7) for large radii, including all these cosmological terms

$$\begin{aligned} \sigma_r^2(r) &= \frac{1}{\rho_h(r) + \rho_{\text{bg}}} \int_r^\infty [\rho_h(s) + \rho_{\text{bg}}] \\ &\quad \times \left[\frac{d\Phi_h}{ds} + \frac{d\Phi_{\text{bg}}}{ds} + \frac{d\Phi_\Lambda}{ds} + \bar{v}_r \frac{\partial \bar{v}_r}{\partial s} + \frac{\partial \bar{v}_r}{\partial t} \right] \S \\ &= \frac{1}{\rho_h(r) + \rho_{\text{bg}}} \int_r^\infty [\rho_h(s) + \rho_{\text{bg}}] \\ &\quad \times \left[\frac{GM_h(s)}{s^2} + q H^2 s|_{\text{bg}, \Lambda} - q H^2 s|_H \right] \S \\ &= \frac{1}{\rho_h(r) + \rho_{\text{bg}}} \int_r^\infty (\rho_h(s) + \rho_{\text{bg}}) \left[\frac{GM_h(s)}{s^2} \right] \S. \end{aligned} \quad (5.24)$$

We thus see that the term $-q H^2 s|_H$ given by the Hubble velocity (5.22) cancels exactly the term $q H^2 s|_{\text{bg}, \Lambda}$ given by the potentials of the background density and the cosmological constant. In this way, we recover the same result as applying the Jeans Swindle, and in the Jeans solution the total mass is again $M(s) = M_h(s)$.

Formally, there is still a minor difference between the two approaches: the density involved in eq. (5.24) is still given by $\rho_h(s) + \rho_{\text{bg}}$, where ρ_{bg} is not zero but instead given by eq. (5.8). However, this time it does not lead to any divergence, because $M_h(s)/s^2$ falls rapidly to zero at large distances. This can be seen in Figure 5.3, where the solution of eq. (5.24) is the red long-dashed line and it matches the result we obtain from equation (5.14) (black solid line). For larger radii, the addition of the background density in the density profile can affect the result slightly. However, in the outer regions, where the halos are no longer equilibrated, the standard Jeans equation is anyway not used to reproduce the radial velocity dispersion. Instead, the generalized Jeans equation in eq. (5.20) must be used, including the infall motion of galaxies. The addition of the peculiar velocity changes the shape of the velocity dispersion in the infall region (Falco et al., 2013b), but it does not affect the conclusion of this work. One could also improve on this minor difference, by not including ρ_{bg} at all radii, but instead a different form which takes into account that the immediate environment of haloes may not be the cosmological value yet. A more accurate density profile would include a term to describe the local region around clusters, before the cosmological background is reached. For example, Cooray & Sheth

(2002) give a detailed description of the halo model, where the background contribution to the total density is given by a more complicated function than the constant value ρ_{bg} only. This is equivalent to define ρ_{h} as

$$\rho_{\text{h}} = \rho_{\text{tot}} - \rho_{\text{bg}}, \quad (5.25)$$

i.e. including in ρ_{h} the details of the background density being different from ρ_{bg} . The equation (5.24) is formally not affected by this modification.

5.5 COMOVING COORDINATES

The equations describing the particle distribution and motion can be written in comoving coordinates (Peebles, 1980). The physical coordinates r and comoving coordinates x are related by the universal time-dependent expansion parameter $a(t)$

$$r = a(t) x. \quad (5.26)$$

When changing variables from the physical space to the comoving one, the Poisson's equation becomes (Peebles, 1980)

$$\nabla^2 \phi = 4\pi G a^2 [\rho(x) - \rho_{\text{bg}}], \quad (5.27)$$

where the gradient is with respect to x , and ρ_{bg} is the mean mass density and $\phi(x)$ is the potential contributed by the overdensity $\rho - \rho_{\text{bg}}$. Therefore, in this coordinate system, the particle motion is already described in terms of the departure from the constant background, and the swindle is not required. As we expect, taking into account the cosmological expansion in the physical space leads to the same result as moving to the expanding space. Equation (5.5) would be correct if we replaced r with x and Φ with ϕ , and using ρ given by (5.9), namely it is the correct Jeans equation in comoving coordinates.

Joyce & Sylos Labini (2012) have also shown that a cosmological N-body simulation of an isolated overdensity should reproduce, in physical coordinates, the same result as a simulation obtained for the structure in open boundary condition without expansion.

We conclude that our work is consistent with the comoving frame analysis by Peebles (1980) and with the conclusions of Joyce & Sylos Labini (2012). This confirms that the Jeans Swindle corresponds to accounting for the expansion of the Universe.

5.6 CONCLUSIONS

We have demonstrated that the Jeans Swindle is not an *ad hoc* trick, but it is the result of correctly combining the mean matter density and the expansion of the Universe. The divergent term from the background density, which in a static universe would lead to a divergent dispersion profile, is exactly cancelled by a term from the expanding universe. We have shown that the dispersion profile measured when assuming no background and a static universe, is the same as the dispersion profile when including both the background density and the expansion. This means that we have established a formal justification for using the Jeans Swindle. This result holds for radii smaller than roughly the virial radius. For larger radii one has to include the effect of infalling matter, which is done through a generalized Jeans equation, as will be presented in a forthcoming article (Falco et al., 2013b).

We thank Wyn Evans for comments, Michael Joyce for useful discussions, and the referee Mark Wilkinson for comments which improved the letter. The Dark Cosmology Centre is funded by the Danish National Research Foundation.

6

CONCLUSION

6.1 SUMMARY

In this thesis, I have explored the properties of clusters of galaxies, dark matter halos and large scale structure. In particular, I have extensively investigated the dynamics of galaxies in the outskirts of clusters, using both a theoretical and observational approach. I have proposed two new methods for measuring the total mass of galaxy clusters, as well as an explanation to the so called *Jeans swindle*, which is invoked in the equations regulating the dynamics of cosmological objects, and is necessary when determining their mass. I will summarize here the main results of this work.

- **Mass estimation in the outer region of galaxy clusters.** We have obtained a generalized Jeans equation that can be used to measure the mass distribution of clusters also in the outer regions, since it takes into account the infall motion of galaxies. The tests performed on cosmological simulations show that the new equation reproduces accurately the radial velocity dispersion profiles of cluster-size halos up to at least four times the virial radius, while the standard Jeans equation overestimates it. In particular, in the region where the extra contributions are significant ($2 - 4 r_v$), the radial velocity dispersion inferred by the standard Jeans equation is overestimated by $\approx 40\%$. This departure is not negligible when measuring the cluster mass through the velocity dispersion modeling. In fact, I find that the systematic error in the mass profile derived from the standard Jeans equation is $\approx 20 - 60\%$ in the range $2 - 4$ virial radii.
- **Mass estimation in the inner region of galaxy clusters from the outskirts.** We have developed a new method for the mass estimation of galaxy clusters. I have tested it on cosmological simulations and applied it to the Coma cluster data. The method involves the detection of extended filaments and sheets, which typically are sitting 5-15 Mpc from the virialized cluster. We identify two sheets in the environment of the Coma cluster. One contains 51 galaxies and extends from ≈ 7 to ≈ 14 Mpc in the phase-space. The second contains 228 galaxies and it extends from ≈ 11 to ≈ 22 Mpc in the phase-space. In the proposed method, the detected structures are used for inferring the virial mass of the neighbor cluster. The estimation of the Coma cluster mass through the analysis of the two sheets, gives $M_{\text{vir}} = (9.2 \pm 2.4) \times 10^{14} M_{\odot}$, in good agreement with previous results from the standard methods.
- **The Jeans swindle.** We provide a formal justification for the commonly used *Jeans swindle*. In fact, I have demonstrated that the Jeans Swindle is not an ad hoc trick, but it is the

result of correctly including all the effects due to the cosmology, namely combining the mean matter density and the expansion of the Universe. I have shown that the dispersion profile measured when assuming no background and a static universe, is the same as the dispersion profile when including both the background density and the expansion.

6.2 FUTURE WORK

I discuss here the future applications of the two mass determination methods developed in this thesis.

- **Mass estimation in the outer region of galaxy clusters.** The proposed method can now be applied to observations. Practically, this technique requires to gather galaxy data in the outer regions of galaxy clusters, and fit their line of sight velocity dispersions using the solution of our generalized Jeans equation. This needs dense redshift surveys that include data up to very large distances from the clusters center. This analysis would be very useful because it can significantly contribute to determine the mass distribution far from the center of the cluster. The new extended Jeans analysis would involve the same steps as the standard one. One of the complications is the interloper removal: outside the virialized region, the process of separating the background galaxies from the cluster members is in fact not trivial. The model also involves the radial velocity anisotropy of galaxies. Just as several approaches have been proposed to break the mass-velocity anisotropy degeneracy in the standard Jeans equations, the same should be done when applying the generalized Jeans equation. Moreover, in the generalized case, we also need to determine a new quantity, i.e. the infall velocity profile.
- **Mass estimation in the inner region of galaxy clusters from the outskirts.** The next step of the work is to apply the method to a sample of clusters of galaxies, in order to make a statistical test on its efficiency. Moreover, this technique shows to have promising possible developments. For example, one could look at large distances from the cluster along the line of sight, instead of along the projected radius on the sky. This would mean to analyze galaxies at redshifts within a large range around the cluster redshift.

Within this work, we also constrain the spatial orientation of the detected structures. Therefore, another future prospective is to test whether our method can actually be used as a tool to extract information about the three-dimensional galaxy distribution outside galaxy clusters.

BIBLIOGRAPHY

- Abazajian, K. N., et al. 2009, *ApJs*, 182, 543
- Abell, G. O. 1958, *ApJs*, 3
- Allen, S. W., Evrard, A. E., & Mantz, A. B. 2011, *Annual Review of Astronomy and Astrophysics*, 49, 409
- Allen, S. W., Rapetti, D. A., Schmidt, R. W., Ebeling, H., Morris, R. G., & Fabian, A. C. 2008, *MNRAS*, 383, 879
- Aragón-Calvo, M. A., Jones, B. J. T., van de Weygaert, R., & van der Hulst, J. M. 2007, *A&A*, 474, 315
- Aragón-Calvo, M. A., van de Weygaert, R., & Jones, B. J. T. 2010, *MNRAS*, 408, 2163
- Ascasibar, Y., & Gottlöber, S. 2008, *MNRAS*, 386, 2022
- Bahcall, N. A. 1997, *Unsolved Problems in Astrophysics*, 61
- Balland, C., & Blanchard, A. 1997, *ApJ*, 487, 33
- Begeman, K. G., Broeils, A. H., & Sanders, R. H. 1991, *MNRAS*, 249, 523
- Bennett, C. L., et al. 1996, *ApJL*, 464, L1
- Bertschinger, E. 1985, *ApJS*, 58, 39
- Binney, J. 1980, *MNRAS*, 190, 873
- Binney, J., & Mamon, G. A. 1982, *MNRAS*, 200, 361
- Binney, J., & Tremaine, S. 1987, *Galactic dynamics* (Princeton University Press), 287–296, 681–686
- . 2008, *Galactic Dynamics: Second Edition* (Princeton University Press)
- Biviano, A. 1998, [arXiv:astro-ph/9711251](https://arxiv.org/abs/astro-ph/9711251)
- Biviano, A., & Girardi, M. 2003, *ApJ*, 585, 205
- Bond, J. R., Kofman, L., & Pogosyan, D. 1996, *Nature*, 380, 603
- Bond, N. A., Strauss, M. A., & Cen, R. 2010, *MNRAS*, 409, 156
- Borgani, S., & Kravtsov, A. 2011, *Advanced Science Letters*, 4, 204
- Borgani, S., et al. 2004, *MNRAS*, 348, 1078

- Boylan-Kolchin, M., Springel, V., White, S. D. M., Jenkins, A., & Lemson, G. 2009, *MNRAS*, 398, 1150
- Brinckmann, T., Lindholmer, M., Falco, M., Hansen, S. H., Wojtak, R., & Sparre, M. 2013, in preparation
- Brown, S., & Rudnick, L. 2011, *MNRAS*, 412, 2
- Bryan, G. L., & Norman, M. L. 1998, *ApJ*, 495, 80
- Burenin, R. A., & Vikhlinin, A. A. 2012, *Astronomy Letters*, 38, 347
- Carlberg, R. G., Yee, H. K. C., Ellingson, E., Abraham, R., Gravel, P., Morris, S., & Pritchet, C. J. 1996, *ApJ*, 462, 32
- Carroll, S. M. 2004, *Spacetime and geometry. An introduction to general relativity* (Addison Wesley)
- Coe, D. 2010, arXiv1005.0411
- Colberg, J. M., Krughoff, K. S., & Connolly, A. J. 2005, *MNRAS*, 359, 272
- Colberg, J. M., White, S. D. M., Jenkins, A., & Pearce, F. R. 1999, *MNRAS*, 308, 593
- Cole, S., & Lacey, C. 1996, *MNRAS*, 281, 716
- Colless, M., et al. 2001, *MNRAS*, 328, 1039
- . 2003, *VizieR Online Data Catalog*, 7226
- Collins, II, G. W. 1978, *The virial theorem in stellar astrophysics* (Tucson, Ariz., Pachart Publishing House (Astronomy and Astrophysics Series. Volume 7))
- Cooray, A., & Sheth, R. 2002, *Physics Reports*, 372, 1
- Cuesta, A. J., Prada, F., Klypin, A., & Moles, M. 2008, *MNRAS*, 389, 385
- Cunha, C., Huterer, D., & Frieman, J. A. 2009, *Phys. Rev. D*, 80, 063532
- Cupani, G., Mezzetti, M., & Mardirossian, F. 2008, *MNRAS*, 390, 645
- Davis, M., Efstathiou, G., Frenk, C. S., & White, S. D. M. 1985, *ApJ*, 292, 371
- de Lapparent, V., Geller, M. J., & Huchra, J. P. 1986, *ApJL*, 302
- Diaferio, A. 1999, *MNRAS*, 309, 610
- Diaferio, A., Geller, M. J., & Rines, K. J. 2005, *ApJL*, 628, L97
- Dietrich, J. P., Werner, N., Clowe, D., Finoguenov, A., Kitching, T., Miller, L., & Simionescu, A. 2012, *Nature*, 487, 202
- Efstathiou, G., Davis, M., White, S. D. M., & Frenk, C. S. 1985, *ApJs*, 57, 241
- Einasto, J., Klypin, A. A., Saar, E., & Shandarin, S. F. 1984, *MNRAS*, 206, 529
- Ershkovich, A. I. 2011, *ArXiv e-prints*, arXiv:astro-ph/1108.5519

- Ettori, S., Fabian, A. C., Allen, S. W., & Johnstone, R. M. 2002a, *MNRAS*, 331, 635
- . 2002b, *MNRAS*, 331, 635
- Ettori, S., & Molendi, S. 2011, *Memorie della Societa Astronomica Italiana Supplementi*, 17, 47
- Fakhouri, O., Ma, C.-P., & Boylan-Kolchin, M. 2010, *MNRAS*, 406, 2267
- Falco, M., Hansen, S., Wojtak, R., & Mamon, G. A. 2013a, *MNRAS*, 431, L6
- Falco, M., Mamon, G. A., Wojtak, R., Hansen, S. H., & Gottlöber, S. 2013b, *arXiv:astro-ph/1306.6637*
- Freedman, W. L., et al. 2001, *ApJ*, 553, 47
- Gavazzi, R., Adami, C., Durret, F., Cuillandre, J.-C., Ilbert, O., Mazure, A., Pelló, R., & Ulmer, M. P. 2009, *Astronomy and Astrophysics*, 498, L33
- Geller, M. J., Diaferio, A., & Kurtz, M. J. 1999, *ApJL*, 517, L23
- Geller, M. J., & Huchra, J. P. 1989, *Science*, 246, 897
- Girardi, M., Giuricin, G., Mardirossian, F., Mezzetti, M., & Boschin, W. 1998, *ApJ*, 505, 74
- Gonzalez, A. H., Zaritsky, D., & Zabludoff, A. I. 2007, *ApJ*, 666, 147
- Gott, III, J. R. 1975, *ApJ*, 201, 296
- Gottloeber, S., & Klypin, A. 2008, *arXiv:0803.4343*
- Gregory, S. A., Thompson, L. A., & Tifft, W. G. 1978, *Bulletin of the American Astronomical Society*, 10, 622
- Gunn, J. E. 1977, *ApJ*, 218, 592
- Gunn, J. E., & Gott, III, J. R. 1972, *ApJ*, 176, 1
- Gursky, H., Kellogg, E., Murray, S., Leong, C., Tananbaum, H., & Giacconi, R. 1971, *ApJ*, 167, L81
- Hahn, O., Porciani, C., Carollo, C. M., & Dekel, A. 2007, *MNRAS*, 375, 489
- Haiman, Z., Mohr, J. J., & Holder, G. P. 2001, *ApJ*, 553, 545
- Hansen, S. H., & Stadel, J. 2003, *ApJ*, 595, L37
- Hernquist, L. 1990, *ApJ*, 356, 359
- Hoekstra, H., Franx, M., Kuijken, K., & Squires, G. 1998, *ApJ*, 504, 636
- Hoffman, Y., Metuki, O., Yepes, G., Gottlöber, S., Forero-Romero, J. E., Libeskind, N. I., & Knebe, A. 2012, *MNRAS*, 425, 2049
- Host, O., & Hansen, S. H. 2011, *ApJ*, 736, 52
- Hubble, E. 1929, *Proceedings of the National Academy of Science*, 15, 168
- Huchra, J., et al. 2005, *Astronomical Society of the Pacific Conference Series*, 329, 135

- Hughes, J. P. 1989, *ApJ*, 337, 21
- Jeans, J. H. 1929, *The Universe Around Us* (Cambridge, University Press)
- Johnston, D. E., et al. 2007, arXiv:0709.1159
- Joyce, M. 2008, *American Institute of Physics Conference Series*, 970, 237
- Joyce, M., & Sylos Labini, F. 2012, *MNRAS* in press, arXiv:1210.1140
- Kaiser, N., Squires, G., & Broadhurst, T. 1995, *ApJ*, 449
- Karachentsev, I. D., & Nasonova, O. G. 2010, *MNRAS*, 405, 1075
- Karachentsev, I. D., & Nasonova (Kashibadze), O. G. 2010, *Astrophysics*, 53, 32
- Katgert, P., Biviano, A., & Mazure, A. 2004, *ApJ*, 600, 657
- Kellogg, E., Gursky, H., Leong, C., Schreier, E., Tananbaum, H., & Giacconi, R. 1971a, *ApJL*, 165, L49
- . 1971b, *ApJL*, 165, L49
- Kent, S. M., & Gunn, J. E. 1982, *AJ*, 87, 945
- Kiessling, M. K.-H. 2003, *Advances in Applied Mathematics*, 31, 138
- Kravtsov, A. V., Klypin, A. A., Bullock, J. S., & Primack, J. R. 1998, *ApJ*, 502, 48
- Kravtsov, A. V., Klypin, A. A., & Khokhlov, A. M. 1997, *ApJs*, 111, 73
- Kubo, J. M., Stebbins, A., Annis, J., Dell'Antonio, I. P., Lin, H., Khiabani, H., & Frieman, J. A. 2007, *ApJ*, 671, 1466
- Łokas, E. L., & Mamon, G. A. 2003, *MNRAS*, 343, 401
- Łokas, E. L., Wojtak, R., Gottlöber, S., Mamon, G. A., & Prada, F. 2006, *MNRAS*, 367, 1463
- Lombardi, M., & Bertin, G. 1999, *A&A*, 348, 38
- Lombriser, L. 2011, *Phys. Rev. D*, 83, 063519
- Ludlow, A. D., Navarro, J. F., White, S. D. M., Boylan-Kolchin, M., Springel, V., Jenkins, A., & Frenk, C. S. 2011, *MNRAS*, 415, 3895
- MacTavish, C. J., et al. 2006, *ApJ*, 647, 799
- Mahajan, S., Mamon, G. A., & Raychaudhury, S. 2011, *MNRAS*, 416, 2882
- Mamon, G. A., & Boué, G. 2010, *MNRAS*, 401, 2433
- Mamon, G. A., & Łokas, E. L. 2005, *MNRAS*, 363, 705
- Mamon, G. A., Sanchis, T., Salvador-Solé, E., & Solanes, J. M. 2004, *A&A*, 414, 445
- Mamon, G. A., Tweed, D., Thuan, T. X., Cattaneo, A., Papaderos, P., Recchi, S., & Hensler, G. 2012, *Predicting the Frequencies of Young and of Tiny Galaxies* (Springer-Verlag, Berlin), 39

- Mandelbaum, R., Seljak, U., Baldauf, T., & Smith, R. E. 2010, *MNRAS*, 405, 2078
- Mei, S., et al. 2007, *ApJ*, 655, 144
- Merritt, D. 1987, *ApJ*, 313, 121
- Mohayaee, R., & Tully, R. B. 2005, *ApJ*, 635, L113
- Moore, B., Quinn, T., Governato, F., Stadel, J., & Lake, G. 1999, *MNRAS*, 310
- More, S., Kravtsov, A. V., Dalal, N., & Gottlöber, S. 2011, *ApJS*, 195, 4
- Motl, P. M., Hallman, E. J., Burns, J. O., & Norman, M. L. 2005, *ApJL*, 623, L63
- Nandra, R., Lasenby, A. N., & Hobson, M. P. 2012, *MNRAS*, 422
- Nasonova, O. G., de Freitas Pacheco, J. A., & Karachentsev, I. D. 2011, *A&A*, 532, A104
- Navarro, J. F., Frenk, C. S., & White, S. D. M. 1996, *ApJ*, 462
- Neistein, E., & Dekel, A. 2008, *MNRAS*, 383, 615
- Novikov, D., Colombi, S., & Doré, O. 2006, *MNRAS*, 366, 1201
- Peebles, P. J. E. 1980, *The large-scale structure of the universe* (Research supported by the National Science Foundation. Princeton, N.J., Princeton University Press, 1980. 435 p.)
- . 1993, *Princeton Series in Physics: Principles of Physical Cosmology* (Princeton, NJ: Princeton Univ. Press)
- Peirani, S., & de Freitas Pacheco, J. A. 2006, *New Astronomy*, 11, 325
- . 2008, *A&A*, 488, 845
- Perlmutter, S., et al. 1999, *ApJ*, 517, 565
- Planck Collaboration et al. 2013, arXiv1303.5076
- Popesso, P., Biviano, A., Böhringer, H., & Romaniello, M. 2007, *A&A*, 464, 451
- Porter, S. C., Raychaudhury, S., Pimblet, K. A., & Drinkwater, M. J. 2008, *MNRAS*, 388, 1152
- Power, C., Knebe, A., & Knollmann, S. R. 2012, *MNRAS*, 419, 1576
- Prada, F., Klypin, A. A., Simonneau, E., Betancort-Rijo, J., Patiri, S., Gottlöber, S., & Sanchez-Conde, M. A. 2006, *ApJ*, 645, 1001
- Reiprich, T. H., Basu, K., Ettori, S., Israel, H., Lovisari, L., Molendi, S., Pointecouteau, E., & Roncarelli, M. 2013, *SSR*, 177, 195
- Reiprich, T. H., Böhringer, H., & Schuecker, P. 2001, *Astronomical Society of the Pacific Conference Series*, 234, 405
- Riess, A. G., et al. 1998, *AJ*, 116, 1009
- Rines, K., & Diaferio, A. 2006, *AJ*, 132, 1275
- Rines, K., Geller, M. J., Kurtz, M. J., & Diaferio, A. 2003, *ApJ*, 126, 2152

- Ryden, B. 2003, *Introduction to cosmology* (San Francisco, CA, USA: Addison Wesley, ISBN 0-8053-8912-1)
- Salucci, P., Wilkinson, M. I., Walker, M. G., Gilmore, G. F., Grebel, E. K., Koch, A., Frigerio Martins, C., & Wyse, R. F. G. 2012, *MNRAS*, 420, 2034
- Sanchis, T., Mamon, G. A., Salvador-Solé, E., & Solanes, J. M. 2004, *A&A*, 418, 393
- Sarazin, C. L. 1988, *Book-Review - X-Ray Emissions from Clusters of Galaxies, Vol. 76 (Sky and Telescope)*
- Schmidt, R. W., & Allen, S. W. 2007, *MNRAS*, 379, 209
- Serpico, P. D., Esposito, S., Iocco, F., Mangano, G., Miele, G., & Pisanti, O. 2004, *JCAP*, 12, 10
- Serra, A. L., Diaferio, A., Murante, G., & Borgani, S. 2011, *MNRAS*, 412, 800
- Shandarin, S. F., & Zeldovich, I. B. 1983, *Comments on Astrophysics*, 10, 33
- Shectman, S. A., Landy, S. D., Oemler, A., Tucker, D. L., Lin, H., Kirshner, R. P., & Schechter, P. L. 1996, *ApJ*, 470, 172
- Sousbie, T., Pichon, C., Colombi, S., Novikov, D., & Pogosyan, D. 2008, *MNRAS*, 383, 1655
- Sparre, M. 2013, submitted to *JCAP*
- Spergel, D. N., et al. 2007, *ApJs*, 170, 377
- Strigari, L. E., Frenk, C. S., & White, S. D. M. 2010, *MNRAS*, 408, 2364
- Sunyaev, R. A., & Zeldovich, I. B. 1980, *ARA&A*, 18, 537
- Tavio, H., Cuesta, A. J., Prada, F., Klypin, A. A., & Sanchez-Conde, M. A. 2008, *ArXiv e-prints*, arXiv:astro-ph/0807.3027
- Taylor, J. E., & Navarro, J. F. 2001, *ApJ*, 563, 483
- Tegmark, M., et al. 2004, *ApJ*, 606, 702
- The, L. S., & White, S. D. M. 1986, *Astronomical Journal*, 92, 1248
- van de Weygaert, R., & Bond, J. R. 2008, *Lecture Notes in Physics*, Berlin Springer Verlag, 740, 409
- van Haarlem, M., & van de Weygaert, R. 1993, *ApJ*, 418, 544
- Voit, G. M. 2005, *Rev. Mod. Phys.*, 77, 207
- Wadekar, D., & Hansen, S. H. 2013, in preparation
- Watt, M. P., Ponman, T. J., Bertram, D., Eyles, C. J., Skinner, G. K., & Willmore, A. P. 1992, *MNRAS*, 258, 738
- Wechsler, R. H., Bullock, J. S., Primack, J. R., Kravtsov, A. V., & Dekel, A. 2002, *ApJ*, 568, 52
- Wen, Z. L., Han, J. L., & Liu, F. S. 2010, *MNRAS*, 407, 533
- White, M., Cohn, J. D., & Smit, R. 2010, *MNRAS*, 408, 1818

- White, S. D. M., & Frenk, C. S. 1991, *ApJ*, 379, 52
- Wojtak, R., & Łokas, E. L. 2010, *MNRAS*, 408, 2442
- Wojtak, R., Łokas, E. L., Gottlöber, S., & Mamon, G. A. 2005, *MNRAS*, 361, L1
- Wojtak, R., Łokas, E. L., Mamon, G. A., & Gottlöber, S. 2009, *MNRAS*, 399, 812
- Wojtak, R., Łokas, E. L., Mamon, G. A., Gottlöber, S., Klypin, A., & Hoffman, Y. 2008, *MNRAS*, 388, 815
- Zappacosta, L., Buote, D. A., Gastaldello, F., Humphrey, P. J., Bullock, J., Brighenti, F., & Mathews, W. 2006, *ApJ*, 650, 777
- Zeldovich, I. B., Einasto, J., & Shandarin, S. F. 1982, *Nature*, 300, 407
- Zeldovich, Y. B., & Novikov, I. D. 1971, *Relativistic astrophysics. Vol.1: Stars and relativity* (Chicago: University of Chicago Press, 1971)
- Zhao, D. H., Mo, H. J., Jing, Y. P., & Börner, G. 2003, *MNRAS*, 339, 12
- Zu, Y., & Weinberg, D. H. 2013, *MNRAS*, 431, 3319
- Zwicky, F. 1933, *Helvetica Physica Acta*, 6, 110
- Zwicky, F., Herzog, E., Wild, P., Karpowicz, M., & Kowal, C. T. 1961, Pasadena: California Institute of Technology (CIT)